Hypersonic phonon propagation in mesoscopic systems by Brillouin spectroscopy

Dissertation
zur Erlangung des Grades
'Doktor der Naturwissenschaften'
(Dr. rer. nat.)
im Promotionsfach Chemie

am Fachbereich Chemie, Pharmazie und Geowissenschaften
der Johannes Gutenberg–Universität Mainz

vorgelegt von

Dipl.-Chem. Dirk Schneider

geboren in Guben

Mainz, 2013

Die vorliegende Arbeit wurde im Zeitraum von Oktober 2010 bis November 2013 am Max-Planck-Institut für Polymerforschung in Mainz unter der Anleitung von Herrn Prof. Dr. [redacted] und Herrn Prof. Dr. [redacted] angefertigt.

Tag der mündlichen Prüfung: 17. 12. 2013
Dekan: Prof. Dr. [redacted]
Erster Berichterstatter: Prof. Dr. [redacted]
Zweiter Berichterstatter: Prof. Dr. [redacted]
Dritter Berichterstatter: Prof. [redacted]

For my beloved wife:
“You’re a friend indeed, when a friend is in need.”

inspired by R. Bergin

Contents

Abstract

Phononic crystals, capable to block or direct the propagation of elastic/acoustic waves, have attracted increasing interdisciplinary interest across condensed matter physics and materials science. As of today, no generalized full description of elastic wave propagation in phononic structures is available, mainly due to the large number of variables determining the band diagram. Therefore, this thesis aims for a deeper understanding of the fundamental concepts governing wave propagation in mesoscopic structures by investigation of appropriate model systems. The phononic dispersion relation at hypersonic frequencies is directly investigated by the non-destructive technique of high-resolution spontaneous Brillouin light scattering (BLS) combined with computational methods.

Due to the vector nature of the elastic wave propagation, we first studied the hypersonic band structure of hybrid superlattices. These 1D phononic crystals composed of alternating layers of hard and soft materials feature large Bragg gaps. BLS spectra are sensitive probes of the moduli, photo-elastic constants and structural parameters of the constituent components. Engineering of the band structure can be realized by introduction of defects. Here, cavity layers are employed to launch additional modes that modify the dispersion of the undisturbed superlattice, with extraordinary implications to the band gap region. Density of states calculations in conjunction with the associated deformation allow for unambiguous identification of surface and cavity modes, as well as their interaction with adjacent defects.

Next, the role of local resonances in phononic systems is explored in 3D structures based on colloidal particles. In turbid media BLS records the particle vibration spectrum comprising resonant modes due to the spatial confinement of elastic energy. Here, the frequency and lineshapes of the particle eigenmodes are discussed as function of increased interaction and departure from spherical symmetry. The latter is realized by uniaxial stretching of polystyrene spheres, that can be aligned in an alternating electric field. The resulting spheroidal crystals clearly exhibit anisotropic phononic properties.

Establishing reliable predictions of acoustic wave propagation, necessary to advance, e.g., optomechanics and phononic devices is the ultimate aim of this thesis.

Zusammenfassung

Phononische Kristalle, welche die Ausbreitung elastischer/akustischer Wellen kontrollieren können, stoßen auf ein immer größeres interdisziplinäres Interesse, sowohl in der Festkörperphysik als auch in den Materialwissenschaften. Eine allumfassende Beschreibung der Wellenausbreitung in phononischen Strukturen ist bis heute nicht vorhanden, vor allem aufgrund der vielen Einflussgrößen des Banddiagramms. Ziel dieser Arbeit ist es daher, durch die Untersuchung geeigneter Modellsysteme, ein tieferes Verständnis der fundamentalen Zusammenhänge zu erhalten. Die Dispersionsrelation im GHz-Band (Hyperschall) kann mittels zerstörungsfreier und hochauflösender Brillouin Lichtstreuung (BLS) direkt bestimmt werden.

Die Vektoreigenschaften elastischer Wellen legen die Untersuchung vereinfachter Bandstrukturen nahe, z.B. die von (hybriden) Übergittern. Diese eindimensionalen phononischen Kristalle bestehen aus wechselnden Lagen eines harten bzw. weichen Materials und zeigen große akustische Bandlücken. BLS-Spektren geben Aufschluss über elastische Moduln, photo-elastische Konstanten und strukturelle Parameter der einzelnen Komponenten. Schichten abweichender Dicke (Kavitäten) können zusätzliche Moden erzeugen, welche die Dispersion des perfekten Übergitters modifizieren, insbesondere im Bereich der Bandlücke. Deformations- und Zustandsdichteberechnungen erlauben die Identifizierung von Oberflächen- und Kavitätenmoden, sowie ihrer Wechselwirkung mit benachbarten Defekten.

Des Weiteren betrachten wir lokale Resonanzen in 3D-phononischen Strukturen, basierend auf kolloidalen Partikeln. In nicht-transparenten Medien misst die BLS das Spektrum resonanter Moden aufgrund der Lokalisierung von elastischer Energie (Partikeleigenschwingungen). Die Form und Lage der Spektrallinien sind untersucht als Funktion zunehmender interpartikulärer Wechselwirkung und abnehmender Symmetrie. Letztere wurde durch Verstreckung von Polystyrolkugeln realisiert, die zudem im elektrischen Wechselfeld ausgerichtet werden können. Die erhaltenen sphäroidalen Kristalle haben eindeutig anisotrope phononische Eigenschaften.

Diese Arbeit ist Teil der Bemühungen die Vorhersagbarkeit der Ausbreitung elastischer Wellen zu verbessern, welche ein integraler Bestandteil für die Weiterentwicklung von z.B. optomechanischen und phononischen Komponenten ist.

Part I.

Introduction

1. Hypersonic Phononics

This Chapter contains an introduction to the field of hypersonic phononics. A short historical outline is sketched to reenact the development until today. Finally, the current challenges are addressed and the motivation is pointed out.

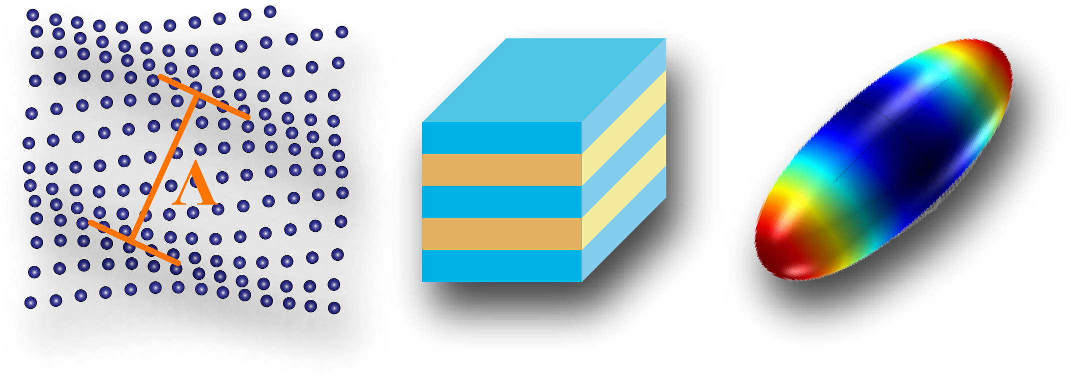

1.1. Historical Sketch

The urge for a deeper understanding of their environment has driven humanity from the dawn of time and culminated in the modern natural sciences. Many phenomena in nature such as the red color of sunsets, lightning or earthquakes have been long unexplained but are well-understood, today. The interaction between energy and matter determines our daily life, to such an extent that no living organism and no machine is conceivable without this fundamental feature.

All of the aforementioned natural events involve energy in form of electromagnetic and elastic waves interacting with small molecules or condensed matter, respectively. Wave phenomena are of striking importance as within a specific wavelength range they can be directly perceived as light and sound. Their interaction with matter (e.g., in a scattering experiment) gives insight to the materials inner structure, hence plays a pivotal role for the measurement of physical quantities.

We should acknowledge that the wave formalism for light and sound is only one way to account for the observations. In the late 17th century, Huygens[1] and Newton laid the foundations for two competing theories for the description of light. While the scientific community was in favor of Newtons corpuscular picture[2] in the 18th century, the close of the 19th century brought the breakthrough of the wave view based on the experiments on interference (Young and Fresnel),[3] polarization (Arago) and Maxwell's[4] and Hertz'[5] works on electromagnetic fields. At the turn of the 20th century, Planck realized that the energy emitted or absorbed by matter is an integer multiple of hf,[6] with h being a constant named after him and f being the frequency of the wave (i.e., the color). In 1905, Einstein postulated that light consists of "light quanta" to explain the photoelectric effect[7] which is considered as one of the foundations of modern quantum physics.

The consequences of the apparent contradiction of the two views have been heavily debated and gave rise to the Copenhagen interpretation of quantum mechanics, that essentially favors a probabilistic description of nature, in the 1920s.[8] In the due course the terms "photon"[9] and "phonon"[10] for quantums of electromagnetic and elastic waves were established. Today, the wave-particle duality is widely accepted and readily applicable to practical cases where particles have low masses or waves have high energies, respectively. In 1924, de Broglie extended the duality to particles and allocated them a wavelength $\lambda = h/p$,[11] with p being the momentum. His postulate has been proven by diffraction experiments ranging from small particles like electrons[12] up to large particles like fullerenes (C_{60}),[13] in 1999. With the development of quantum field theory in the second half of the 20thcentury, the distinction between particles and waves became obsolete as all (quasi-)particles can be described as excited states in an underlying physical field.

The generated knowledge facilitated the analysis of scattering experiments that used small particles and electromagnetic waves. A few examples are the (Rutherford) scattering of α-particles on gold atoms leading to the planetary model for atoms[14] or the electron spin discovered by the deflection of silver atoms under an magnetic field in the Stern-Gerlach experiment.[15,16] X-ray diffraction became important for the analysis of crystal structures[17] and inelastic light scattering (Raman)[18] can be used to probe the vibrational states of small molecules or the high frequency phonons and magnons (spin waves) in condensed matter. Ultrasonic waves are utilized, e.g., for medical imaging and submarine navigation (sonar).

Today, numerous methods are known to investigate the inner structure of materials, their chemical composition, phase transitions etc.. A wide range of physical/chemical quantities can be accessed by appropriate methods (e.g., chromatography, spectroscopy). The surge of industrial production required material characterization to become a routinely performed task on a commercial basis. However, it has remained a challenge to artificially design materials with predictable properties and characteristic responses to external stimuli. While design is possible on a large scale (architecture, craftsmanship) and on molecular scale (in-/organic synthesis), the field of nanofabrication (10 nm–10 µm) is not even seventy years old. Our world would look entirely different without the transistor revolution invoked by the advent of integrated circuits.[19] Semiconductor industry has pushed growth and etching processes to ever smaller scales and can be considered as one of the driving forces in nanotechnology. This progress is entirely built on the growing knowledge about the inherent processes attained by critical experimental and theoretical work.

Electrons treated as waves in the periodic potential of a (semiconductor) crystal lattice are not scattered from the nuclei if they meet certain criteria. An exception is the scattering from defects or grain boundaries that break the symmetry of the crystal. The degenerated energy states of separated single atoms split infinitesimally to form the quasi-continuous valence and conduction bands when organized in a macroscopic solid. For electrical conduction electrons must be excited into

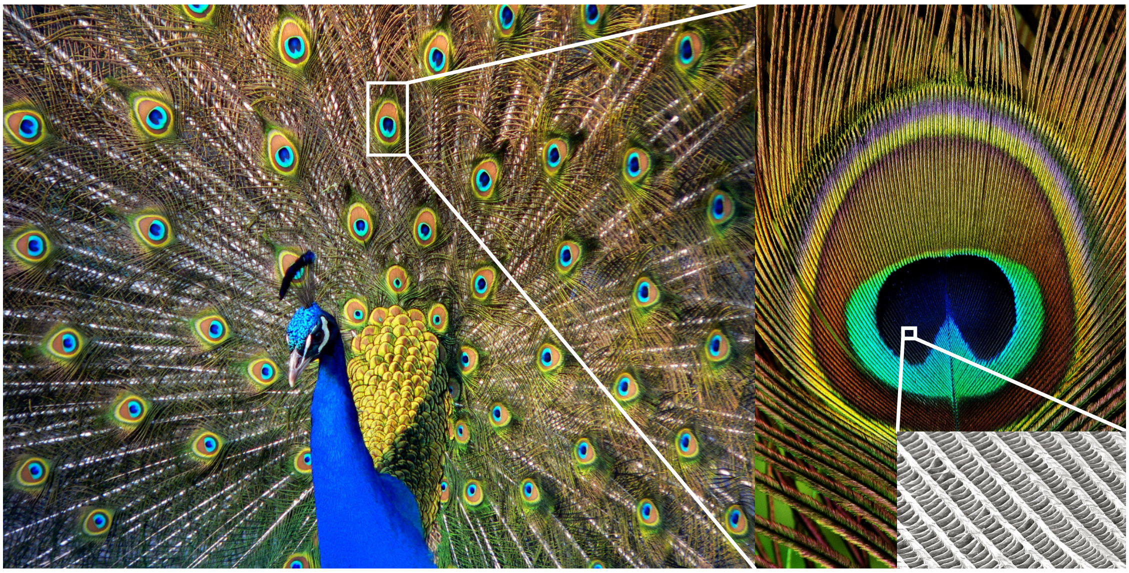

Figure 1.1: A male indian peafowl (*Pavo cristatus*) displaying. The interference color of the feathers is an example for a natural photonic crystal formed by regular inclusions of air. Reducing the optical mismatch by filling the interstices would result in a pale gray appearance. (adapted from Wikimedia Commons)

free states above the Fermi energy that is a measure of the filling level of the energy states. Valence and conduction bands overlap in metals (conductors) and are well separated in isolators, with the Fermi level between these two bands causing the electrical resistance as no electrons can be excited into the conduction band. The tiny energetic separation in semiconductors ($0.1 \leq 4\,\mathrm{eV}$) mainly causes their electronic resistance often referred to as "band gap". The *dispersion relation* $\omega(k)$ reflects the electronic band structure by relating energy with (quasi-)momentum of the electrons. Doping with auxiliary elements alters the band structure, such that electronic conduction can be individually tailored.

In a similar way, the introduced concepts are applicable to electro-magnetic waves, as well. No doubt, one of the most spectacular developments in the past decades is the field of *photonic crystals* (PhC's).[20,21] Characteristic for these systems is a periodic variation of the dielectric constant ϵ along at least one axis of periodicity. A prominent exponent is the feathering of peacocks, whose colors are purely due to interference from the regular pattern of air inclusions (Fig. 1.1). The most striking feature is the so called "photonic band gap", observed when the structure period a is in the order of magnitude of visible light. Light of a particular wavelength

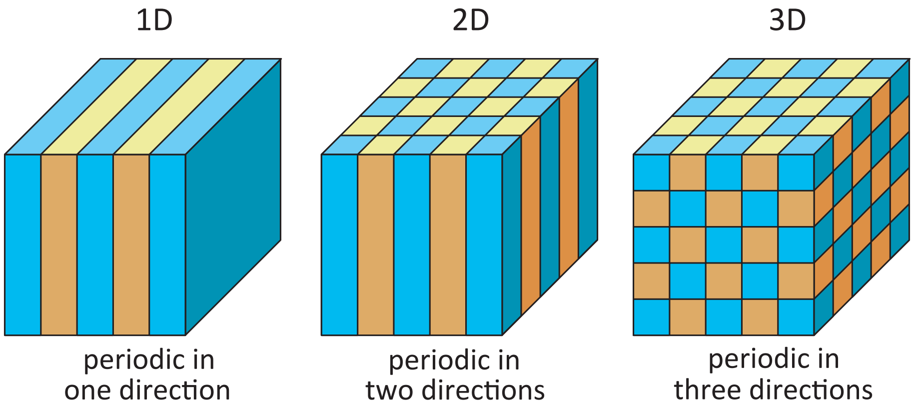

Figure 1.2: Schematic view of one-, two-, and three-dimensional photonic or phononic crystals. Different colors represent the two composing materials that have different dielectric constants or elastic impedance, respectively. Such crystal are predominantly defined is the periodicity of along one or more axes.

(frequency) cannot traverse the crystal as its amplitude decays evanescently into the PhC due to multiple destructive interferences of the incident and reflected beams. Hence, these photons are (Bragg) reflected and give rise to the iridescent colors. For the simplest case of one-dimensional (1D) structures the lattice period should be half the wavelength $a = \lambda/2$ to maximize this effect. The figure of merit is the width of the band gap $\Delta f/f$ discernible in the photonic dispersion relation and is determined by the relative thickness and the mismatch of refractive indices of the two composing materials.[22] As the periodicity is in the range of the wavelength of visible light (400–780 nm), the structures can be artificially created using nanofabrication techniques. Adjusting the geometrical parameters to tailor the propagation of light holds a wealth of applications. Instead of using light as probe for the purpose of analysis, the specific modification of the sample is employed to shape the properties of the probe beam after the interaction. Of course, the interplay of structure creation and subsequent analysis will play a paramount role in practice.

Photonic structures can be periodic in one, two, or three dimensions (Fig. 1.2), which is the fundamental difference to atomic lattices, that are inherently three-dimensional. 3D structures allow to observe complete photonic band gaps, i.e. an electromagnetic wave cannot pass the photonic crystal regardless of their angle of incidence. Prominent examples are the inverse opals,[23] and woodpile structures.[24,25] Two-dimensional structures, such as arrays of rods or holes (with different lattice symmetries) can be used for wave guiding along high curvatures in various ways.[26,27] The confinement of distinct modes in photonic crystal fibers with a hexagonal structure surrounding a hollow core is basically a 2D PhC.[28,29] Especially, one-dimensional photonic crystals find wide application due to the ease of fabrication. Few examples are dichroic mirrors and anti reflective coatings, with tunable passing bands. Also, the development of lasers hugely benefits from 1D PhC's that increase the reflectivity of the resonators and allow the single-mode operation by placing a Fabry-Pérot etalon inside the resonator. Even quasi-crystalline materials were shown to possess photonic band gaps.[30] The tunability of the photonic band structure and accelerated fabrication[31] opens pathways for application in data processing, i.e. integrated circuits that are switched by photons rather than electrons.

The concepts found for PhC's can be transferred to *phononic crystals* (PnC's) by replacing the relevant parameters, as theorized in 1993.[32,33] Instead of variations in the dielectric constant the variations of the acoustic impedance Z $(= \rho c_L)$ becomes important, that is the product of mass density ρ and (longitudinal) sound velocity c_L. The higher Z (or the proportional elastic moduli) the stiffer is the material and the faster travels an acoustic wave through the structure. At boundaries between two materials of different Z, elastic waves are reflected and can destructively interfere at frequencies of the *phononic band gap.* One of the first PnC's identified as such is the meter-sized sculpture "Organo" by E. Sempere (on display at the Juan March Foundation in Madrid), with an acoustic band gap at 1.67 Hz.[34] In principle, all effects found in PhC's are also present in PnC's, but now more materials parameters are involved as phonons propagate as full vector waves, and consequently require a higher (computational) effort to be correctly described by theory. Other than their electromagnetic analogs, elastic waves require a medium for propagation and in general one distinguishes between longitudinal and transverse polarization. Longitudinal waves, or pressure waves, with displacement of atoms (or volume elements) along the axis of propagation are basically pressure fluctuations and are supported by both solids and fluids. Transverse (or shear) waves, with displacement perpendicular to the propagation direction can only be observed in solids, as they need a non-zero shear modulus as the restoring force.

The realization of a PnC in the ultrasonic regime was first presented in 2D,[35] followed by a 3D example with a band gap at audible frequencies.[36] Shortly after this, absolute band gaps, i.e. independent of the direction of propagation were reported in two-dimensional structures.[37] Also, first evidence for hypersonic band gaps was found in two- and three-dimensional systems.[38,39] In 2006, the first hypersonic Bragg-type band gap was observed in self-assembled colloidal crystals made from polystyrene beads infiltrated with silicon oil.[40] Few years later, a second type of band gap was reported in a similar system.[41] The so called hybridization gaps arise from the anticrossing interaction of a localized mode (particle eigenvibration, cf. Section 1.3) with the longitudinal acoustic branch.[42] Hybridization due to localized modes stemming from the built-in resonant units were observed in dense-packed multiple-scattering colloidal suspensions.[43] Being an integral part of this thesis, one-dimensional phononic crystals are treated in Section 1.2.

The state-of-the-art techniques to determine the mechanical properties mainly rely on deformation, e.g. rheology (sub Hz to kHz regime) or nanoindentation. Higher frequencies (created by piezoelectric actuators[44]) are measured by ultrasound transmission experiments, with great success in studying the dispersion relation of mm-sized structures.[45] In pump-probe experiments the band structure is probed in the time-domain, either by reflectivity measurements or (superconducting) bolometers.[46] Today, the hypersonic (GHz) phononic dispersion relation of transparent dielectric materials is best measured using the non-destructive technique of Brillouin light scattering. This technique was largely used in this thesis and will be discussed in Chapter 2.3. A strong advantage of light scattering methods is their non-contact nature, which require no special sample preparation, hence have the potential to be used as in-line detection techniques. Photoelastic interaction allows to probe thermally activated phonons in transparent dielectric media. In opaque samples, the surface band structure can be measured in reflection.[47]

Recently, many exciting developments have boosted the role of high-frequency acoustics, yet hold plenty of space for further research. Few of them are highlighted in following lines, but the potential applications of phononic crystals are by far not yet fully explored. While this thesis might be a modest contribution to the study of their fundamentals, a lot more research from an engineering point of view is necessary to unveil possible new devices.

Alongside the further development of nanofabrication and based on theoretical studies started in 1960's,[48] so called acoustic metamaterials have evolved as an interesting new field.[49] With structural features smaller than the observed wavelengths these structures can have negative effective masses or moduli, which opens an entirely new perspective on materials science.[50,51] Peculiar phenomena are noticed, such as negative refraction by acoustic superlenses,[52,53] or acoustic cloaks[54,55] capable of hiding submarines from sonar. Squeezing the powerful functionality into micro-phononic crytals is the basis of a number of applications in the fields of wireless telecommunications or microelectromechanical systems (MEMS).[56]

Optomechanics are an interesting new development that exploit the advantages of interaction between electromagnetic and elastic energy.[57] A crystal that has the ability to mold the flow of light and sound simultaneously is often referred to as *phoxonic crystal* (PxC).[58–60] As the length scale of periodicity is fixed to the visible or near infrared wavelengths, PxC's are inherently hypersonic. Optomechanical coupling is reported in planar microcavities.[61–63] Laser cooling of mechanical motion into its quantum ground state has been exemplified in a nanoscaled oscillator[64,65] and whispering gallery resonators.[66] Further methods to interact with the acoustic field are provided by magnetostriction[67] or electrostriction using the electric field of high-power lasers. Recent works on stimulated coherent phonon emission aimed for the realization of the acoustic analog of a laser, sometimes referred to as *saser*.[68,69]

Heat conductivity in dielectrics is mainly based on phonons. However, a full understanding of the heat capacity of disordered systems (e.g., liquids and glasses) remains an unsolved problem. The characteristic discontinuities of the specific heat at the glass transition temperature is due to rearrangements that occur in the distribution of atoms.[70] The study of the dependence of glass transition on annealing, structure formation and geometry, enjoyed continuous interest, during the past decades.[71–77]

Control over (directionally unspecified) heat diffusion lies at the heart of the research on thermoelectric devices, that turn a temperature gradient into a potential gradient and vice versa. Suppressed heat conductance at constantly high electrical conductance, will increase their figure of merit ZT and will allow for a better conversion efficiency. 1D PnC's with a band gap in the frequency regime of thermal phonons were shown to reduce the thermal conductivity.[78–81] There's no doubt that PnC's will play a key role in thermal management, in the next years.

In the following two sections, I will provide a deeper insight into this thesis' subjects.

1.2. One-dimensional Phononics

Phononic crystals with periodicity along a single axis, sometimes called *superlattices*, have a long history. The term “superlattice” arises from the fact that similar rules apply as for crystal lattices. Here, a single layer (several nanometers thick) corresponds to an atomic layer (few Ångström thick) of a, e.g., *fcc*-crystal.

The theoretical foundations for the description of periodic systems laid by Floquet date back to the year 1883.[82] In 1928, based on Floquet’s theorem, Bloch described the wave function of electrons $\psi(\mathbf{x})$ in periodic potentials as represented by crystal lattices.[83] His general solution to Schrödinger’s stationary equation[84] reads

$$\psi_{n\mathbf{k}}(\mathbf{x}) = e^{i\mathbf{k}\cdot\mathbf{x}} \cdot u_{n\mathbf{k}}(\mathbf{x}), \tag{1.1}$$

with $\mathbf{k}$ being the wave vector and n the band index. Eq. (1.1) is essentially the product of a plane wave and a periodic function $u_{\mathbf{k}}(\mathbf{x}) = u_{\mathbf{k}}(\mathbf{x} + \mathbf{a})$ of period $\mathbf{a}$. It yields the frequency eigenvalues $\omega_n(\mathbf{k}) = \omega_n(\mathbf{k} + \mathbf{G})$, with $\mathbf{G}$ being the reciprocal lattice vector. The so called band structure $\omega(\mathbf{k})$ is then a collection of n energy eigenstates in the first Brillouin zone (BZ). This result is fundamental to any theory of periodic systems. A simple model applicable to the one-dimensional case was developed by Kronig and Penney, in 1931.[85] Initially set up for the energy of potential wells $V(x)$ representing a line of atoms, it can be used in a similar fashion to account for the spatially periodic fluctuation of the refractive index $n(x)$ or acoustic impedance $Z(x)$ in 1D photonic or phononic crystals, respectively (Fig. 1.3). A wave propagating perpendicular to the 1D structure will turn into a standing wave as $k_\perp$ approaches the edge of the 1st BZ. At this point ($k = G/2$), the group velocity being the slope of the dispersion curves, vanishes and a frequency gap opens up. At

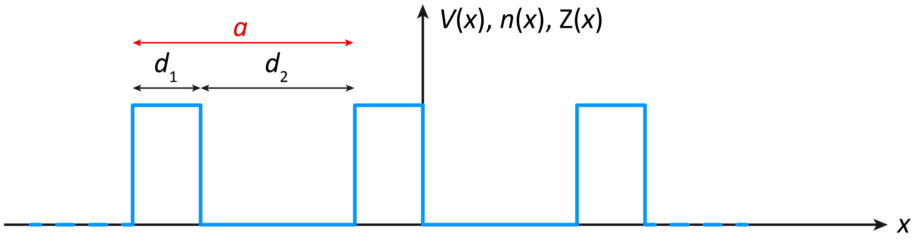

Figure 1.3: Illustration of the Kronig-Penney model,[85] a simplified description of the change of potential, refractive index or acoustic impedance in one-dimensional crystals.

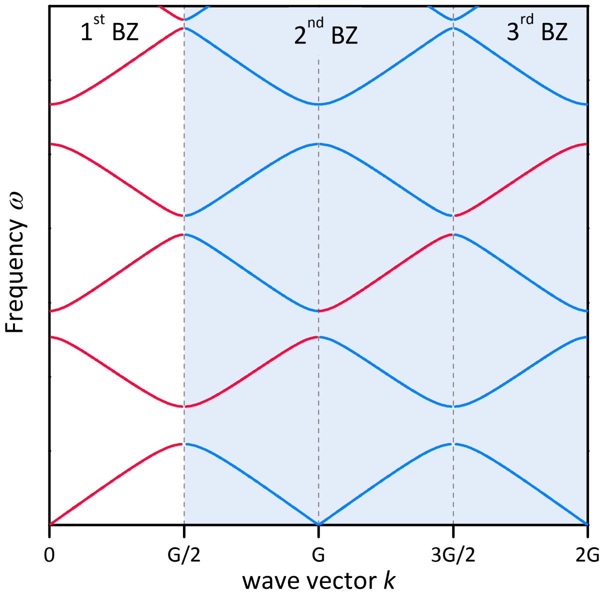

Figure 1.4: Phononic dispersion relation for an arbitrary one-dimensional crystal. Due to the uniaxial symmetry, the dispersion folds back into the 1stBrillouin zone.

higher k, the branches fold back to the 1st BZ due to momentum conservation as illustrated by the red lines in Fig. 1.4. The flat edge modes surrounding the band gap denote standing waves with amplitudes centered at regions of either high or low potential energy (or refractive index, acoustic impedance).

Due to the manifold of works published on (mostly semiconductor) superlattices (SLs), the following will be limited to elastic wave propagation in SLs. Layered media has long been of great interest,[86,87] often driven by the need to understand the propagation of seismic waves, up to these days.[88] With the miniaturization of artificially created structures this interest was renewed and experimental physics conquered ever higher frequency regimes. In the late 1970's, the existence of zone-folded phonons in semiconductor SLs was reported,[89–91] which stimulated further research in this growing field.[92–94] SLs became a widely used model system as the reduced dimensionality facilitates investigation of new phonon states and manipulation of phonon propagation in periodic structures.

Part II of this thesis is devoted to establish the use of soft matter for phononic devices, due to various advantages. PnC's made from polymers are light-weight and easily tunable by adapted chemistry. While classical growth techniques (e.g., molecular beam epitaxy) require clean-room facilities, polymer SLs can be rapidly

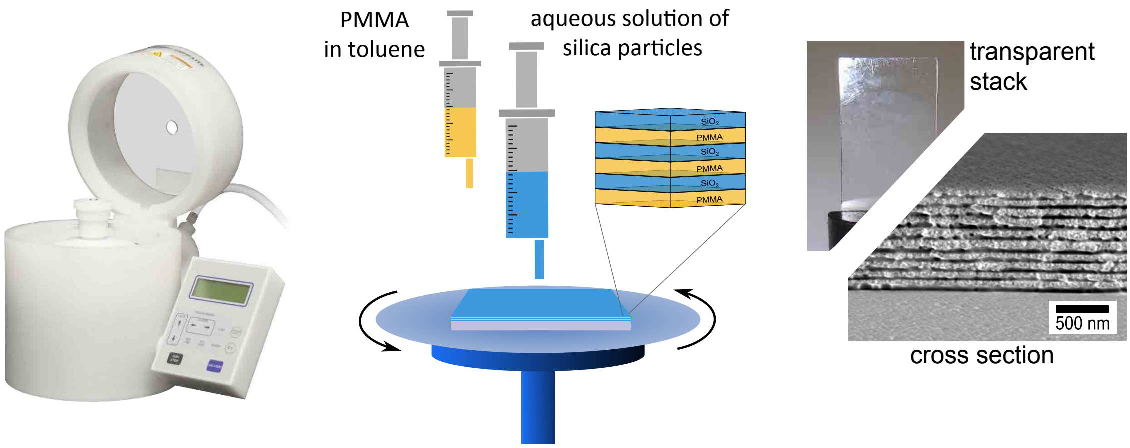

Figure 1.5: Hybrid superlattices are prepared by subsequent spincoating of a soft poly(methyl methacrylate) layer and a hard silica layer. After each coating cycle the whole stack was annealed until the finalized transparent stack with uniform lattice spacing is obtained.

produced at low costs using dip- or spincoating techniques (Fig. 1.5).[95–97] First steps onto this path were the observation of zone-folded phonons and in-plane layer excitations in porous silicon[98,99] and polymer[100,101] SLs using Brillouin and pump-probe time resolved spectroscopy. Triggered by the first direct observation of a sizeable hypersonic phononic band gap in hybrid SLs made from silica and poly(methyl methacrylate),[95] I want to expand my research based on that system.

In Chapter 3 the possibilities to engineer the phononic dispersion relation are highlighted. The gap size $\Delta f/f$ and its absolute position is adjusted by controlling the thicknesses of the composing layers. Density of states calculations provide full theoretical description of Brillouin spectra and dispersion relation yielding a unique estimation of elastic moduli. Although one-dimensional, the structures were designed in a 3D world, hence it is worthwhile to study the changes to the phononic dispersion as the propagation direction deviates from the normal axis. At oblique angles longitudinal and transverse modes interact with each other. Due to the mixing of polarization the bands shift, possibly closing or widening the band gap as a function of the angle of incidence.

SLs with embedded defect layers can be used to tailor the band structure according to specific requirements. Depending on their size and position additional modes will show up in the dispersion with their maximum displacement localized at characteristic positions in the SL. Defect modes either inside the frequency gaps of the zone-folded phonons[102–105] or with wave vectors in the vicinity of the center and edge of the BZ[106,107] have been revealed in semiconductors SLs. The interest in defect doped SLs is based on their role in applications such as coherent phonon generation and transmission,[69,94,108–110] concurrent modulation of light and sound,[58,61,111,112] acoustic diodes,[113] and reduction of heat conductivity.[114,115]

By exploiting the advantages of the proposed soft matter based platform we will be able to shed some light on the phonon dispersion in defected structures (Chapter 4). Due to the finite character of hybrid SLs, defect layers are in close vicinity and can "see" each other. Here, the first unambiguous evidence for the interaction of surface and cavity modes is reported. This analysis is powered by a Green's function formalism that allows for direct access to the density of states. The visualization of the displacement field enables the identification of the modes inside and near the edges of the 1st BZ that are activated through breaking of the high symmetry of undefected SLs. The insight gained with these fundamental studies is a precondition for reliable predictions of phonon propagation in periodic composite structures. New designs of nanostructures are anticipated to serve the demand for direction dependent propagation of elastic waves and optomechanical interactions at visible/hypersonic wavelengths.

1.3. Colloidal Systems

Colloidal science is a huge interdisciplinary field dealing with particles at the border between the nanoscopic and macroscopic world. In general, colloids are dispersed particles or droplets that scatter visible light, hence are of typical sizes between 10 nm and 10 µm. Due to their high surface/volume ratio, these particles can resist gravity and form stable suspensions. Popular examples are blood (erythrocytes dispersed in serum), milk (fat droplets dispersed in water) or fume (small particles dispersed in air). Today, the synthesis and functionalization of colloidal particles with desired properties and low size dispersion is well controlled. In principal, there is no limit in the choice of shape and materials (polymers, metals, oxides). Although harder to control, non-spherical shapes, e.g., rods,[116] cubes,[117] octahedrons[118] or ellipsoids[119] were successfully realized. Hierarchichally structured colloids, e.g. core-shell[120,121] or raspberry particles,[122] allow further control over the interaction with solvents or neighboring particles. Adjustment of surface charge, shape and size determines the inter-particle forces that are responsible for self-assembly. With their tunable properties, colloids provide a wide range of applications such as their uses in cosmetics, drug delivery or surface finishing. The particles used here were all artificially created by the mature methods of polymer science and material chemistry.[119,123–126]

From the perspective of elasticity isolated colloids are nanomechanical resonators that can store mechanical energy. Their shape fluctuations are described by eigenmodes with particular quantum numbers in analogy to molecular vibrations.[127] Brillouin light scattering (BLS) is a powerful tool to study the vibration dynamics, the "music", of submicron particles. The frequency of the resolved eigenmodes is independent of the exchanged scattering vector q, due to their resonant character. However, BLS selects a specific q, but due to multiple Mie scattering all wave vectors corresponding to angles from zero to backscattering contribute to the spectra. Hence, several modes are probed at once, only the number of resolved modes depends on the particle diameter. While for small particles ($d \leq 100\,\mathrm{nm}$) only the first few fundamental vibrations are observed, larger particles have rich spectra. In case of the latter, and in general at higher frequency, BLS peaks will be a sum of several contributions, therefore a profound theoretical description is needed. Calculations based on the eigenfunctions of freely vibrating homogenous spheres gave good agreement with experimental findings.[127,128] The assumption of no interaction is valid, as long as the contact area is negligible compared to the whole surface, as proven by related experiments on single spheres.[129] This model ceases to reflect the truth, if the contact of particles is increased.

In Chapter 5 we investigate the multiple processes affecting the eigenmode spectra using an adapted model, that allows interaction. At low particle diameter there is more contact area per total volume, which has effects on the sound velocity in clusters of particles and gives rise to a translational band not discernible in the spectra of large particles. Another way to increase the adhesion between particles is the thermal annealing around the glass temperature, which also increases the sound velocity due to the strengthened network.

Ordered assemblies of colloids are essentially 3D PnC's, however due to multiple scattering their phononic dispersion relation cannot be measured by light scattering. Infiltration of the systems with a liquid of similar refractive index suppresses the

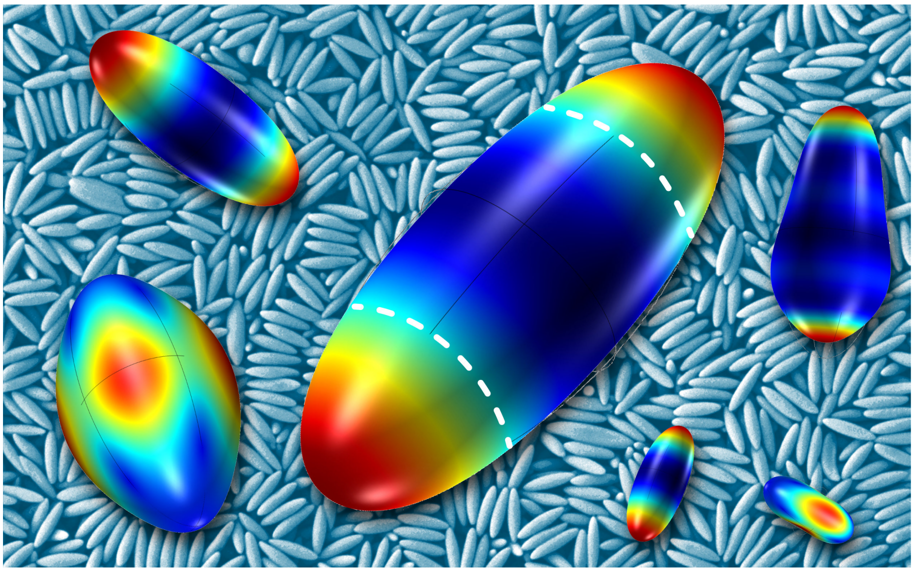

Figure 1.6: Artistic representation of colloidal vibration illustrated as the color-coded displacement calculated by finite elements method. (*Soft Matter* 9/2013, back cover)

perturbing scattering.[40,41] As the change of the matrix induces also an altered acoustic mismatch, as well as increased interaction through the stiffer medium, the obtained results are precious information for the analysis of phononic systems.

Quite infrequently, the building blocks of 3D PnC's are cubes arranged in a *bcc*-lattice, as suggested by Fig. 1.2. Rather, they are composed of a periodic network of beams[130] or (mostly spherical) particles forming *fcc* of random close packed lattices. Non-spherical particles bear the potential to construct anisotropic PnC's with unprecedented sound transmission characteristics. Obviously, the easiest way to reduce the crystals symmetry is to stretch it. This means the building units are no longer spherical but elongated (Figure 1.6), with severe consequences for the particle resonances. The evolution of resonance frequencies upon increased elongation can be tracked by Brillouin spectroscopy (Chapter 6). Due to the reduced symmetry the degeneracy of eigenmodes will be lifted and a multiple of eigenmodes can contribute to the spectra, thus hampering the identification of the individual modes. Nevertheless, it's worth to gather a solid knowledge of the non-spherical colloids, because it's them determining the macroscopic acoustic properties of a fused crystal.

1.4. Aims and Motivation

This work focuses on the propagation and localization of hypersound in soft periodic structures. A challenging aim is the mating of polymer science and condensed matter physics. While many concepts of phonon interaction have been studied theoretically in-depth by solid state physicists, the experimental demonstration has mostly been limited to well-controlled systems, such as the already mentioned semiconductor superlattices. On the other side, there are modern polymer and colloidal sciences providing a zoo of tunable materials with unprecedented properties.

Colloidal science succeeded to create regular nanostructured patterns from soft matter building units that was expectedly followed by the study of their hypersonic acoustic properties.[41,131] However, the manipulation of the phononic dispersion relation involves complex theoretic description and remains non-trivial for three-dimensional *fcc* colloidal crystals, let alone more exotic patterns. Hence, this work pursues a one-dimensional approach by using hybrid (soft matter composite) 1D phononic crystals to elucidate the response of the dispersion relation to the variation of mechanical properties, oblique incidence and introduction of defects.[96] The latter in particular has the potential to fortify the role of GHz acoustics, as it allows facile engineering of the phononic band structure by structural design, as will be demonstrated.[132]

Another motivation is the localization of sound in small objects. Due to the large elastic mismatch between nanoparticles and the surrounding air, elastic energy can be stored as resonant modes being confined in the particles. Their frequency and quality factor is intimately connected to the size,[127] shape,[133] interaction with neighboring spheres,[134] and surrounding matrix.[43] Furthermore, these eigenmodes can interact with the acoustic field of the effective medium and give rise to hybridization band gaps. Therefore, the study of non-spherical particles and the evolution of eigenmode spectra with increased aspect ratio is studied[135] with pertinent results being used to create anisotropic phononic crystals.

The strength of this interesting, yet not fully explored field lies also in the discovery of applications to control the flow of elastic energy. For example, miniaturized heat-guiding devices might change our everyday-life if waste heat could be efficiently recovered. The present contribution is also driven by the desire to advance this exciting evolution.

1.5. Outline of this Thesis

The thesis consists of three main parts as follows.

Part I contains the introduction to hypersonic phononics, peculiarities associated with and motivation for this work (this Chapter). An introduction to the theoretical details and the experimental and computational methods used is presented in Chapter 2.

Part II is dedicated to one-dimensional phononics. The phononic dispersion of hybrid superlattices as function of the lattice parameter and the direction of the probed wave vector is investigated in Chapter 3. The control over the band gap region by introduction of defect layers in finite superlattices and the interaction of defect modes is reported in Chapter 4.

Part III comprises the study of the mechanical properties of colloidal particles. The frequency and lineshapes of the particle eigenmodes are discussed as function of increased interaction in Chapter 5. The mode frequencies scale with the inverse diameter and the departure from spherical symmetry results in a complicated particle vibration spectrum. Chapter 6 addresses the lifting of mode degeneracy in uniaxially stretched polystyrene spheres. These particle have shown the ability to align in an AC field. The resulting spheroidal crystals exhibit anisotropic phononic properties, as highlighted in Chapter 7.

The epilog (Part IV) contains concluding remarks on the achieved results and the perspectives ahead.

2. Theory and Methods

This chapter presents a concise insight to the theoretical background needed to understand the results in chapter 3–7. At first the characteristics of elastic waves and their propagation will be outlined, followed by an introduction to some experimental and theoretical details.

2.1. Basics of Elasticity Theory

The first Section lays the foundation for the theoretical description of elasticity and wave propagation. The following excerpt sticks closely to the textbook by Landau and Lifshitz,[136] to be as concise as possible. The basic equation presented here were established by Cauchy and Poisson, already in the 1820's.[137–139]

2.1.1. Stress and strain

The theory of elasticity comprises the mechanics of solid bodies, which are regarded as continuous media (in that sense also liquids can be considered "solid"). Under an external force any solid body deforms to a certain extent. Hence, a convenient way to study elasticity is to look at this change of shape and/or volume. If we pick a particular point with position vector $\mathbf{x}$, we can allocate another vector $\mathbf{x}'$ after deformation. Then the displacement $\mathbf{u}$ is simply given by the difference of these two:

$$u_i = x_i' - x_i. \tag{2.1}$$

The distance between two arbitrary points in close vicinity is

$$\mathrm{d}l = \sqrt{\mathrm{d}x_1^2 + \mathrm{d}x_2^2 + \mathrm{d}x_3^2} = \sqrt{\mathrm{d}x_i^2}. \tag{2.2}$$

For convenience, the Einstein summation convention (right side of Eq. 2.2) is used. The distance after deformation can be expressed likewise and by the displacement from the initial position:

$$\mathrm{d}l' = \sqrt{\mathrm{d}x_i'^2} = \sqrt{\mathrm{d}x_i{}^2 + \mathrm{d}u_i{}^2} \tag{2.3}$$

After elimination of the square root and by using the substitution $\mathrm{d}u_i = (\partial u_i/\partial x_k)\mathrm{d}x_k$ we obtain

$$\mathrm{d}l'^2 = \mathrm{d}l^2 + 2\frac{\partial u_i}{\partial x_k}\mathrm{d}x_i\mathrm{d}x_k + \frac{\partial u_i}{\partial x_k}\frac{\partial u_i}{\partial x_l}\mathrm{d}x_k\mathrm{d}x_l. \tag{2.4}$$

The second term of Eq. 2.4 has its summation taken over both indices, therefore can be replaced by the symmetrical form $\left(\frac{\partial u_i}{\partial x_k} + \frac{\partial u_i}{\partial x_k}\right)\mathrm{d}x_i\mathrm{d}x_k$. If the indices i and l in the third term are interchanged we obtain for $\mathrm{d}l'^2$:

$$\mathrm{d}l'^2 = \mathrm{d}l^2 + 2u_{ik}\mathrm{d}x_i\mathrm{d}x_k, \tag{2.5}$$

with u_{ik} being the *strain tensor* defined as

$$u_{ik} = \frac{1}{2}\left(\frac{\partial u_i}{\partial x_k} + \frac{\partial u_k}{\partial x_i} + \frac{\partial u_l}{\partial x_k}\frac{\partial u_l}{\partial x_i}\right). \tag{2.6}$$

The last term of higher order can be neglected in case of small deformation $(\partial u_l/\partial x)$, typically applicable for two adjacent points (x,x'). As can be seen from its definition, the strain tensor is symmetrical $(u_{ik} = u_{ki})$, hence can be diagonalized with only the components u_{11}, u_{22}, and u_{33} being non-zero along the three axes, denoted by $u^{(i)}$ for simplicity. As the strain tensor can be diagonalized at any given point the length element $\mathrm{d}l'$ around this point can be expressed as

$$\mathrm{d}l'^2 = (\delta_{ik} + 2u_{ik})\mathrm{d}x_i\mathrm{d}x_k, \tag{2.7}$$

$$= (1 + 2u^{(i)})\mathrm{d}x_i^2. \tag{2.8}$$

Each of the (independent) strains is simply an extension or compression along the corresponding axis. Therefore, the relative extension is defined as

$$\frac{\mathrm{d}x_i' - \mathrm{d}x_i}{\mathrm{d}x_i} = \sqrt{1 + 2u^{(i)}} - 1 \approx u^{(i)}, \tag{2.9}$$

while the approximation is valid in almost all cases, as the change of distances in the body is typically small versus the distance itself.

Speaking about the forces being active during deformation of a body we first need to define a volume element before ($\mathrm{d}V$) and after deformation ($\mathrm{d}V'$). The deformation can be expressed in terms of the sum of the diagonal components $u_{ii} = u_{11} + u_{22} + u_{33}$:

$$\mathrm{d}V' = \mathrm{d}V(1 + u_{ii}). \tag{2.10}$$

Thus the relative volume change $(\mathrm{d}V' - \mathrm{d}V)/\mathrm{d}V$ is simply the trace of the strain tensor $\mathrm{tr}(u)$.

A non-deformed body in thermal equilibrium possesses no resulting forces in the volume $\mathrm{d}V$. If this state is disturbed, forces arise which are generally referred to as *internal stresses*. The total force is equal to the sum of all forces on all volume elements of a selected portion and is expressed as the volume integral $\int \mathbf{F}\mathrm{d}V$, with $\mathbf{F}$ being the force per unit volume. According to Newton's third law, any forces inside the volume element act on one another and are canceled out. Hence, only the forces on the surface of $\mathrm{d}V$ become important. The integral of the vector F_i (element of $\mathbf{F}$) is a second rank tensor, namely the *stress tensor* σ_{ik}. Hence F_i can be written as the divergence of σ_{ik}

$$F_i = \frac{\partial \sigma_{ik}}{\partial x_k}. \tag{2.11}$$

The transformation from volume to surface integral reads

$$\int F_i \mathrm{d}V = \int \frac{\partial \sigma_{ik}}{\partial x_k} \mathrm{d}V = \oint \sigma_{ik} \mathrm{d}S_k, \tag{2.12}$$

whereas $\sigma_{ik}\mathrm{d}S_k$ denotes the i^{th} component of the force on the surface $\mathrm{d}\mathbf{S}$. The surface elements that enclose the volume $\mathrm{d}V$ are defined by the normal vector along the x_k-axis. In a cartesian coordinate system σ_{xx} is the force on the surface perpendicular to the area, while σ_{yx} and σ_{zx} are tangential forces along the y- and z-axes, respectively (Fig. 2.1).

Stress and strain are always interconnected. From a thermodynamic point of view, the work $\mathrm{d}W$ done by internal stresses can be expressed in terms of the change in the strain tensor

$$\mathrm{d}W = -\sigma_{ik}\mathrm{d}u_{ik}. \tag{2.13}$$

Infinitesimal change of the internal energy $\mathrm{d}U$ is equal to the difference between acquired heat ($T\mathrm{d}S$) and the work performed by internal stresses ($\mathrm{d}W$). Thus we

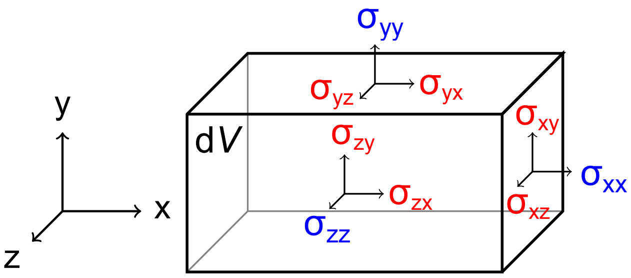

Figure 2.1: Schematic of the components of the stress tensor acting on the surface of the volume element dV. Normal and tangential forces are denoted in blue and red, respectively.

obtain the fundamental thermodynamic relation for deformed bodies

$$\mathrm{d}U = T\mathrm{d}S + \sigma_{ik}\mathrm{d}u_{ik}. \tag{2.14}$$

For hydrostatic compression the stress tensor is simply defined by $\sigma_{ik} = -p\delta_{ik}$, with p being the pressure and δ_{ik}, the Kronecker delta. As the volume change is the trace of u_{ik} (Eq. 2.10) the expression for the internal energy takes the usual form

$$\mathrm{d}U = T\mathrm{d}S - p\mathrm{d}V. \tag{2.15}$$

Due to the relations between the thermodynamic quantities stress and strain tensors can be written as derivatives of internal, Helmholtz free (A) and Gibbs free energy (G)

$$\sigma_{ik} = \left(\frac{\partial U}{\partial u_{ik}}\right)_S = \left(\frac{\partial A}{\partial u_{ik}}\right)_T, \tag{2.16}$$

$$u_{ik} = -\left(\frac{\partial G}{\partial \sigma_{ik}}\right)_T. \tag{2.17}$$

2.1.2. Hooke's law

Under sufficiently small stresses the amount of strain induced is proportional to the magnitude of the stress, and vice versa. For the simplest case of a bar under pure tensile stress the following identities represent Hooke's law,

$$\sigma = Cu; \qquad\qquad u = s\sigma, \tag{2.18}$$

whereas C denotes the elastic stiffness constant, while the inverse ($s = 1/C$) is the elastic compliance constant. In the aforementioned case C is equal to Young's modulus E and all following elucidation will be limited to C (the inverse results apply for s). In a more generalized approach for Eq. (2.18) C becomes a fourth rank tensor that relates the second rank tensors of stress and strain:

$$\sigma_{ij} = C_{ijkl} u_{kl}, \tag{2.19}$$

with C_{ijkl} comprising 81 elements (i,j,k,l $= \{1, 2, 3\} \rightarrow 3^4 = 81$) representing all stiffness constants of an arbitrary homogenous body. From the symmetry considerations of the stress and strain tensors found in section 2.1.1 (e.g., $\sigma_{12} = \sigma_{21}$) the following properties are deduced

$$C_{ijkl} = C_{jikl}, \tag{2.20}$$

and

$$C_{ijkl} = C_{ijlk}. \tag{2.21}$$

The abundance of equal elastic constants decreases the number of independent components from 81 to only 36. Furthermore, it allows the use of the more convenient matrix notation of the cumbersome fourth-rank tensor by using the substitution $C_{mn} = C_{ijkl}$ according to the rules given below.[140]

tensor indices (ij,kl)	11	22	33	23, 32	31, 13	21, 12
matrix indices (m,n)	1	2	3	4	5	6

with

$$\begin{aligned} C_{mn} &= C_{ijkl}, && \text{if } m \text{ AND } n \text{ are 1,2 or 3,} \\ C_{mn} &= \tfrac{1}{2} C_{ijkl}, && \text{if either } m \text{ OR } n \text{ is 4,5 or 6,} \\ C_{mn} &= \tfrac{1}{4} C_{ijkl}, && \text{if both } m \text{ AND } n \text{ are 4,5 or 6.} \end{aligned}$$

The (second rank) stress tensor is transformed as follows

$$\begin{pmatrix} \sigma_{11} & \sigma_{12} & \sigma_{13} \\ \sigma_{21} & \sigma_{22} & \sigma_{23} \\ \sigma_{31} & \sigma_{32} & \sigma_{33} \end{pmatrix} \rightarrow \begin{pmatrix} \sigma_{1} & \sigma_{6} & \sigma_{5} \\ \sigma_{6} & \sigma_{2} & \sigma_{4} \\ \sigma_{5} & \sigma_{4} & \sigma_{3} \end{pmatrix}, \tag{2.22}$$

whereas the strain tensor can be transformed in the same manner. Consequently, the stiffness tensor can be transformed to a 6 × 6 matrix C_{mn}

$$C_{ijkl} \rightarrow C_{mn} = \begin{pmatrix} C_{11} & C_{12} & C_{13} & C_{14} & C_{15} & C_{16} \\ C_{12} & C_{22} & C_{23} & C_{24} & C_{25} & C_{26} \\ C_{13} & C_{23} & C_{33} & C_{34} & C_{35} & C_{36} \\ C_{14} & C_{24} & C_{34} & C_{44} & C_{45} & C_{46} \\ C_{15} & C_{25} & C_{35} & C_{45} & C_{55} & C_{56} \\ C_{16} & C_{26} & C_{36} & C_{46} & C_{56} & C_{66} \end{pmatrix} \tag{2.23}$$

The stiffness matrix (2.23), depending on the crystal's symmetry, can be simplified. For the simplest isotropic case, applicable to many polymers, Hooke's law (2.19) reads:[140]

$$\begin{pmatrix} \sigma_1 \\ \sigma_2 \\ \sigma_3 \\ \sigma_4 \\ \sigma_5 \\ \sigma_6 \end{pmatrix} = \begin{pmatrix} C_{11} & C_{12} & C_{12} & 0 & 0 & 0 \\ C_{12} & C_{11} & C_{12} & 0 & 0 & 0 \\ C_{12} & C_{12} & C_{11} & 0 & 0 & 0 \\ 0 & 0 & 0 & C_{44} & 0 & 0 \\ 0 & 0 & 0 & 0 & C_{44} & 0 \\ 0 & 0 & 0 & 0 & 0 & C_{44} \end{pmatrix} \begin{pmatrix} u_1 \\ u_2 \\ u_3 \\ u_4 \\ u_5 \\ u_6 \end{pmatrix} \tag{2.24}$$

Here, only three elastic constants are necessary to represent the stiffness tensor. These are interconnected by the following equation:

$$C_{11} = C_{12} + 2C_{44}, \tag{2.25}$$

or

$$M = \lambda + 2G. \tag{2.26}$$

The two independent components C_{12} and C_{44} turn out to be the first (λ) and second ($\mu = G$) Lamé parameters, widely used in the theory of elasticity of isotropic materials. M is the longitudinal or P-wave modulus. Other frequently used parameters are Young's modulus E (cf. (2.18)), the bulk modulus K ($= p$, the pressure in ideal fluids) and the Poisson's ratio ν. The latter is defined by the length changes (transverse vs. axial) of a cube under axial strain (Fig. 2.2):

$$\nu = -\frac{\mathrm{d}u_{\text{trans}}}{\mathrm{d}u_{\text{axial}}} \approx \frac{\Delta L'}{\Delta L}. \tag{2.27}$$

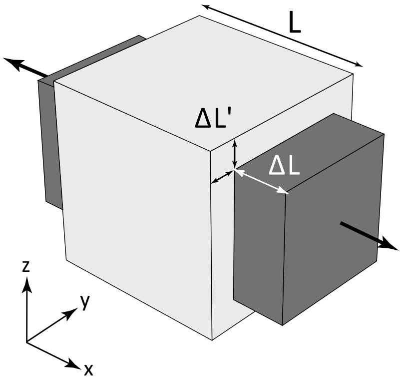

Figure 2.2: Schematic illustration of the definition of the Poisson ratio.

Any two of these elastic constants completely define a body's elastic properties. Hence, the conversion between them is frequently exercised and a summary of the respective relations is given in Tab. 2.1.

Table 2.1: Selection of frequently used conversion formulae of elastic parameters valid for homogenous linear elastic materials.

$f(a,b)$	λ, G	λ, ν	E, G	E, ν	G, ν	G, M
λ	λ	λ	$\frac{G(E-2G)}{3G-E}$	$\frac{E\nu}{(1+\nu)(1-2\nu)}$	$\frac{2G\nu}{1-2\nu}$	$M-2G$
G	G	$\frac{\lambda(1-2\nu)}{2\nu}$	G	$\frac{E}{2(1+\nu)}$	G	G
K	$\lambda+\frac{2G}{3}$	$\frac{\lambda(1+\nu)}{3\nu}$	$\frac{EG}{3(3G-E)}$	$\frac{E}{3(1-2\nu)}$	$\frac{2G(1+\nu)}{3(1-2\nu)}$	$M-\frac{4G}{3}$
E	$\frac{G(3\lambda+2G)}{\lambda+G}$	$\frac{\lambda(1+\nu)(1-2\nu)}{\nu}$	E	E	$2G(1+\nu)$	$\frac{G(3M-4G)}{M-G}$
M	$\lambda+2G$	$\frac{\lambda(1-\nu)}{\nu}$	$\frac{G(4G-E)}{3G-E}$	$\frac{E(1-\nu)}{(1+\nu)(1-2\nu)}$	$\frac{2G(1-\nu)}{(1-2\nu)}$	M
ν	$\frac{\lambda}{2(\lambda+G)}$	ν	$\frac{E}{2G}-1$	ν	ν	$\frac{M-2G}{2M-2G}$

2.2. Propagation of Elastic Waves

2.2.1. Elastic waves in isotropic media

The propagation of elastic waves is described by the equation of motion, that relates the internal stress force $\frac{\partial \sigma_{ik}}{\partial x_k}$ to the product of the acceleration $\frac{\partial^2 u_i}{\partial t^2}$ and the mass density ρ:

$$\rho \frac{\partial^2 u_i}{\partial t^2} = \frac{\partial \sigma_{ik}}{\partial x_k} \tag{2.28}$$

This general equation of motion is valid under the assumption that the velocity v of a point in the medium is equal to the derivative of its displacement $\frac{\partial u_i}{\partial t}$. Furthermore, any heat exchange due to transient density changes is neglected as the oscillatory motion is regarded fast (here, GHz) compared to heat diffusion. Hence, all elastic parameters must be replaced by their adiabatic values,[136] and one can write:

$$\rho \frac{\partial^2 \mathbf{u}}{\partial t^2} = G \nabla^2 \mathbf{u} + M \, \mathbf{grad} \, \mathrm{div} \, \mathbf{u}. \tag{2.29}$$

If we consider a plane wave traveling trough an isotropic medium, the deformation $\mathbf{u}$ will only be a function of x, and all off-x-axis derivatives will be zero. With that, we obtain for the axial and transverse components of the displacement $\mathbf{u}$ the following equations

$$\frac{\partial^2 u_x}{\partial x^2} - \frac{1}{c_\mathrm{L}^2} \frac{\partial^2 u_x}{\partial t^2} = 0, \qquad \frac{\partial^2 u_{y,z}}{\partial (y,z)^2} - \frac{1}{c_\mathrm{T}^2} \frac{\partial^2 u_{y,z}}{\partial t^2} = 0. \tag{2.30}$$

Here, we have introduced the longitudinal c_L and transverse c_T sound velocities:

$$c_\mathrm{L} = \sqrt{\frac{M}{\rho}}, \qquad c_\mathrm{T} = \sqrt{\frac{G}{\rho}}. \tag{2.31}$$

An elastic wave (2.29) is essentially composed of two independently propagating waves. The one with displacement only along the direction of propagation is the longitudinal wave, that involves compression and expansions of the body. Transverse waves have their displacement perpendicular to the direction of propagation and involve no change of volume. With this separation in longitudinal and transverse components the displacement reads

$$\mathbf{u} = \mathbf{u}_L + \mathbf{u}_T, \tag{2.32}$$

with the following properties, as discussed above

$$\mathrm{div} \, \mathbf{u}_T = 0, \qquad \mathbf{curl} \, \mathbf{u}_L = 0. \tag{2.33}$$

Finally, in the general case of an arbitrary elastic wave (not just plane) in an infinite medium (2.30) can be expressed as function of the sound velocities

$$\frac{\partial^2 \mathbf{u}}{\partial t^2} = c_{\mathrm{T}}^2 \nabla^2 \mathbf{u} + (c_{\mathrm{L}}^2 - c_{\mathrm{T}}^2)\,\mathbf{grad}\,\mathrm{div}\,\mathbf{u}. \tag{2.34}$$

2.2.2. Elastic waves in structured media

In arbitrarily structured media with anisotropic elastic properties, e.g. crystals, it is more complicated to derive the equation of motion. If we get back to (2.19) and (2.28) we obtain with some symmetry consideration the generalized equation of motion

$$\rho \frac{\partial^2 u_i}{\partial t^2} = C_{ijkl}\,\frac{\partial^2 u_m}{\partial x_k \partial x_l}. \tag{2.35}$$

To find a solution we use the wave equation of the form

$$u_i = u_{0i}\, e^{\mathrm{i}(\mathbf{k}\cdot\mathbf{r} - \omega t)}, \tag{2.36}$$

where the wave vector $\mathbf{k}$ and frequency ω are related such that (2.35) is satisfied. The spatial and temporal derivative results in multiplication with the factors $\mathrm{i}x_{k,l}$ and $-\mathrm{i}\omega$, respectively. With $u_i = \delta_{im} u_m$ (2.35) can be written after differentiation as

$$\rho\omega^2 \delta_{im} u_m = C_{ijkl}\, k_k k_l u_m. \tag{2.37}$$

Rearrangement of (2.37) yields a set of homogenous equations with the three unknowns u_x, u_y, u_z, whose non-zero solutions can be found if the determinant is set zero:

$$\left| C_{ijkl}\, k_k k_l - \rho\omega^2 \delta_{im} \right| = 0. \tag{2.38}$$

As (2.38) determines the relation between ω and $\mathbf{k}$, it is called “dispersion relation”. The equation is cubic in ω^2 with the three roots $\omega^2 = \omega_j^2(\mathbf{k})$ being different in the general 3D case and are often referred to as “branches”. If these roots are substituted back into (2.37) one can obtain the polarization directions of the three waves. These polarizations are mutually perpendicular and in the special case of an isotropic body they fall together with the longitudinal wave ($\omega = c_{\mathrm{L}} k$) and two independent transverse waves ($\omega = c_{\mathrm{T}} k$). The propagation velocity of the waves, i.e., the velocity of a wave packet (group velocity) is given by

$$\mathbf{v}_{\mathrm{group}} = \frac{\partial \omega}{\partial \mathbf{k}}. \tag{2.39}$$

The direction of propagation is in general different from $\mathbf{k}$. Only along the symmetry axes of a crystalline body one can find $\mathbf{v}$ and $\mathbf{k}$ pointing in the same direction. In the isotropic case $\omega(k)$ is always linear and the velocities $(c_{\mathrm{L}}, c_{\mathrm{T}})$ parallel to k.

To be concise we will limit the discussion of wave propagation in non-isotropic materials to the one-dimensional case.

2.2.3. The one-dimensional phononic crystal

More than half of this thesis deals with elastic wave propagation in one-dimensional composites. Here, we lay the theoretical foundation by looking at the simplest model system: a linear monatomic chain (Fig. 2.3). The position of the atoms is simply given by $\mathbf{r} = na$ and their displacement by $u(na)$, with n being an integer. With the constraint that only neighboring atoms can interact the harmonic potential is given by:[141]

$$U^{\mathrm{harm}} = \frac{1}{2} K \sum_{n} [u(na) - ([n+1]a)]^2, \tag{2.40}$$

whereas K denotes the spring constant. With the mass m we can write the equation of motion

$$m \frac{\partial^2 u(na)}{\partial t^2} = -\frac{\partial U^{\mathrm{harm}}}{\partial u(na)} = -K \left[2u(na) - u([n-1]a) - u([n+1]a) \right]. \tag{2.41}$$

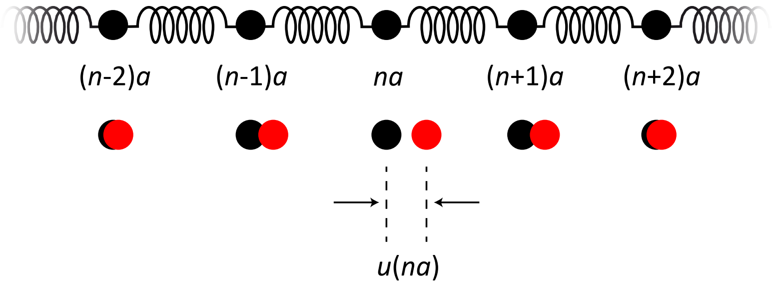

Figure 2.3: Linear chain of atoms connected by springs. The displacement from equilibrium position is given by $u(na)$.

Solving this equation with the Ansatz outlined in Section 2.2.2, the dispersion relation of the linear chain becomes

$$\omega(k) = 2\sqrt{\frac{K}{m}}\left|\sin\frac{ka}{2}\right|. \tag{2.42}$$

The periodic boundary condition $u(0) = u(Na)$ requires k to have the form

$$k = \frac{2\pi}{a}\frac{n}{N}, \tag{2.43}$$

with N being the total number of atoms. Thus we have N distinct values for k and (2.36) yields N independent solutions (modes). Hence, an arbitrary motion of the chain is completely determined by a set of N initial positions and N intitial velocities. Figure 2.4 illustrates the size effect. For a low number of chain atoms discrete values are found (red dots) while at high numbers the dispersion relation forms a continuous band. If the wavelength λ $(= 2\pi/k)$ is large compared to the spacing a, ω is linear in k just as in the isotropic case.

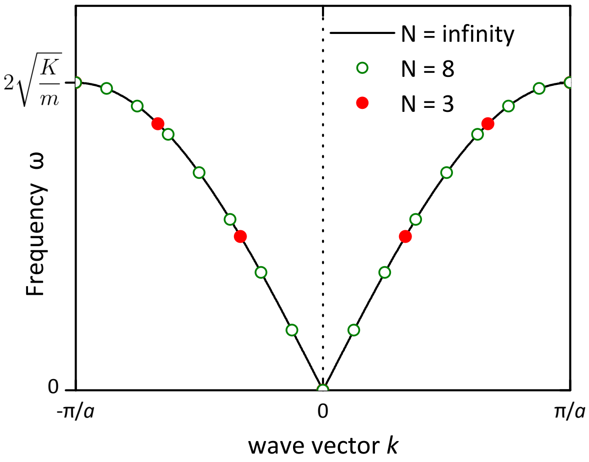

Figure 2.4: Dispersion relation for a monatomic chain in the 1$^{\text{st}}$ Brillouin zone.

Apart from the acoustic phonons discussed above, also optical phonons exist in crystals that are composed of two and more different kinds of atoms. The name of these modes is due to the fact that the frequencies in ordinary ternary crystals is in the near infrared and hence readily measured by Raman spectroscopy. In principle, they can be described as two sublattices vibrating out-of-phase (cf. Fig. 2.3 with two different atoms and/or spring constants). Optical branches show up with non-zero frequency at the zone-center, i.e. these modes are non-propagating excitations. For the systems studied in this thesis they play no important role.

2.2.4. The theory of interface response

The propagation of elastic waves in one-dimensional layered structures can be calculated using a Green's function formalism in the frame of elasticity theory. This allows to compute the phononic dispersion relation and density of states, whose knowledge is vital for the evaluation of the experimental results presented in Chapters 3 and 4. The theoretical framework needed, first presented by Green in 1828,[142] provides an important tool to solve inhomogeneous differential equations. Essentially, a Green's function describes the response to an external perturbation of a (quantum-) mechanical system, that is defined by initial and boundary conditions. In the interface response theory, the formalism is used for the solution of a set of linear inhomogeneous differential equations that represent the mechanical properties of (one-dimensional) composite materials.[143,144]

A composite system is described by several homogeneous parts joined together through their interfaces. A discrete infinite material i can be defined in the whole space D_∞ (Fig. 2.5a) and is composed of N homogeneous pieces situated in their respective domains D_i ($1 \leq i \leq N$). The interface of such a piece is denoted by M_i which can be bound to interface elements from an adjacent domain M_j ($1 \leq j \leq J$) through the sub-interface domains M_{ij}. Thus the interface area M_i is generally an element of J sub-interfaces (Fig. 2.5b). and their sum forms the interface space M. A homogenous infinite material i is described by its dynamical matrix

$$H_i = [(\omega^2 + \mathrm{i}\xi)I - H], \tag{2.44}$$

with ω being the eigenfrequency, $\mathrm{i} = \sqrt{-1}$, ξ an infinitesimally small positive number, I the identity matrix, and H denotes the classical Hamiltonian. The inverse of this matrix is the corresponding Green's response function G_i

$$H_i G_i = I. \tag{2.45}$$

The operators may be written as a matrix $H_i(X, X')$ whose elements are taken between different points in space X and X'.

To form a composite system, a small part is carved out of the infinite material. The corresponding subsystem D_i (Fig. 2.5b) is bound by the free surface space M_{ij} and with the cleavage operator V_{si} we can write

$$h_{si} = H_i + V_{si}. \tag{2.46}$$

The corresponding response function of the subsystem g_{si} is defined as

$$h_{si}\, g_{si} = I. \tag{2.47}$$

The corresponding bulk response function G_{si} of the truncated part is

$$H_{si}\, G_{si} = I. \tag{2.48}$$

The ideal-surface response operator is then defined as $A_{si} = V_{si}\, G_{si}$ and A_s will be the surface response operator of a composite system created from all independent blocks A_{si}. In a similar way, we can define the operator h_s formed out of every h_{si} of the independent subsystems with ideally cleaved free surfaces (and correspondingly $h_s g_s = I$). The independent parts are joined to become the composite system

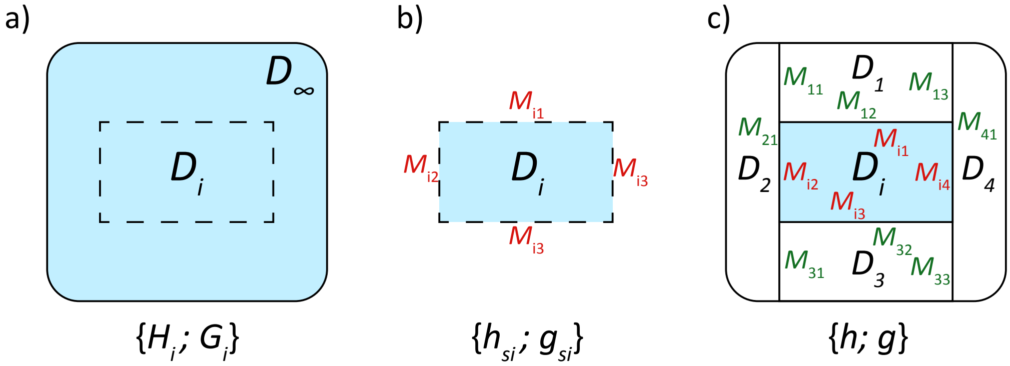

Figure 2.5: Schematic view of the formation of a composite system. a) From an infinite homogenous material i defined in D_∞ a finite piece is cut in its space D_i. b) This is bound by free interfaces described by sub-interface domains M_{ij}. c) After joining multiple subsystems, the whole composite system is obtained and characterized by the operator h and the response function g.

(Fig. 2.5c) by the coupling operator V_I and its operator h becomes

$$h = h_s + V_I. \tag{2.49}$$

The corresponding response function g of the composite system is related to the block diagonal reference response function G by

$$g(I + A) = G, \tag{2.50}$$

with $A = A_s + V_I G$. The interface response operator A has non-zero elements only between the points X of the interface space M and any point X' in the whole space D. Defining a rectangular matrix using the notation A(MD) we can write (2.50) as

$$g(DD) + g(DM)A(MD) = G(DD). \tag{2.51}$$

If the interface coupling operator V_I vanishes this equation becomes

$$g_s(D_iD_i) + g_s(D_iM_i)A_s(M_iD_i) = G(D_iD_i), \tag{2.52}$$

enabling the calculation of the response function of all independent subsystems $g_s(D_iD_i)$. In a more explicit form (2.51) reads

$$g_{si}(X, X') + g_{si}(X, X'')A_{si}(X'', X') = G_i(X, X'), \tag{2.53}$$

with $\{X, X'\} \in D_i$ and $\{X''\} \in M_i$. The matrices $g_{si}(X, X')$ defined in interface space $\{X, X'\} \in M_i$ are still matrices, but of smaller size than $g_s(M_iM_i)$, generally they are (3×3) matrices, with respect to the three dimensions $X = \{x, y, z\}$. In the case of a superlattice (SL) and for the sake of simplicity we consider only the case of phonon propagation normal to the layers. Due to the symmetry of translation along the layers (x, y) one can introduce a wavevector $k_\parallel$ parallel to the layers

$$k_\parallel = \mathbf{i}_x k_x + \mathbf{i}_y k_y, \tag{2.54}$$

with $\mathbf{i}_{x,y}$ being unit vectors along the specified direction, such that $g_s(M_iM_i|k_\parallel)$. Then, longitudinal and transverse waves are decoupled and the inverse elements of the interface Green's functions of the slabs (with two different materials) simply become (2×2) matrices

$$g_1^{-1}(M_iM_i) = \begin{pmatrix} a_1 & b_1 \\ b_1 & a_1 \end{pmatrix}, \qquad g_2^{-1}(M_iM_i) = \begin{pmatrix} a_2 & b_2 \\ b_2 & a_2 \end{pmatrix}, \tag{2.55}$$

with $a_i = \mathrm{i}\omega\rho c_\mathrm{L} \coth(-\mathrm{i}\omega d/c_\mathrm{L})$ and $b_i = \mathrm{i}\omega\rho c_\mathrm{L}/\sinh(-\mathrm{i}\omega d/c_\mathrm{L})$. Juxtaposition of the matrices (2.55) allows to construct the elements of the Green's function for the composite system (Fig. 2.6, right) in the entire interface space M

$$g^{-1}(MM) = g_s^{-1}(MM) + V_I, \tag{2.56}$$

with $g_s^{-1}(MM)$ being the block diagonal matrix formed out of all $g_s^{-1}(M_iM_i)$ (Fig. 2.6, left) and

$$g^{-1}(MM) = \begin{pmatrix} F_\mathrm{sub} + a_1 & b_2 & 0 & 0 & 0 & 0 & 0 \\ b_1 & a_1 + a_2 & b_2 & 0 & 0 & 0 & 0 \\ 0 & b_2 & a_2 + a_1 & b_1 & 0 & 0 & 0 \\ 0 & 0 & b_1 & a_1 + a_2 & b_2 & 0 & 0 \\ 0 & 0 & 0 & b_2 & a_2 + a_1 & b_1 & 0 \\ 0 & 0 & 0 & 0 & b_1 & a_1 + a_2 & b_2 \\ 0 & 0 & 0 & 0 & 0 & b_2 & a_2 \end{pmatrix}. \tag{2.57}$$

Thus, (2.57) uniquely represents any given multilayer systems, described by the thickness of each layer d, their mass density ρ and longitudinal sound velocity c_L. The boundary condition at the interface to the substrate $g_\mathrm{sub}^{-1}(0,0)$ is defined as $F_\mathrm{sub} = \mathrm{i}\omega\rho c_\mathrm{L}$.

In the interface response theory for a continuous composite material systems, the elements of the Green's function $g(DD)$ can be obtained via[145,146]

$$g(DD) = G(DD) + G(DM)\left[G^{-1}(MM)\,g(MM)\,G^{-1}(MM) - G^{-1}(MM)\right]G(MD), \tag{2.58}$$

whereas $G(DD)$ denotes the block diagonal bulk Green's function of the reference system and $g(MM)$ is the interface Green's function of the entire composite system (cf. Fig. 2.6).

For a SL with n repetition units, a unit cell composed of the two different materials

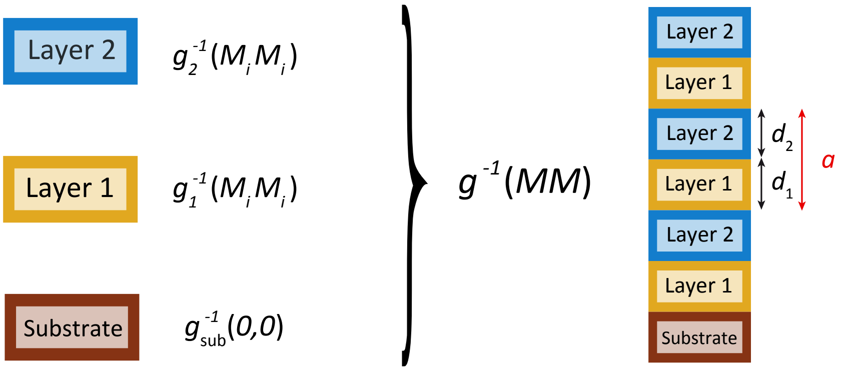

Figure 2.6: Schematic illustration of the construction of the Green's response function of a composite material (Eq. 2.57) by superposition of the interface response function of the individual layers $g_s^{-1}(M_iM_i)$ (Eq. 2.55).

i $(= 1, 2)$, and with Eq. 2.54 the elements of the Green's function take the following form

$$g_{\alpha\beta}(\omega^2, k_\parallel | n, i, z; n', i', z') \tag{2.59}$$

where α, β $(= 1, 2, 3)$ indicate the directions x, y and z, with z being the direction perpendicular to the layers. Any position in space M along the z-axis in medium i of unit cell n is denoted as (n, i, z). The local density of states at the interfaces can be calculated from the imaginary part of (2.59)

$$n_\alpha(\omega^2, k_\parallel | n, i, z) = -\frac{1}{\pi}\Im\left\{g_{\alpha\alpha}(\omega^2, k_\parallel | n, i, z; n, i, z)\right\}. \tag{2.60}$$

Here, α $(= 3)$ is the z-component in the case of pure longitudinal modes. Integration over z and summation over n, i.e. over all interfaces of the SL, yields the structure's total density of states

$$n_{\text{total}}(\omega^2) = \sum_i \sum_n \int_{-d_i/2}^{d_i/2} n_\alpha(\omega^2 | n, i, z) \mathrm{d}z. \tag{2.61}$$

Therefore, the corresponding g_{11} (hence, n_1), and g_{22} (hence, n_2) give the transverse vertical and transverse horizontal components of the modes, respectively. The new interface states, i.e. the dispersion relations, of propagating and localized modes can be calculated from the following determinant[145]

$$\det\left[g^{-1}(\mathrm{MM})\right] = 0. \tag{2.62}$$

That means for the calculation of a SLs interface states, one only needs to know the inverse of the Green's function of each individual layer in the space of their respective interfaces.

Finally, the interface response theory allows the determination of the eigenvectors $E\ (= \omega^2 + \mathrm{i}\xi)$ of a composite system associated with the corresponding eigenvalues. Therefore, we consider the matrix operator (cf. Eq. 2.44)

$$h = EI - H, \tag{2.63}$$

with I being the identity matrix and H a Hamiltonian. If the force on the system is zero, the eigenvalues E and the corresponding eigenvector $u(D)$ are given by the diagonalization of (2.63). If the force is non-zero, the direct calculation is complicated, since h becomes a matrix of large dimension. Instead, we can use the result of (2.58) wich allows us to calculate the displacement field (denoted as row vector $|u(D)\rangle$) at any point inside the composite material[146]

$$\begin{aligned} |u(D)\rangle = {} & |U(D)\rangle - |U(M)\rangle\, G^{-1}(MM)G(MD) \\ & + |U(M)\rangle\, G^{-1}(MM)g(MM)G^{-1}(MM)G(MD). \end{aligned} \tag{2.64}$$

$|U(D)\rangle$ represents the displacement field of the reference medium. In the particular case of a supported SL, $|U(D)\rangle$ is a bulk propagating wave launched inside the homogeneous substrate ($z = -\infty$).

Hence, the interface response theory becomes a powerful tool to calculate the dispersion relation, mode displacements and light scattering spectra (Section 2.3.3) of any layered material. This freedom to adapt the theoretical representation is particularly useful for the description of SLs with designed defects (Chapter 4). The density of states will be shown to be very sensitive to changes in spacing or elastic moduli of the layers.

In the generalized case of an infinite SL, the dispersion relation is well represented by the following analytical expression[86,91]

$$\cos(ka) = \cos\left(\frac{\omega\, d_1}{c_{\mathrm{L},1}}\right)\cos\left(\frac{\omega\, d_2}{c_{\mathrm{L},2}}\right) - \frac{1}{2}\left(\frac{Z_1}{Z_2} + \frac{Z_2}{Z_1}\right)\sin\left(\frac{\omega\, d_1}{c_{\mathrm{L},1}}\right)\sin\left(\frac{\omega\, d_2}{c_{\mathrm{L},2}}\right) \tag{2.65}$$

with $Z(=\rho\, c_L)$ being the longitudinal elastic impedance, c_{L} being longitudinal sound velocity and $d_{1,2}$ being the thickness of the two layers. The lattice spacing is given by $a = (d_1 + d_2)$ and k is the Bloch wave vector.

2.3. Inelastic Light Scattering

In this Section, the concepts of inelastic light scattering are introduced, in particular we will focus on the use of light scattering for the study of acoustic properties. While the latter can be readily analyzed in the sonic and ultrasonic frequency regime, an investigation of GHz acoustics (the hypersonic regime) is usually non-trivial as they are beyond the reach of piezo-electric transducers. Fortunately, this frequency range can be covered by light scattering, since the wavelengths of visible light are of the same order of magnitude as the acoustic waves at hypersonic frequencies. The elastic motion of materials is a sensitive probe to the mechanical properties and relaxation rates a high frequencies. The length scale under study (10 nm–10 µm) is of particular interest as it falls together with the dimensions in modern nanoscience. Hence, probing acoustic phonons by means of light scattering is of utter importance and contributes to state-of-the-art materials science by providing complementary information, not available by conventional mechanical testing methods.

2.3.1. Fundamentals of light scattering

While the theory of light scattering is typically developed by quantum field theory, its results differ only little from those obtained by the classical theory of light scattering. In the semimacroscopic view, light scattering is essentially a result of local fluctuation in the dielectric constant,[147] which fully satisfies the description of our experiments. In short, the electromagnetic field of an incident beam is considered to exert a force on the charges inside an arbitrary scattering volume. The acceleration of charges in turn gives rise to emission of radiation – the scattered light. Thus the incident light polarizes the material and produces scattered light in every volume element. If the object is optically homogeneous, i.e. has the same dielectric constant, the wavelets scattered in each volume element are identically, but are different in phase due to their spatial separation. Therefore, destructive interference will cause annihilation of any scattered light, except in the direction of the incident beam. On interfaces of different dielectric constant, the scattered light is no longer identical, therefore no complete cancellation occurs.

Due to the ubiquitous thermal motion, the local dielectric constant $\boldsymbol{\epsilon}(\mathbf{r},t)$ is always fluctuating around its equilibrium value ϵ_0 and can be expressed as a second rank tensor

$$\boldsymbol{\epsilon}(\mathbf{r},t) = \epsilon_0 \mathbf{I} + \delta\boldsymbol{\epsilon}(\mathbf{r},t), \tag{2.66}$$

with $\mathbf{I}$ being the unit tensor and $\delta\boldsymbol{\epsilon}(\mathbf{r},t)$ the dielectric fluctuation at position $\mathbf{r}$ and time t. The incident electric field is represented by a plane wave of the following form

$$\mathbf{E}_i(\mathbf{r},t) = \mathbf{n}_i E_0 e^{\mathrm{i}(\mathbf{k}_i\cdot\mathbf{r}-\omega_i t)}, \tag{2.67}$$

with $\mathbf{n}_i$ being the unit vector in the direction of the incident field (the polarization). $\mathbf{r}$ and t denote the position and time, whereas $\mathbf{k}_i$ and ω_i denote the wave vector and angular frequency of the incident light. Electrodynamics demand that the total electric field $E = E_i + E_s$ always satisfies Maxwell's equation. The same applies for the magnetic $\mathbf{H}$ and electrical displacement field $\mathbf{D}$. After its lengthy derivation,[148] the scattered far-field (seen by the detector) at distance $\mathbf{R}$ from the scattering volume with polarization $\mathbf{n}_s$, and wave vector $\mathbf{k}_s$ becomes

$$E_s(R,t) = \frac{E_0}{4\pi R\epsilon_0}\, e^{\mathrm{i}k_s R} \int_V d^3r\, e^{\mathrm{i}(\mathbf{q}\cdot\mathbf{r}-\omega_i t)} \left[\mathbf{n}_s\cdot \left[\mathbf{k}_s \times (\mathbf{k}_s \times (\delta\boldsymbol{\epsilon}(\mathbf{r},t)\cdot\mathbf{n}_i)\right]\right], \tag{2.68}$$

whereas $\int_V$ denotes the integral over the entire scattering volume. The scattering vector $\mathbf{q} = \mathbf{k}_s - \mathbf{k}_i$ is defined by the scattering geometry (Fig. 2.7). The angle between $\mathbf{k}_s$ and $\mathbf{k}_i$ is the scattering angle θ. Using the definition of the scalar product and having in mind the quasielasticity ($|\mathbf{k}_s| \approx |\mathbf{k}_i|$) we can write

$$q^2 = k_i^2 + k_s^2 - 2\mathbf{k}_i \cdot \mathbf{k}_s = 2k_i^2(1-\cos\theta) = 4k_i^2 \sin^2\frac{\theta}{2}. \tag{2.69}$$

With $k_s = k_i = 2\pi n/\lambda$ and the refractive index $n = \sqrt{\epsilon_0}$ we obtain the Bragg condition

$$q = 2k_i \sin\frac{\theta}{2} = \frac{4\pi n}{\lambda}\sin\frac{\theta}{2}. \tag{2.70}$$

With its spatial Fourier transform, the dielectric fluctuation becomes a function of q

$$\delta\boldsymbol{\epsilon}(\mathbf{q},t) = \int_V d^3r\, e^{\mathrm{i}\mathbf{q}\cdot\mathbf{r}}\, \delta\boldsymbol{\epsilon}(\mathbf{r},t), \tag{2.71}$$

and (2.68) can be expressed as

$$E_s(R,t) = \frac{E_0}{4\pi R\epsilon_0} e^{\mathrm{i}(k_s R-\omega_i t)} \left[\mathbf{n_s}\cdot\left[\mathbf{k}_s \times \mathbf{k}_s \times (\delta\boldsymbol{\epsilon}(\mathbf{q},t)\cdot\mathbf{n}_i)\right]\right]. \tag{2.72}$$

By working out the vector products, it can be simplified to[148]

$$E_s(R,t) = \frac{-k_s^2 E_0}{4\pi R\epsilon_0} e^{\mathrm{i}(k_s R-\omega_i t)} \delta\epsilon_{is}(\mathbf{q},t), \tag{2.73}$$

with

$$\delta\epsilon_{is}(\mathbf{q},t) \equiv \mathbf{n}_s\cdot\delta\boldsymbol{\epsilon}(\mathbf{q},t)\cdot\mathbf{n}_i \tag{2.74}$$

being the component of the dielectric constant fluctuation tensor along the polarization directions before and after the scattering event. The time-correlation of the

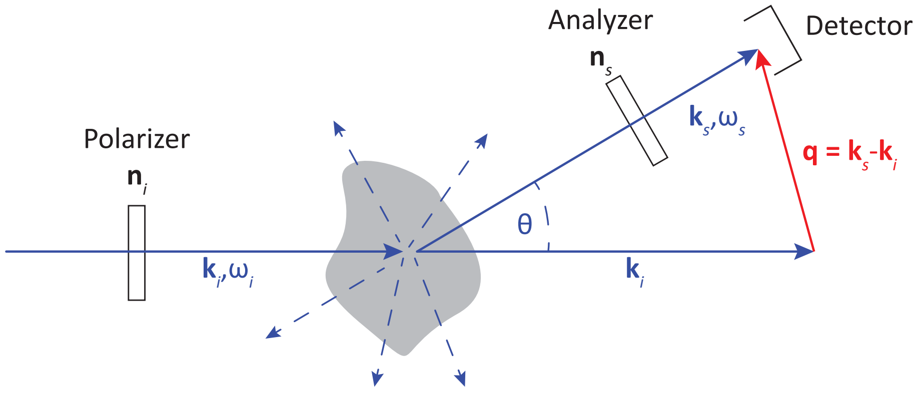

Figure 2.7: Schematic view of a general light scattering setup. An incident light beam of polarization $\mathbf{n_i}$, frequency ω_i, and wave vector $\mathbf{k_i}$ is scattered. Although the scattering is omnidirectional (dashed arrows), only the light with $\mathbf{n}_s$ and $\mathbf{k}_s$ can reach the detector after passing the analyzer. The scattering vector $\mathbf{q} = \mathbf{k}_s - \mathbf{k}_i$ shown in red is defined by the scattering geometry.

scattered field can be evaluated from (2.73)

$$\langle E_s^*(R,0)E_s(R,t)\rangle = \left(\frac{k_s^2|E_0|}{4\pi R\epsilon_0}\right)^2 \langle \delta\epsilon_{is}^*(\mathbf{q},0)\delta\epsilon_{is}(\mathbf{q},t)\rangle\, e^{-\mathrm{i}\omega_i t}, \tag{2.75}$$

and the spectral intensity reads as follows

$$\begin{aligned} I_{is}(\mathbf{q},\omega_s,R) &= \int_{-\infty}^{+\infty} e^{\mathrm{i}\omega_s t} dt\, \langle E_s^*(R,0)E_s(R,t)\rangle \\ &= \left[\frac{I_0 k_s^4}{16\pi^2 R^2 \epsilon_0^2}\right] \frac{1}{2\pi} \int_{-\infty}^{+\infty} dt\, \langle \delta\epsilon_{is}^*(\mathbf{q},0)\delta\epsilon_{is}(\mathbf{q},t)\rangle\, e^{\mathrm{i}(\omega_s-\omega_i)t}, \end{aligned} \tag{2.76}$$

with $I_0 = |E_0|^2$. Three important conclusions can be drawn from (2.76):
i) It reflects the inverse λ^4 dependence $I_{is} \propto \lambda^{-4}$ (k^4), i.e. the fact that light of shorter wavelength is subject to stronger scattering, as prominently shown by the blue of the sky. ii) The inverse R^2 dependence $I_{is} \propto R^{-2}$ simply accounts for the attenuation of spherical wave via the inverse-square law. iii) The scattered intensity depends on ω_i and ω_s solely by their difference $\omega = \omega_s - \omega_i$. A change in frequency can occur only if $\delta\boldsymbol{\epsilon}(\mathbf{q},t)$ varies with time, otherwise the scattering will be purely elastic.

Thus, for a given experiment (i.e., constant prefactor in Eq. 2.76) the light scattering spectrum directly measures the fluctuation of the local dielectric constant via

$$I_{is}(\mathbf{q},\omega) \propto \int_{-\infty}^{+\infty} dt\, \langle \delta\epsilon_{is}^*(\mathbf{q},0)\delta\epsilon_{is}(\mathbf{q},t)\rangle\, e^{\mathrm{i}\omega t}. \tag{2.77}$$

The advent of lasers enabled experimental observation of the spectral shape $I(q,\omega)$, that hasn't been possible before due to the lack of sufficiently monochromatic light sources. The phonon frequencies measured in this work are in the GHz-range, while the frequency of the probing light itself is in the THz-range, hence high-resolution spectrometers are needed to resolve the tiny frequency shift of this quasi-elastic scattering. But also with the limitation of low resolution, the evaluation of the total (frequency integrated) intensity by static light scattering

$$I_{is}(\mathbf{q}) \propto \left\langle |\epsilon_{is}(\mathbf{q})|^2 \right\rangle, \tag{2.78}$$

bears important information, such as the structure factor $S(q)$ (cf. Eq. 2.87).

As seen from the above outline, any scattering event can be regarded in terms of conservation of momentum and energy. A photon either looses or gains energy and momentum by interaction with the scattering volume.

$$(\pm)\hbar\omega = \hbar\omega_s - \hbar\omega_i, \tag{2.79}$$

$$(\pm)\hbar\mathbf{q} = \hbar\mathbf{k}_s - \hbar\mathbf{k}_i. \tag{2.80}$$

For Brillouin light scattering this means a phonon is either created ($\Delta E_{\text{photon}} = -\hbar\omega$) or annihilated ($\Delta E_{\text{photon}} = +\hbar\omega$) with a wavevector k_{phonon} equal to the scattering vector q. The connection between the quantities ω and q is described by the (phononic) dispersion relation $\omega(q)$, which in our experiments serves as a unique probe of composite materials structural composition, elastic parameters and wave propagation characteristics.

2.3.2. Brillouin light scattering

Inelastic scattering of light from thermally activated sound waves with frequencies in the GHz range is generally referred to as Brillouin light scattering (BLS). The striking feature of each BLS spectrum is the appearance of the symmetric Brillouin doublet, already predicted in 1922.[149] Other than in Raman spectroscopy, where almost only the ground state is occupied, the energy of hypersonic phonons is well below the thermal energy $k_B T$ (at 298 K), with k_B being Boltzmann's constant. The occupation number for phonons (which are bosons) is expressed as

$$\langle n \rangle = \frac{1}{e^{\hbar\omega/(k_B T)} - 1}. \tag{2.81}$$

Figure 2.8 illustrates that quantum states at frequencies typically probed by BLS (few GHz) are well occupied, even at low temperatures. Hence, the Stokes (phonon excitation) and anti-Stokes (annihilation) processes are of similar probability, i.e., their peaks have the same intensity.[150] According to (2.39) and (2.80) the frequency of the incident light ω_i undergoes the Doppler shift

$$\omega_s = \omega_i \pm c_{\mathrm{L,T}}\, q, \tag{2.82}$$

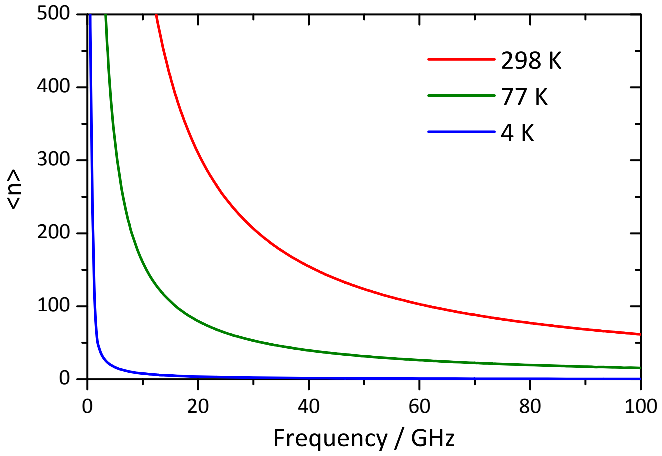

Figure 2.8: Occupation number $\langle n \rangle$ as function of phonon frequency and temperature.

as it is scattered from the hydrodynamic modes within a fluid. $c_{\mathrm{L,T}}$ denotes the longitudinal (transverse) sound velocity and q is the exchanged wave vector. This very basic finding is important for most of the experiments, where we are only interested in the phonon frequency, in order to derive the elastic properties and map the dispersion relation of new materials. Deeper insight to the processes involved in BLS is provided by the elucidation of the spectral features. To clarify the origin of the scattered intensity we need to go back to (2.77). In the simple case of a monatomic fluid which has no off-diagonal elements in the dielectric fluctuation $\delta\boldsymbol{\epsilon}_{\alpha\beta}(\mathbf{q},t) = \boldsymbol{\epsilon}(\mathbf{q},t)\delta_{\alpha\beta}$ the spectral intensity is represented by the scattering formula

$$I_{is}(\mathbf{q},\omega) = (\mathbf{n}_i \cdot \mathbf{n}_s)^2 \underbrace{\frac{1}{2\pi}\int_{-\infty}^{+\infty} dt\, \langle \delta\epsilon^*(\mathbf{q},0)\delta\epsilon(\mathbf{q},t)\rangle\, e^{\mathrm{i}\omega t}}_{S(\mathbf{q},\omega)}\,. \tag{2.83}$$

BLS probes dielectric fluctuations of wavelengths in the range of $q^{-1} \sim 100\,\mathrm{nm}$ that is considerably higher than the intermolecular separation. These fluctuations rather involve collective motion of numerous molecules, that can be described by the macroscopic laws of physics, such as thermodynamics and hydrodynamics. In general, the dielectric constant of a fluid in equilibrium is a function of density ρ and temperature T, which is expressed in the dielectric equation of state

$$\delta\epsilon(\mathbf{r},t) = \left(\frac{\partial\epsilon}{\partial\rho}\right)_T \delta\rho(\mathbf{r},t) + \left(\frac{\partial\epsilon}{\partial T}\right)_\rho \delta T(\mathbf{r},t). \tag{2.84}$$

The derivatives can be determined experimentally by the variations of ϵ with density and temperature. Combining (2.83) and (2.84) the spectral intensity becomes

$$\begin{aligned} I_{is}(\mathbf{q},\omega) = (\mathbf{n}_i \cdot \mathbf{n}_s)^2 \Bigg\{ & \left(\frac{\partial\epsilon}{\partial\rho}\right)^2_{T_0} S_{\rho\rho}(\mathbf{q},\omega) \\ & + \left(\frac{\partial\epsilon}{\partial\rho}\right)_{T_0} \left(\frac{\partial\epsilon}{\partial T}\right)_{\rho_0} \left[S_{\rho T}(\mathbf{q},\omega) + S_{T\rho}(\mathbf{q},\omega)\right] \\ & + \left(\frac{\partial\epsilon}{\partial T}\right)^2_{\rho_0} S_{TT}(\mathbf{q},\omega) \Bigg\}, \end{aligned} \tag{2.85}$$

whereas $S_{\alpha\beta}(\mathbf{q},\omega)$ denotes the spectral densities of the respective correlation funcitions $\langle \delta\alpha^*(\mathbf{q},0)\delta\beta(\mathbf{q},t)\rangle$. In most practical cases the temperature dependence of the fluctuations in ϵ are negligible and (2.85) simplifies to

$$I_{is}(\mathbf{q},\omega) = (\mathbf{n}_i \cdot \mathbf{n}_s)^2 \left(\frac{\partial\epsilon}{\partial\rho}\right)^2_{T_0} S_{\rho\rho}(\mathbf{q},\omega). \tag{2.86}$$

Thus the scattered intensity essentially reflects the autocorrelation of the local density fluctuation $\delta\rho(\mathbf{q},t)$. The total integrated intensity is then proportional to the structure factor

$$S(\mathbf{q}) = \left\langle |\delta\rho(\mathbf{q})|^2 \right\rangle, \tag{2.87}$$

which is the mean-square fluctuation of q^{th} Fourier component of the density fluctuations. Since q^{-1} is large compared to intermolecular distances, the q-dependence can be ignored and $S(\mathbf{q})$ is shown to be proportional to the mean-square fluctuation of the number of particles in the scattering volume

$$\lim_{q\to 0} S(\mathbf{q}) = \left\langle |\delta N|^2 \right\rangle, \tag{2.88}$$

$$= V\rho^2 k_B T \chi_T. \tag{2.89}$$

With equality (2.89) that follows from statistical fluctuation theory and χ_T being the isothermal compressibility, the integrated intensity is given by[147]

$$I_{is}(\mathbf{q}) = (\mathbf{n}_i \cdot \mathbf{n}_s)^2 \left(\frac{\partial\epsilon}{\partial\rho}\right)^2_{T_0} V\rho^2 k_B T \chi_T. \tag{2.90}$$

This formula is fundamental for the understanding of BLS as it reports the observed intensity being

i) strong for polarized scattering (VV),
ii) independent of the scattering angle θ (except for the slight change of the scattering volume with θ),
iii) and proportional to density fluctuations of the dielectric constant $(\frac{\partial\epsilon}{\partial\rho})^2_T$, the square number density ρ^2, and the isothermal compressibility $\chi_T = \frac{1}{\rho}(\frac{\partial\rho}{\partial p})^2_T$.

While (2.90) gives good account for the experimentally observed total intensity, it does not specify to what extent the central unshifted line (Rayleigh) and the Brillouin doublet contribute to the spectrum. The dielectric equation of state (2.84) can also be expressed as function of other independent thermodynamic quantities, such as entropy S and pressure p

$$\delta\epsilon(\mathbf{r},t) = \left(\frac{\partial\epsilon}{\partial S}\right)_p \delta S(\mathbf{r},t) + \left(\frac{\partial\epsilon}{\partial p}\right)_S \delta p(\mathbf{r},t). \tag{2.91}$$

The first term of (2.91) describes the isobaric entropy fluctuations, which are non-propagating and account for the intensity of the central line I_c. The latter similarly accounts for the adiabatic pressure fluctuations which are propagating sound waves that give rise to the Brillouin doublet $2I_B$. After a lengthy derivation,[136,148] the spectral density of the Rayleigh-Brillouin spectrum in (2.86) is given as a sum of Lorentzians

$$\begin{aligned} S_{\rho\rho}(\mathbf{q},\omega) =& \frac{1}{\pi}\rho^2 k_B T \chi_T \Bigg\{ \underbrace{\left(1-\frac{1}{\gamma}\right)\left(\frac{D_T q^2}{\omega^2+[D_T q^2]^2}\right)}_{\propto I_C} \\ &+ \underbrace{\frac{1}{\gamma}\left(\frac{\Gamma q^2}{[\omega-\omega(q)]^2+[\Gamma q^2]^2} + \frac{\Gamma q^2}{[\omega+\omega(q)]^2+[\Gamma q^2]^2}\right)}_{\propto 2I_B} \\ &+ \frac{b(q)}{\gamma}\left(\frac{[\omega+\omega(q)]}{[\omega+\omega(q)]^2+[\Gamma q^2]^2} - \frac{[\omega-\omega(q)]}{[\omega-\omega(q)]^2+[\Gamma q^2]^2}\right)\Bigg\}, \end{aligned} \tag{2.92}$$

with γ being the specific heat ratio $\gamma = C_p/C_V = \chi_T/\chi_S$. D_T is the thermal diffusivity $D_T = \kappa/(\rho C_p)$, with termal conductivity κ. The term in the first line of (2.92) represents the central Rayleigh line with the full-width at half maximum (FWHM) $\Delta\omega_C(q) = 2D_T q^2$. The two terms in the central line denote the Brillouin doublet with frequency shift $\pm\omega_B = \pm c_S q$ (c_S being the adiabatic velocity of sound) and linewidth (FWHM)

$$\Delta\omega_B(q) = 2\Gamma q^2 = \Bigg[\underbrace{\frac{\eta_v + \frac{4}{3}\eta_s}{\rho}}_{D_V} + \frac{\kappa(\gamma - 1)}{\rho C_P}\Bigg] q^2, \tag{2.93}$$

whereas Γ is the classical attenuation coefficient of sound, while η_v and η_s denote the bulk and shear viscosities, respectively. The last line of (2.92) is non-Lorentzian and normally a very small contribution, that shifts the apparent Brillouin peaks towards the center. The prefactor is $b(q) = q[3\Gamma - D_V/(\gamma c_S)]$, whereas D_V is the longitudinal kinematic viscosity (cf. Eq. 2.93).

The relation between the intensity of the central and Brillouin lines is known as the Landau-Placzek ratio

$$\frac{I_C}{2I_B} = \frac{\chi_T - \chi_S}{\chi_S} = \frac{C_p - C_V}{C_V} = \gamma - 1. \tag{2.94}$$

It follows from the above equation that if isobaric and isochoric heat capacity are not much different (e.g., in water) no Rayleigh line will be observed.

The experimental width of BLS peak comprises many contributions, such as absorption, phonon scattering (on phase boundaries), and intermolecular relaxations that reduce the lifetime of phonon, thereby increase the width $\Delta\omega$. Detailed knowledge of all contributions is necessary for physically relevant deconvolution processes, which in practice is hardly achieved. Only the q-dependence of $\Delta\omega$ is always present (in Newtonian fluids) and due to Navier-Stokes equations[148] we obtain $\Delta\omega \propto q^2$. The inherent line width of Brillouin signals (2.93) increases with the viscosity and thermal conductivity. Another source of line broadening in composite systems is due to scattering of phonons on interfaces (grain boundaries, structural imperfections), i.e. the finite size of crystallites can limit the effective mean free path of phonons.

2.3.3. Longitudinal acoustic phonons in 1D superlattices

This section is devoted to the computation of the BLS spectra of 1D hybrid superlattices (SLs) studied in Chapter 3 and 4. Based on the calculation of the density of vibrational states (DOS) and photo-elastic coupling between material displacements and refractive index fluctuations, the spectral density can be deduced. Utilization of the Green's function technique and the theory of interface response in the frame of elasticity theory allows to calculate the density of states $n(\omega, k)$ and the displacement field (Section 2.2.4). The dispersion relations of propagating and localized modes are given by the determinant of the inverse Green's function $\det[\mathbf{g}^{-1}(MM)]$ in the interface space M, that uniquely represents the mechanical properties of a given SL (Eq. 2.62). If an acoustic phonon propagates in the multilayer structure it causes a periodic variation of strain, which in turn induces a modulation of the dielectric tensor ϵ_{ij} through the photo-elastic coupling to elastic fluctuations

$$\delta\epsilon_{ij} = \epsilon_{ii}\epsilon_{jj} \sum_{kl} P_{ijkl} \frac{1}{2} \left(\frac{\partial u_k}{\partial x_l} + \frac{\partial u_l}{\partial x_k} \right). \tag{2.95}$$

P_{ijkl} are the elements of the photoelastic tensor and can be considered a function of z (along the axis of periodicity). Here, we consider the electromagnetic field polarized along the x-direction and wave propagation along z with $\{x, y, z\} = \{1, 2, 3\}$. Hence, for each medium α, described by longitudinal sound velocity c_L, density ρ and refractive index $n_\alpha = \sqrt{\epsilon_\alpha}$ we can write the photoelastic constant as

$$p_\alpha = -\epsilon_\alpha^2 P_{1133}^\alpha, \tag{2.96}$$

and consequently

$$\delta\epsilon_\alpha = p_\alpha \frac{\partial u_\alpha(z)}{\partial z}. \tag{2.97}$$

The calculations consider the modulation $\delta\epsilon$ caused by the displacement due to strain, sometimes referred to as the opto-mechanical effect. In finite structures another contribution to $\delta\epsilon$ has to be taken into account. Eq. (2.98) gives the modulation $\delta\epsilon^{'}$ caused by the displacement of the interfaces, which is in our case negligible except at the surface

$$\delta\epsilon^{'} = \sum_\alpha \left(\epsilon_\alpha - \epsilon_{\alpha+1}\right) \left\{\theta(z - z_\alpha) - \theta(z - z_\alpha - u_z(z_\alpha))\right\}, \tag{2.98}$$

with θ denoting the Heaviside step function and z_α being the position of the interface between layers α and $\alpha + 1$.

The coupling between incident photons $E_i(z', t)$ and thermally activated phonons in a SL is the source of the scattered field $E_s(z,t)$ from the composite system, whereas z' (z) denotes the space inside (outside) the SL/air system. After a lengthy derivation,[151] and using the Green's function method (cf. Eq. 2.59), the scattered field after interaction of E_i with a SL can be obtained as follows[146]

$$E_s(z,t) = \frac{\omega_i^2}{\epsilon_0 c^2} \sum_\alpha \int p_\alpha G(z,z') \frac{\partial u_\alpha(z')}{\partial z'} E_i(z',t) \mathrm{d}z'. \tag{2.99}$$

Here, ω_i denotes the frequency of the incident field and c is the vacuum velocity of light. $G(z,z')$ is the Green's function associated with the propagation of an electromagnetic field along the z-direction in the SL in absence of any elastic deformation. Note, that the theoretical representation of $E_s(\omega, q_\perp)$ in (2.99) is performed with regard to the elastic and optical modulation of the layers.

The dielectric modulation of the multilayer structure can be neglected when the layers are thin as compared to the probing optical wavelength. The same is true if the layers are characterized by almost the same refractive indices. This particular case applies for the systems in Chapter 3 and 4, that can be considered as homogeneous media from the optical point of view (except at the surface). Instead of being a Bloch wave, the incident electric field in the medium then becomes a simple plane wave

$$E_i(z',t) = E_i^0 e^{\mathrm{i}k_i z'}, \tag{2.100}$$

and the Green's function can be written as

$$G(z,z') \propto e^{\mathrm{i}k_s(z-z')}. \tag{2.101}$$

With the definition of the scattering vector $q_\perp = k_s - k_i$ the scattered field $E_s(\omega, q_\perp)$ becomes

$$E_s(\omega, q_\perp) \propto \sum_\alpha \int e^{iq_\perp z'} p_\alpha \frac{\partial u_\alpha(z', \omega)}{\partial z'} \mathrm{d}z'. \tag{2.102}$$

Consequently, the Brillouin intensity is given by the square of Eq. (2.102)

$$I_s(\omega, q_\perp) = |E_s(\omega, q_\perp)|^2 \tag{2.103}$$

Momentum conservation at the frequencies of the Brillouin doublet requires that all partial waves are scattered coherently. Hence, in the case of a large (or infinite)

SL the scattered intensity from all layers interferes constructively and the corresponding spectral line should be narrow and well pronounced. However, in real systems there are a few sources of line broadening, such as interfacial roughness and structural incoherence. The thickness fluctuations of individual layers are not explicitly handled in this presentation as they have only marginal effects on the Brillouin spectra, as being studied in Section 3.3.4. All sources of broadening, including the instrumental function, were accommodated by the convolution with a Lorentzian.

In summary, theoretical Brillouin spectra are computed using the Green's function technique in the frame of elasticity theory. With the knowledge of the SL's response function, and hence the displacement field, we can calculate the Brillouin intensity as function of the scattering vector. Finally, the spectra are broadened to account for the instrumental function.

2.3.4. Eigenmode spectra of submicron particles

BLS usually measures the frequency of propagating phonons with the dispersion $\omega(q)$. However, this quantity from which group and phase sound velocities, as well as frequency gap formation can be deduced is not accessible in turbid media. Such multiply scattering samples appear as white powders and the exchanged wave vector $q(\theta)$ can adopt any value between forward- and backscattering ($0° < \theta < 180°$), therefore we speak of q being ill-defined. This apparent disadvantage of incoherent scattering can be exploited for the determination of q-independent (localized) resonance modes arising from the spatial confinement of elastic energy. Due to the strong scattering integrated over all possible q-values, one readily obtains the *vibrational eigenmode spectrum* of the individual particles. These rich BLS spectra contain a wealth of information about the particles, such as their diameter, shape, elastic moduli, and effects of interaction (Chapter 5 and 6).

This section intends to give a concise description of the mathematical representation of eigenmodes, first derived by Lamb for freely vibrating spheres.[152] Here, a more generalized approach is chosen that allows energy leakage into the matrix, which becomes important for infiltrated colloidal films (Chapter 7). This coupling of eigenmodes to the propagating acoustic waves causes broadening of the resonance lines and diminishes the character of individual particles as function of elastic impedance mismatch. Dry films of particles in air that exhibit a large impedance contrast render the boundary-condition quasi-stress-free and the results will coincide with those of Lamb. The modes are indexed by (p,n,l,m), whereas the parameter p specifies the polarization of the modes as spheroidal (s) or torsional (t). The latter involves only shear, i.e. they evoke no volume change, hence cannot be seen by BLS. In analogy to atomic orbitals, the quantum number n denotes the n^{th} radial component of vibrations and l, m denote the angular momentum quantum numbers.

For the description of particle vibrations, it is beneficial to use the spherical-wave solution of the elastic wave equation for isotropic media (2.29). Using spherical coordinates the displacement can be given as the sum of the vectors

$$\mathbf{u} = \mathbf{l} + \mathbf{m} + \mathbf{n}, \tag{2.104}$$

and we obtain three independent Helmholtz equations[131]

$$\left(\nabla^2 + k_L^2\right)\mathbf{l} = 0, \quad \left(\nabla^2 + k_T^2\right)\mathbf{m} = 0, \quad \left(\nabla^2 + k_T^2\right)\mathbf{n} = 0. \tag{2.105}$$

The displacement associated with a longitudinal wave is represented by $\mathbf{l}$, while $\mathbf{m}$ and $\mathbf{n}$ account for two orthogonal transverse waves. These vectors can be written as gradients of scalar potential functions (φ, ψ, χ) that satisfy the respective scalar Helmholtz function $(\nabla^2 + k_{L,T}^2)(\varphi, \psi, \chi) = 0$

$$\mathbf{l} = \frac{1}{k_L}\nabla\varphi, \quad \mathbf{m} = \nabla \times \mathbf{r}\,\psi, \quad \mathbf{n} = \frac{1}{k_T}\nabla \times \nabla \times \mathbf{r}\,\chi. \tag{2.106}$$

Here, the transverse displacements remain independent of $\mathbf{l}$ and were expressed as the `curl` and `curl curl` of the product of position vector $\mathbf{r}$ and the scalar vector functions. A well-known solution of the scalar Helmholtz function takes the form

$$f_{lm}(r, \theta, \phi) = R_l(kr)\,Y_{lm}(\theta, \phi), \tag{2.107}$$

where $Y_{lm}(\theta, \phi)$ denote the spherical harmonics (the Legendre polynomials) with $l = 0, 1, 2, \ldots$ and m assumes integer values from $-l$ to $+l$. The radial functions $R_l(kr)$ are the n^{th} order Bessel functions and independent of l. With that, the solutions for the vectors in (2.105) read as follows

$$\mathbf{l}_{lm}(R, k_L) = \frac{1}{k_l}\nabla\left[R_l(k_L r)Y_{lm}(\hat{r})\right], \qquad l = 0, 1, 2, 3, \ldots, \tag{2.108}$$

$$\mathbf{m}_{lm}(R, k_T) = \nabla \times \left[\mathbf{r}R_l(k_T r)Y_{lm}(\hat{r})\right], \qquad l = 1, 2, 3, \ldots, \tag{2.109}$$

$$\mathbf{n}_{lm}(R, k_T) = \frac{1}{k_T}\nabla \times \nabla \times \left[\mathbf{r}R_l(k_T r)Y_{lm}(\hat{r})\right], \qquad l = 1, 2, 3, \ldots, \tag{2.110}$$

whereas monopole waves ($l = 0$) exist only as longitudinal solutions $\mathbf{l}_{lm}$, which are the so called “breathing” modes with purely radial displacement.

When a elastic wave strikes a particle we can divide the total displacement field in three contributions, namely the unimpeded incident wave $\mathbf{u}^{\text{inc}}$, the scattered wave $\mathbf{u}^{\text{scatt}}$ and the elastic excitation inside the sphere $\mathbf{u}^{\text{in}}$. For the derivation of eigenmodes, the displacement field inside $\mathbf{u}^{\text{in}}$ and outside $\mathbf{u}^{\text{out}}$ the particles needs to be the same. This boundary condition requires the continuity of stress and strain at the surface $r = r_s$, such that

$$\mathbf{u}^{\text{in}}(\mathbf{r}_s) = \mathbf{u}^{\text{out}}(\mathbf{r}_s) = \mathbf{u}^{\text{inc}}(\mathbf{r}_s) + \mathbf{u}^{\text{scatt}}(\mathbf{r}_s), \tag{2.111}$$

$$\mathbf{p}^{\text{in}}(\mathbf{r}_s) = \mathbf{p}^{\text{out}}(\mathbf{r}_s) = \mathbf{p}^{\text{inc}}(\mathbf{r}_s) + \mathbf{p}^{\text{scatt}}(\mathbf{r}_s). \tag{2.112}$$

(2.112) represents the boundary condition for the surface traction, i.e. the force per unit area $p_i = \sigma_{ik}n_k$ with stress tensor σ_{ik} and $\mathbf{n}$ being the outbound unit vector normal to the sphere surface. With (2.104) and (2.108–2.110) the three waves can be expanded into vector spherical harmonics and we obtain

$$\mathbf{u}^{\text{inc}}(\mathbf{r}) = \sum_{lm}\left\{a^1_{lm}\mathbf{l}^m_{lm}(R_l, k^{\text{out}}_L) + a^2_{lm}\mathbf{m}_{lm}(R_l, k^{\text{out}}_T) + a^3_{lm}\mathbf{n}_{lm}(R_l, k^{\text{out}}_T)\right\}, \tag{2.113}$$

$$\mathbf{u}^{\text{scatt}}(\mathbf{r}) = \sum_{lm}\left\{b^1_{lm}\mathbf{l}^m_{lm}(R'_l, k^{\text{out}}_L) + b^2_{lm}\mathbf{m}_{lm}(R'_l, k^{\text{out}}_T) + b^3_{lm}\mathbf{n}_{lm}(R'_l, k^{\text{out}}_T)\right\}, \tag{2.114}$$

$$\mathbf{u}^{\text{in}}(\mathbf{r}) = \sum_{lm}\left\{c^1_{lm}\mathbf{l}^m_{lm}(R_l, k^{\text{in}}_L) + c^2_{lm}\mathbf{m}_{lm}(R_l, k^{\text{in}}_T) + c^3_{lm}\mathbf{n}_{lm}(R_l, k^{\text{in}}_T)\right\}. \tag{2.115}$$

The coefficients a^i_{lm} are related to b^i_{lm} (i=1,2,3) via the boundary conditions and should be known for a given incident wave. Hence, the above equation can be decomposed into six independent scalar equations with the coefficients b^i_{lm} and c^i_{lm}. This system can be further broken to two subsystems, one involving the coefficients

b_{lm}^2 and c_{lm}^2 of the vector $\mathbf{m}_{lm}$ and another involving the remaining four coefficients that correspond to $\mathbf{l}_{lm}$ and $\mathbf{n}_{lm}$. With the orthonormality over Y_{lm}, each of the six equations can be decomposed into l equations. In practice, the calculations are performed with a limited number of l to handle the computational demand. The two subsystems account for the torsional modes ($\mathbf{m}_{lm}$) and spheroidal modes ($\mathbf{n}_{lm}, \mathbf{l}_{lm}$), respectively. In the case of a sphere the eigenmodes are degenerate in m, but mix with the torsional modes if particles loose their spherical symmetry (Chapter 6). For every l the determinant vanishes only for a discrete set of modes $\omega_{n,l}$, where n denotes the branch number. For the scattered waves $\mathbf{u}^{\text{scatt}}(\mathbf{r})$, a different Bessel function R'_{lm} has to be used that diverges at $r = 0$ and accounts for the exclusion of the sphere's origin.[153]

2.4. BLS Instrumentation

The description of the experimental design in this section is intended to be as concise as possible. Therefore, we first have a look on the integral part necessary to detect small frequency changes. Laser interferometry is widely used to monitor subtle frequency shifts and probably the most impressive demonstration is the use of the giant interferometer LIGO (4 km mirror distance) for the detection of gravitational waves.[154,155] Basically, a Fabry Pérot interferometer (FPI) makes uses of multiple interference of light inside an etalon. The latter is composed of two highly reflective mirrors, typically coated with thin films of dielectric materials or metals (Ag, Al) on thick (for stability) optical flats, mounted perfectly parallel to each other. Parallelism is maintained by piezoelectric actuators.

Figure 2.9 illustrates the multiple reflections of the incident light. The path length difference L between different beams that exit the etalon depends on the mirror distance d and the refractive angle α_r

$$L = 2nd\cos\alpha_r. \tag{2.116}$$

Due to numerous reflections, the light is subject to destructive interference at $\alpha_r \sim 0°$, except when the path length difference is an integer multiple (m) of the wavelength λ

$$L = m\lambda. \tag{2.117}$$

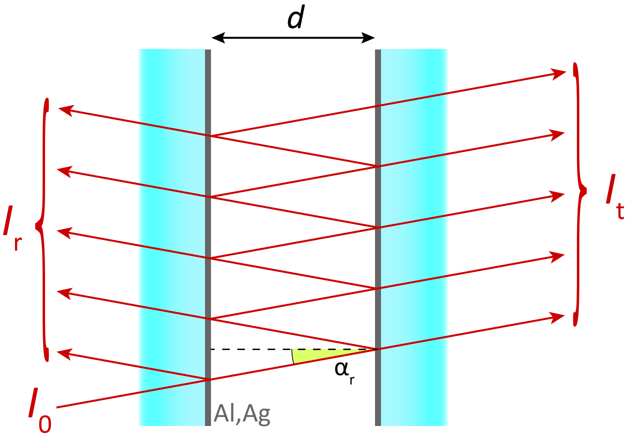

Figure 2.9: Scheme of the beam path entering a Fabry Pérot etalon at an incident angle α_r. The transmitted and reflected intensity is denoted as I_t an I_r, respectively. A thin film metal is coated on the inside surface to increase reflectivity.

At normal incidence ($\cos \alpha_r = 1$) the refractive index has no effect and the transmission condition becomes

$$\lambda = \frac{2d}{m}, \tag{2.118}$$

i.e., the observed wavelength is varied by scanning the mirror distance d. With the phase difference between two adjacent rays $\delta = k_0 L$ and the reflectivity r one obtains expressions for the relative intensity of the reflected and transmitted beam, respectively

$$\frac{I_r}{I_0} = \frac{(4F^2/\pi^2)\sin^2(\delta/2)}{1 + (4F^2/\pi^2)\sin^2(\delta/2)}, \tag{2.119}$$

$$\frac{I_t}{I_0} = \frac{1}{1 + (4F^2/\pi^2)\sin^2(\delta/2)}. \tag{2.120}$$

Here, the finesse F is directly related to the reflectivity of the mirrors[156]

$$F = \frac{\pi\sqrt{r}}{1 - r}, \tag{2.121}$$

and the term $1/[1 + (4F^2/\pi^2)\sin^2(\delta/2)]$ is the so called *Airy* function. With the parameter F, this function can be used to represent the transmission characteristics of a Fabry-Perot etalon. The portion of transmitted light as function of the phase difference is illustrated in Fig. 2.10. Large values for F (i.e., high reflectivity) result

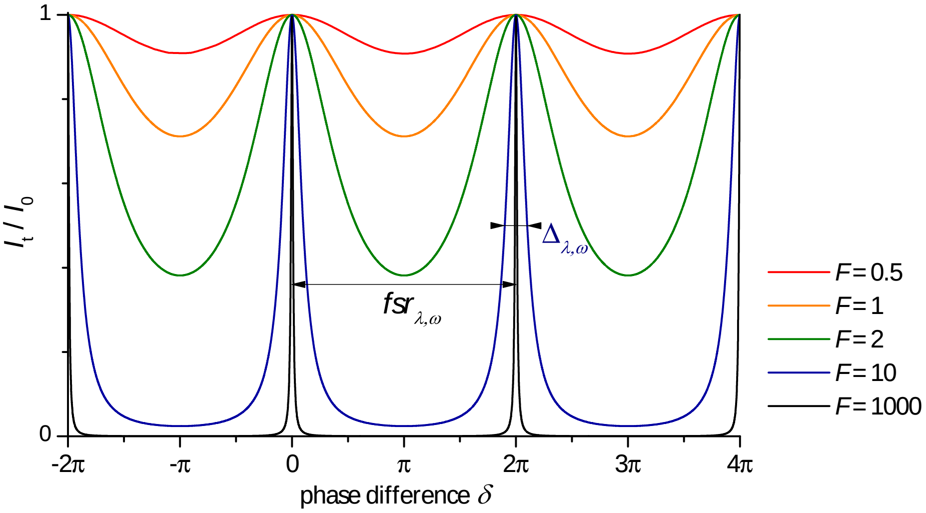

Figure 2.10: Illustration of the Airy transmission function of a FPI used in Eq. 2.119 at different values of F. The abscissa can be defined either in the wavelength or in the frequency domain.

in an almost complete extinction of the light entering the etalon and the intensity between the two transmission maxima approaches zero. The spectrometer's transmission function is characterized by the distance of the maxima, sometimes referred to as the free spectral range (fsr_λ), and the full width at half maximum $\Delta\lambda$. The finesse F serves as the figure of merit that can be easily evaluated from experimental observables (Fig. 2.10)

$$F = \frac{fsr_\lambda}{\Delta\lambda}. \tag{2.122}$$

Since our argumentation is based on path length differences we have defined fsr and Δ in the wavelength domain. However, the findings can be equally well presented in the frequency domain which is more important in practice

$$fsr_\lambda = \frac{\lambda^2}{2nd} \quad \longrightarrow \quad fsr_\omega = \frac{c}{2nd}, \tag{2.123}$$

$$\Delta\lambda \quad \longrightarrow \quad \Delta\omega, \tag{2.124}$$

whereas c denotes the vacuum velocity of light and (2.122) holds accordingly. Note that in this simple presentation no absorption effects are considered.

While in general a high finesse is preferred for high resolution measurements, one faces inherent problems of the technique. In practice it is hard to achieve

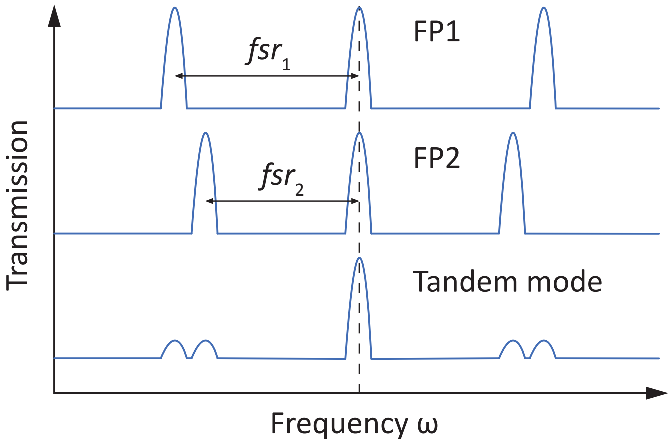

Figure 2.11: Tandem multi-pass operation of two FPI allows the suppression of higher order transmission modes. The two FPI have different *fsr*'s, hence only common multiples of fsr_1 and fsr_2 will be transmitted without attenuation.

$F > 50$, although non-scanning FPIs with special geometries and up to $F \sim 1000$ have been realized.[157] To vary the passing wavelength, one either has to adjust the refractive index inside the etalon (by different gases and/or concentration) or the mirror distance needs to be scanned. While the former is very slow, the latter is quite unstable and impractical to use. The group around Sandercock succeeded to develop a self-stabilizing scanning multiple-pass tandem FPI to tackle the above mentioned problems.[158]

The core element of the BLS setup (Fig. 2.12) is the interferometer (*JRS Scientific Instruments*) with two FPI's (FP1 and FP2) operated in tandem mode. That means the mirror distance is synchronously scanned by a common translation stage which is moving along the normal axis of FP1. Simultaneous transmission through both FPIs with different spacing $d_2/d_1 \sim 0.95$ requires

$$m_1\lambda = 2nd_1, \tag{2.125}$$

$$m_2\lambda = 2nd_2. \tag{2.126}$$

FP2 is inclined at a fixed angle φ with respect to FP1, therefore its mirror distance depends on those of the latter by

$$d_2 = d_1 \cos\varphi. \tag{2.127}$$

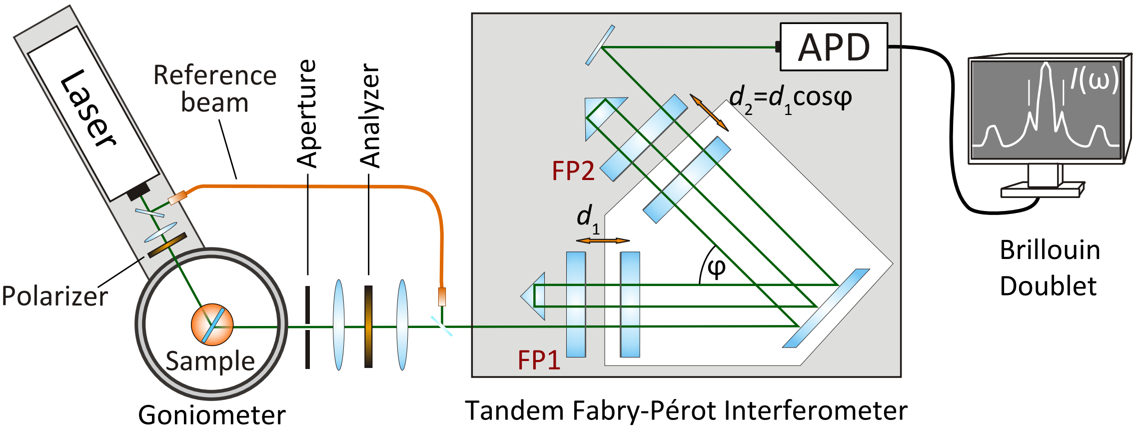

Figure 2.12: Scheme of the BLS setup. A polarized single-mode (532 nm) laser beam impinges on the sample centered in a goniometer which allows to change the scattering angle θ. The (inelastically) scattered light is analyzed by a 6-pass tandem FPI and the frequency shift upon interaction with a thermal phonon is observed as the Brillouin doublet. Both etalons are scanned synchronously by the translation stage (white) moving along the normal of FP1.

Figure 2.11 illustrates the transmission of a tandem FPI that realizes a much higher finesse and suppresses the higher order peaks (also referred to as "Ghosts"). Due to the different spacings (hence, different *fsr* values), one FPI blocks the transmitted light of the other, except under the condition where both transmission peaks fall together ($m_1/d_1 = m_2/d_2$), which is tuned to the center position (Fig. 2.11).

The light scattering setup as a whole is shown in Fig. 2.12. The sample holder is mounted in the middle of a goniometer with the option to control its temperature (-15–200 °C) and the possibility to apply strain by appropriate auxiliary devices. A solid-state diode-pumped single-mode laser ($\lambda = 532\,\text{nm}$, *Coherent, Compass 315M*, 150 mW) is placed on the goniometer arm. This configuration allows to measure at scattering angles θ between 5 and 150°, and probe sound propagation at various directions and magnitude of $\mathbf{q}$ inside the specimen. This is a clear advantage over BLS experiments using only the backscattering component q_{BS}. The laser beam passes a Glan-Thompson polarizer (extinction ratio of the depolarized light $\sim 10^{-5}$) ensuring vertical (V) polarization and is then focused to the center of the goniometer (beam diameter $\sim 100\,\mu\text{m}$). The scattered light along a specific direction is collected beyond an aperture, the subsequent pass of another Glan-Thompson prism (now with a higher extinction ratio of 10^{-8}) selects polarized (V) or depolarized (H) light,

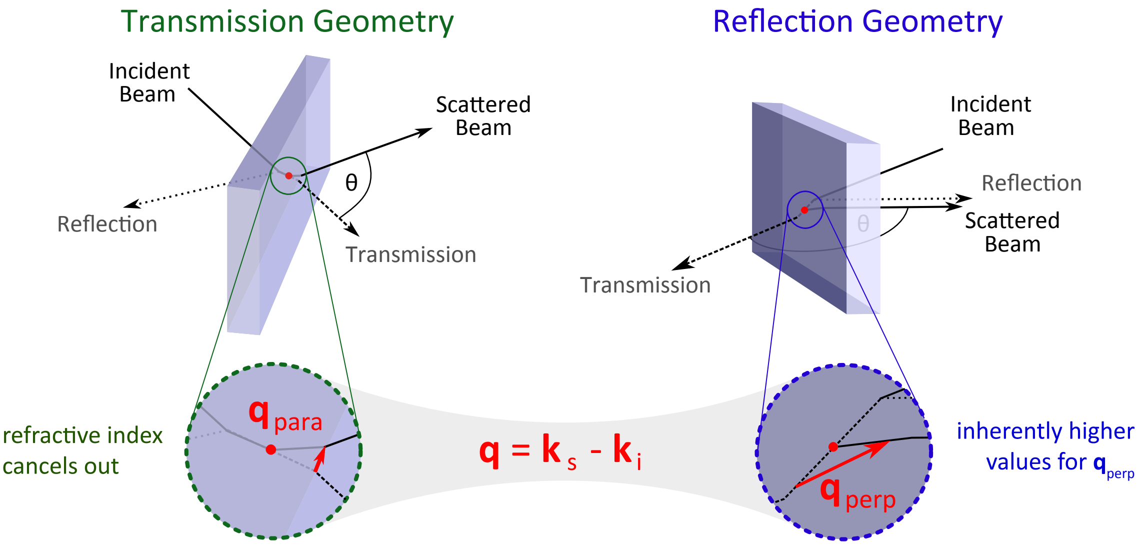

Figure 2.13: Scheme of the BLS scattering geometries for a slab sample. The left panel illustrates the transmission geometry in the special case of $\alpha = \theta/2$ for which n-independet moduli can measured. The right panel demonstrates the reflection geometry for $\alpha = \frac{180° - \theta}{2}$.

and the beam is focused into the entrance pinhole (150–1000 µm) of the tandem FPI. Inside the spectrometer, the scattered photons are directed by a set of lenses and mirrors to traverse a FPI etalon six times before they pass the output pinhole (200–1500 µm) and reach the detector. The latter is an avalanche photo diode (APD), whose signal is processed by a multi-channel analyzer (MCA, 1024 ch.) to give the frequency resolution as function of the position of the translation stage.

As mentioned above, the stability of the optical setup remains an issue for scanning FPIs. This problem is addressed by dynamic realignment of FP1 and FP2 for perfect parallelism of the two mirrors. Therefore, a small portion (∼4%) bypasses the sample and is used as reference to constantly adjust the piezo voltages that control the mirror position to gain maximum transmittance of the central elastic line. Each time the translation stage moves through the zero-frequency position, the dual-shutter unit behind the entrance pinhole selects the reference beam for stabilization purposes and to protect the detector from the high intensity of the Rayleigh line. At last, the whole setup rests on an optical table that provides active vibration isolation of disruptive noise from the environment.

The q-vector is—besides by the scattering angle—largely determined by the samples' geometry. In the case of a cylindrical sample, the scattering vector is given by

$$q = \frac{4\pi n}{\lambda} \sin \frac{\theta}{2}. \tag{2.128}$$

However in this work we often deal with samples of slab geometry which are easy to prepare and can be conveniently positioned in the center of the goniometer with a selected angle of incidence α. In general, two scattering geometries are used and sketched in Fig. 2.13. In transmission, the magnitude of the q-vector is defined by

$$q = \frac{4\pi n}{\lambda} \sin \left[\frac{1}{2} \arcsin \left(\frac{\sin(\theta - \alpha)}{n} \right) + \frac{1}{2} \arcsin \left(\frac{\sin \alpha}{n} \right) \right]. \tag{2.129}$$

When the q-vector is decomposed into its components parallel and perpendicular to the slab plane, the component $q_{\|}$ is independent of the material's refractive index n

$$q_{\|} = \frac{2\pi}{\lambda} \left[\sin \alpha + \sin(\theta - \alpha) \right]. \tag{2.130}$$

Sound propagation parallel to the sample is probed in the special case of $\mathbf{q} = \mathbf{q_{para}}$, i.e. $\theta = 2\alpha$, where q is simply given by

$$q = q_{para} = \frac{4\pi}{\lambda} \sin \frac{\theta}{2}. \tag{2.131}$$

This geometry allows the unequivocal determination of the sound velocities in unknown materials without having to rely on the (estimated) refractive index. Furthermore, the refractive index of new mechanically homogenous materials can be evaluated by measuring the (linear) dispersion in transmission and reflection geometry. The $q_{\perp}$ values can be fitted in n until they line up with the group velocity (the slope of the dispersion) measured independent of n. For the reflection geometry, the scattering vector reads

$$q = \frac{4\pi n}{\lambda} \sin \left[\frac{1}{2} \arcsin \left(\frac{\sin \alpha}{n} \right) + \frac{1}{2} \arcsin \left(\frac{\sin(\theta + \alpha)}{n} \right) \right], \tag{2.132}$$

and under the condition $\alpha = \frac{180^\circ - \theta}{2}$ the probed wavevector is equal to the perpendicular component $\mathbf{q} = \mathbf{q}_{\perp}$.

Part II.

One-Dimensional Phononics

3. Engineering the Band Diagram of Hypersonic Hybrid Superlattices

This Chapter reports on the full control of phononic band diagrams for periodic stacks of alternating layers of poly(methyl methacrylate) and porous silica combining Brillouin light scattering spectroscopy and theoretical calculations. These structures exhibit large and robust on-axis band gaps determined by the longitudinal sound velocities, densities, and spacing ratio. A facile tuning of the gap width is realized at oblique incidence utilizing the vector nature of the elastic wave propagation. Off-axis propagation involves sagittal waves in the individual layers, allowing access to shear moduli at nanoscale. The full theoretical description discerns the most important features of the hypersonic one-dimensional crystals forward to a detailed understanding, a precondition to engineer dispersion relations in such structures.

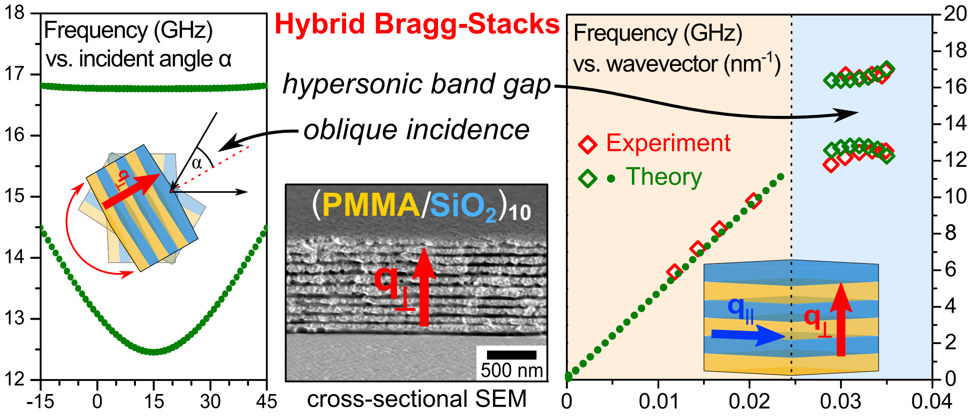

This Chapter is based on:

D. Schneider, F. Liaqat, E. H. El Boudouti, Y. El Hassouani, B. Djafari-Rouhani, W. Tremel, H.-J. Butt, G. Fytas, *Engineering the Hypersonic Phononic Band Gap of Hybrid Bragg Stacks.* Nano Lett. 2012, **12**, 3101.

3.1. Introduction

Controlling sound propagation has been an intensely studied field during the past centuries, ranging from architectural design[88] over noise reduction applications[159,160] to the rise of thermal management,[81] sound shields,[161] acoustic diodes,[113] and acoustic metamaterials.[49,162] Phononic crystals (PnC) happen to be a promising class of composite structures, that allow for systematic manipulation of elastic (acoustic) wave propagation. The most striking feature is their ability to create (phononic) band gaps, similar to the electronic and photonic bandgaps in semiconductors and photonic crystals (PhC), respectively. Following the discoveries in the older field of PhC (periodic spatial variation of refractive index n), PnCs (variation of density ρ, longitudinal c_L and transverse c_T sound velocities) happen to share many similarities, such as Bragg reflection and characteristic dispersion relations. However, elastic waves require many more parameters being considered for a full theoretic description, *i.e.*, it renders predicted phononic behavior complicated. While the band diagram of semiconductors simply reflects scalar waves, and transverse waves in PhCs, sufficient description of sound propagation requires full vector waves.

The search for phononic structures started with theoretical work,[32,33] in 1993. The first observation of band gaps followed later, using manually manufactured metallic macrostructures in the centimeter range with gaps at audible frequencies.[34] In contrast to these sonic phononic crystals, the need to reach high frequencies in the hypersonic (GHz) range and beyond imposes substantial demand on design, fabrication, and characterization techniques because of the inherently much smaller length scale. The first phononic band gap in the hypersonic regime was experimentally observed in a three-dimensional assembly of close-packed polymer colloids,[40] soon after its prediction in 2005.[39] During the following years extensive research has been carried out on hypersonic phononics. The tuning and switching of high frequency phononics[40,163] point forward to possible applications and underline the importance of controlled wave propagation. However, the full description of phonon propagation in multidimensional periodic assemblies still remains a challenging task.

The research on phononic band diagrams in 1D superlattices has started earlier than the discovery of complete (omnidirectional) phononic band gaps[32,33] with the study of folded phonons in a semiconductor superlattice using Raman spectroscopy at few laser wavelengths,[91] followed by other Raman studies.[92–94,106] More recently, some evidence for the existence of a hypersonic band gap and zone-folded phonons, and in-plane layer excitations was reported for porous silicon[98,99] and polymer[95,100,101] superlattices using Brillouin and pump-probe time resolved spectroscopy. For 1D periodic structures, however, the first direct observation of a sizeable normal incidence hypersonic phononic band gap was reported in periodic porous silica/poly(methyl methacrylate) (p-SiO_2/PMMA) multilayer films by some of the present authors.[95]

The latter study has initiated new perspectives towards engineering of phonon propagation which are addressed in this work. These include (i) robustness of the dispersion to fabrication inherent imperfections, (ii) the unique estimation of both elastic moduli (longitudinal C_{11} and shear C_{44}) and elasto-optic coefficients of the individual layers through (iii) the theoretical representation of the dispersion relations for normal and oblique incidence and (iv) the intensities of the two, lower and upper, phononic branches of the gap. On the basis of these findings, we expect new designs of nanostructures to emerge for desired direction dependent elastic wave propagation and profound (hypersonic) phonon-(visible) photon interactions.

3.2. Experimental

3.2.1. Fabrication

Stacks of poly(methyl methacrylate) (PMMA) and porous silica (p-SiO_2) were assembled by alternating spin-coating from the respective stock solutions on a glass substrate starting with the PMMA layer. Two multilayer stacks each consisting of twenty alternating PMMA and p-SiO_2 layers with different thicknesses d_{PMMA} and $d_{\mathrm{SiO_2}}$ and hence periodicity a ($= d_{\mathrm{PMMA}} + d_{\mathrm{SiO_2}}$) were fabricated. A combination of scanning electron microscopy (SEM) and confocal microscopy was used to determine (i) the relative distribution of materials and (ii) the absolute thickness of the multilayer structure. Figure 3.1 (left panel) displays the SEM pictures of stack A with $a = 117\,\mathrm{nm}$ ($d_{\mathrm{SiO_2}} = 79\pm6\,\mathrm{nm}$ and $d_{\mathrm{PMMA}} = 38\pm4\,\mathrm{nm}$) and stack B with $a = 100\,\mathrm{nm}$ ($d_{\mathrm{SiO_2}} = 55\pm5\,\mathrm{nm}$ and $d_{\mathrm{PMMA}} = 45\pm5\,\mathrm{nm}$).

3.2.2. Brillouin light scattering

We used the non-destructive technique of spontaneous Brillouin light scattering (BLS) spectroscopy to probe hypersonic phonons propagating in these structures at sub-micrometer scale and thermal equilibrium (Section 2.4). BLS utilizes the photo-elastic interaction of an incident visible photon (532 nm) and a thermally excited phonon with wavevector k and frequency ω $(= 2\pi f)$ in the sample. The phonon energy is represented by the frequency shift (ω) of inelastically scattered light of a single-mode laser beam. The small shift (of the order of few GHz) is resolved by a six-pass tandem Fabry-Pérot interferometer. For a homogeneous medium, the probed phonon has k equal to the scattering wavevector $\mathbf{q} = \mathbf{k}_\mathrm{s} - \mathbf{k}_\mathrm{i}$ (here $\mathbf{k}_\mathrm{s}$, $\mathbf{k}_\mathrm{i}$ are the wavevectors of the scattered light and incident laser beam). For a periodic structure with a reciprocal lattice vector $\mathbf{G}$ momentum conservation requires, $\mathbf{k} = \mathbf{q} + \mathbf{G}$. The desired dispersion relation is represented by the plot $\omega(k)$ along a propagation direction selected by the scattering geometry:[95] Along the periodicity direction (on-axis), $q = q_\perp$ is perpendicular to the layers (hence, $q_{\|} = 0$), whereas in-plane propagation is probed for $q = q_{\|}$ along the layers (and hence $q_\perp = 0$); at oblique incidence, $q_\perp, q_{\|} \neq 0$ (off-axis).

3.3. Results and Discussion

3.3.1. Normal incidence phonon propagation

Figure 3.1 displays BLS spectra for stacks A and B, both for two $q_\perp$-values near the edge of the first Brillouin zone (BZ) appearing at $G/2 = \pi/a$, *i.e.* $q_\mathrm{BZ} = 0.0269\,\mathrm{nm}^{-1}$ and $q_\mathrm{BZ} = 0.0314\,\mathrm{nm}^{-1}$, respectively for stacks A and B. The double peak structure of the BLS spectra correspond to the bands 1 (at low) and 2 (at high frequency) between which the Bragg gap occurs. The different spacing of the two films is manifested in the BLS spectral shape (Fig. 3.1); stack A (periodicity $a = 117\,\mathrm{nm}$) shows only branch 2 while stack B ($a = 100\,\mathrm{nm}$) displays both branches at the high $q_\perp$ value in the right panel of Fig. 3.1. The BLS spectra correspond to different $q_\perp a$ values and their shape sensitively depends on the proximity to the edge of the BZ at $q_\perp a = \pi$.

Both stacks were scanned through the accessible q-range (methods) to obtain

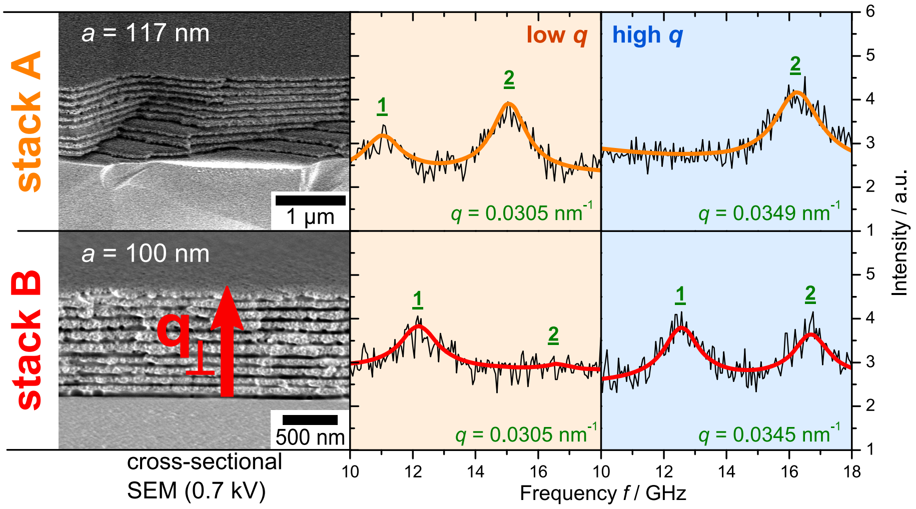

Figure 3.1: Two Bragg-stacks and the phononic band gap at a glance; scanning electron microscopy (SEM) images (left) and splitting into two phonon branches (1 and 2, middle and right panel). Stack A has a larger spacing a than stack B and displays only the high-frequency band 2 at high $q_\perp$ directed normal to the layers (on z-axis, s. scheme in the left panel). The situation is inverted in stack B. The solid lines represent Lorentzian line fits used to extract the frequency f and damping Γ (FWHM) of modes (1) and (2) from the experimental spectra.

the dispersion relation $f(q_\perp)$ for on-axis phonon propagation (yellow circles/red diamonds on blue ground in Fig. 3.2c). The BLS spectra were well represented by a double Lorentzian convoluted with the instrumental function (Fig. 3.1); the solid lines in Fig. 3.2a represent the theoretical spectra. The line intensities and the peak frequencies are shown in Figs. 3.2b and 3.2c (blue shaded area), respectively. Figure 3.2c also includes the phonon frequencies for in-plane propagation (reddish area) in the two hybrid stacks. The opening of a hypersonic phononic stop band along the periodicity direction (at $q_\perp a = \pi$) is demonstrated with the two stacks covering different regimes in the BZ; stack A falls mainly into the 2$^{\text{nd}}$ BZ. In spite of the (small) differences in the elastic parameters (Table 3.1), the intensity ratio $I(2)/I(1)$ of the two bands superimpose on a common curve when plotted versus $q_\perp a$ in Fig. 3.2b, thereby justifying the larger ratio observed for stack A (Figs. 3.1 and 3.2a).

A detailed understanding of the phononic properties of 1D crystals requires the full description of the experimental BLS spectrum that involves the concurrent representation of both intensities of the two modes and the dispersion relations. Following

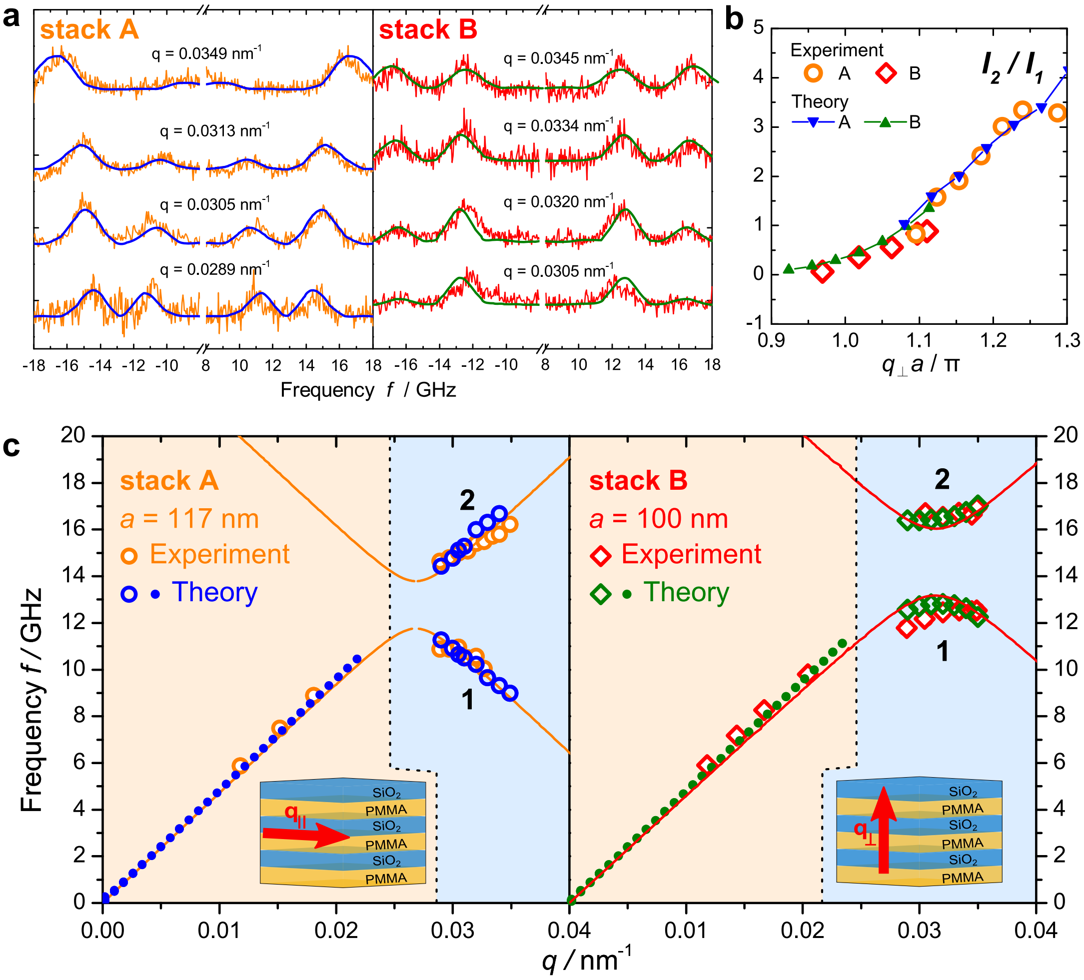

Figure 3.2: a) Experimental BLS-spectra of the stack A and B superimposed with the theoretical spectra (solid lines) at different phonon wavevectors $q_\perp$ normal to the layers. b) The ratio $I(2)/I(1)$ of the intensities of the high and low frequency bands in (a). The small-size symbols indicate the values of $I(2)/I(1)$ obtained from the theoretical spectra in (a). c) Dispersion relation of stack A and B (experimental data given in yellow circles/red diamonds) for in-plane (reddish back) and out-of-plane (light blue back) propagation. The solid lines denote the theoretical dispersion relation Eq. 3.2 for sound propagation along the periodicity axis (scheme for $q_\perp$) and hollow symbols indicate the mode 1 and 2 frequencies obtained from the theoretical spectra in a). The linear dispersion for phonon propagation parallel to the stacks (scheme for $q_{||}$) is denoted as a dotted line along with the experimental data along the same direction.

the strategy outlined in Sections 2.2.4 and 2.3.3 the scattered intensity is given by (2.103)

$$I_s(\omega, q_\perp) \propto \left| \sum_\alpha \int p_\alpha e^{\mathrm{i}q_\perp z'} \frac{\partial u_\alpha(z', \omega)}{\partial z'} \mathrm{d}z' \right|^2 . \tag{3.1}$$

The solid lines in Fig. 3.2a denote the fit of $I_s(\omega, q_\perp) \propto |E_s(\omega, q_\perp)|^2$ to the BLS spectra using the values of the parameters listed in Table 3.1. The computed $I(\mathtt{2})/I(\mathtt{1})$ ratio (solid symbols in Fig. 3.2b) and the frequencies of modes `1` and `2` (blue and green symbols on the right shaded areas in Fig. 3.2c) in the dispersion relations of the two stacks are in good agreement with the corresponding experimental values. The on-axis dispersion diagram in the present 1D phononic crystals was found to be well represented (solid lines in Fig. 3.2c) by[86]

$$\begin{aligned} \cos(ka) = & \cos\left(\frac{\omega\, d_{\mathrm{SiO_2}}}{c_{\mathrm{L,SiO_2}}}\right) \cos\left(\frac{\omega\, d_{\mathrm{PMMA}}}{c_{\mathrm{L,PMMA}}}\right) \\ & - \frac{1}{2}\left(\frac{Z_{\mathrm{SiO_2}}}{Z_{\mathrm{PMMA}}} + \frac{Z_{\mathrm{PMMA}}}{Z_{\mathrm{SiO_2}}}\right) \sin\left(\frac{\omega\, d_{\mathrm{SiO_2}}}{c_{\mathrm{L,SiO_2}}}\right) \sin\left(\frac{\omega\, d_{\mathrm{PMMA}}}{c_{\mathrm{L,PMMA}}}\right), \end{aligned} \tag{3.2}$$

with $Z(= \rho\, c_L)$ being the longitudinal elastic impedance of the two layers. In the computation of the dispersion relations, we utilized the values of the parameters (Table 3.1) as obtained from the representation of the experimental spectra (Fig. 3.2). Hence, the description of the dispersion relations in Fig. 3.2c by (3.2) is noticeable.

The effective medium longitudinal sound velocity $c_{\mathrm{L},\perp}$ amounts to 2970 ms^{-1} in stack A and 2890 ms^{-1} in stack B (slope of (3.2) in the low-q limit). In fact, these values can be also computed from Wood's law,[164] which is obtained by Taylor expansion of (3.2) around $\omega = 0$:

$$\frac{1}{M(A/B)} = \frac{\phi}{\rho_{\mathrm{PMMA}} c^2_{\mathrm{L,PMMA}}} + \frac{1-\phi}{\rho_{\mathrm{SiO_2}} c^2_{\mathrm{L,SiO_2}}}, \tag{3.3}$$

whereas M $(= C_{11} = \rho_{\mathrm{eff}}\, c^2_{\mathrm{L},\perp})$ is the bulk modulus of the whole system (stack A or B) with an effective density of $\rho_{\mathrm{eff}} = \phi\rho_{\mathrm{PMMA}} + (1-\phi)\rho_{\mathrm{SiO_2}}$, and volume fraction $\phi = d_{\mathrm{PMMA}}/a$.

The frequency of band `1` below the gap (reddish area in Fig. 3.2c) deviates from

Table 3.1: Values of the physical quantities used in the calculations.

		PMMA	p-SiO$_2$	substrate
A	c_L / m s^{-1}	2800^a	3100	5600
	c_T / m s^{-1}	1400^a	1800	
	ρ / kg m^{-3}	1190^a	1420	2200
	d / nm	38	79	
	$p_{\text{PMMA}}/p_{\text{SiO}_2}$	2		
	n	1.49	1.46	1.53
B	c_L / m s^{-1}	2800^a	3030	5600
	c_T / m s^{-1}	1400^a	1800	
	ρ / kg m^{-3}	1190^a	1500	2200
	d / nm	45	55	
	$p_{\text{PMMA}}/p_{\text{SiO}_2}$	2		
	n	1.49	1.46	1.53

Sound velocities (c_L, c_T), density (ρ), thickness (d), refractive index (n).
^{a} These parameters were fixed to the values of bulk PMMA film.[73,95]

the corresponding frequency (experimental symbols) for in-plane propagation in both stacks. In the direction parallel to the layers, the effective medium sound velocity $c_{\text{L},\|}$ is a different average of the elastic properties in the individual layers as it is affected by sagittal modes. In fact, the computed in-plane acoustic phonon frequency[165] (dots in the reddish area of Fig. 3.2c) agrees well with the experimental frequencies along the same direction. The slopes of these dotted lines, *i.e.*, the sound velocities for in-plane propagation $c_{\text{L},\|}(A) = 3020\,\text{m/s}$ and $c_{\text{L},\|}(B) = 2990\,\text{m/s}$ are slightly higher than the corresponding $c_{\text{L},\perp}$, respectively. This small difference might suggest a low ($< 5\%$) mechanical anisotropy normal, and parallel to the layers.

In order to provide a measure for the width of the band gap, we first look at two exemplary situations. If we assume that $\frac{d_{\text{PMMA}}}{c_{\text{L,PMMA}}} = 2\frac{d_{\text{SiO}_2}}{c_{\text{L,SiO}_2}}$, exemplified by stack A, the frequencies of the upper/lower limit of the gap are given exactly by,

$$f_{1,2} = \frac{c_{\text{L,PMMA}}}{2\pi d_{\text{PMMA}}} \cos^{-1}\left(\frac{Z_{\text{PMMA,SiO}_2}}{Z_{\text{PMMA}} + Z_{\text{SiO}_2}}\right). \tag{3.4}$$

The obtained gap width of $\Delta f = f_2 - f_1 \sim 2\,\text{GHz}$, is in good agreement with the band gap in stack A. Now, if we assume $\frac{d_{\text{PMMA}}}{c_{\text{L,PMMA}}} = \frac{d_{\text{SiO}_2}}{c_{\text{L,SiO}_2}}$, approximately fulfilled in stack B, the center of the first gap conforms to $\frac{f_0\, d_{\text{PMMA}}}{c_{\text{L,PMMA}}} = \frac{f_0\, d_{\text{SiO}_2}}{c_{\text{L,SiO}_2}} = 1/4$, *i.e.*, the system acts as an “quarter wave stack” exhibiting the widest possible band gap in 1D crystals,[22]

$$f_{1,2} = f_0 \pm \frac{2f_0}{\pi} \sin^{-1}\left(\frac{Z_{\mathrm{PMMA}} - Z_{\mathrm{SiO_2}}}{Z_{\mathrm{PMMA}} + Z_{\mathrm{SiO_2}}}\right), \tag{3.5}$$

with f_0 being the frequency of the center of the gap at $k_{\mathrm{BZ}} = \pi/a$. The larger gap width in stack B is $\Delta f \sim 3\,\mathrm{GHz}$ according to (3.5) and in good agreement with the experimentally observed band gap.

Aside of these two special cases and for relatively small contrast in elastic impedance $\Delta Z/\overline{Z}$ (which is the case here) the width of the band gap can be approximated by a general expression,[166]

$$\Delta f \cong 4f_0 \sin \frac{\pi d_{\mathrm{PMMA}} c_{\mathrm{L,SiO_2}}}{d_{\mathrm{PMMA}} c_{\mathrm{L,SiO_2}} + d_{\mathrm{SiO_2}} c_{\mathrm{L,PMMA}}} \frac{\Delta Z}{\overline{Z}}, \tag{3.6}$$

where $\Delta Z = |Z_{\mathrm{PMMA}} - Z_{\mathrm{SiO_2}}|$, $\overline{Z} = \sqrt{Z_{\mathrm{PMMA}} Z_{\mathrm{SiO_2}}}$ and f_0 is obtained from $\frac{1}{2f_0} = \frac{d_{\mathrm{PMMA}}}{c_{\mathrm{L,PMMA}}} + \frac{d_{\mathrm{SiO_2}}}{c_{\mathrm{L,SiO_2}}}$. Note that f_0 defines the middle of the gap only in the case of a “quarter wave stack”, where the gap width is maximized. The fundamental quantity of 1D phononic crystals, the width of their primary band gap, depends on many parameters, such as thickness and sound velocity of constituent materials and not just from the impedance mismatch $\Delta Z/\overline{Z}$, although this plays a central role (Fig. 3.5); $\Delta Z/\overline{Z} \sim 0.37$ for the present PMMA and p-SiO_2 layers.

For small elastic contrast, Eqs. 3.4–3.6 yield two simple equations for stop band width of stacks A ($d_{\mathrm{PMMA}}/d_{\mathrm{SiO_2}} \approx 0.5$) and B ($d_{\mathrm{PMMA}}/d_{\mathrm{SiO_2}} \approx 1$), respectively:

$$\Delta f \cong \frac{\sqrt{3}}{6} \frac{c_{\mathrm{L,PMMA}}}{\pi d_{\mathrm{PMMA}}} \frac{\Delta Z}{\overline{Z}} \approx 1.8GHz, \tag{3.7}$$

and

$$\Delta f \cong \frac{1}{2} \frac{c_{\mathrm{L,PMMA}}}{\pi d_{\mathrm{PMMA}}} \frac{\Delta Z}{\overline{Z}} \approx 3GHz. \tag{3.8}$$

The observed good agreement between theory and experiment leads to important conclusions: (i) the phononic dispersion is not simply scalable with the contrast of elastic impedance $\Delta Z/\overline{Z}$. In contrast to photonics, density and sound velocity of both layers enter explicitly in (3.2); (ii) the physical quantities, density and longitudinal elastic modulus of the porous $\mathrm{SiO_2}$ layer adopt lower values than in silica glass; these are slightly different in the two stacks; (iii) the average thicknesses of the individual layers are uniquely obtained, and (iv) effective medium elastic parameters (ρ,$c_{\mathrm{L},\perp}$) are also obtained from the frequency of mode `1` which becomes acoustic only at low $q_\perp$'s.

3.3.2. Oblique incidence phonon propagation

A versatile tuning of the phononic band structure is feasible by simply turning the film around its axis normal to the scattering plane (saggital plane) as visualized in Fig. 3.3a. This leads to an oblique incidence at which the scattering wavevector q deviates from $q_\perp$ activating mixing with saggital modes, *i.e.*, in-plane propagating transverse modes. Yet, q is represented by a linear combination of $q_\perp$ and $q_\|$, that is a function of the scattering angle θ and the incident angle α (Eq. 3.9)

$$q_\| = q \cdot \sin\left[\frac{1}{2}\left(\sin^{-1}\left(\frac{1}{n}\sin\alpha\right) - \sin^{-1}\left(\frac{1}{n}\sin\left(\alpha+\theta\right)\right)\right)\right], \tag{3.9a}$$

$$q_\perp = q \cdot \cos\left[\frac{1}{2}\left(\sin^{-1}\left(\frac{1}{n}\sin\alpha\right) - \sin^{-1}\left(\frac{1}{n}\sin\left(\alpha+\theta\right)\right)\right)\right], \tag{3.9b}$$

$$q = \sqrt{q_\|^2 + q_\perp^2}. \tag{3.9c}$$

Figure 3.3b depicts the phonon frequencies of modes `1` and `2` as function of the incidence angle in stack B (at $\theta = 150°$). As α deviates from $\frac{\pi-\theta}{2}$ ($= 15\,°$) the low-frequency mode `1` approaches the high-frequency mode 2, which is remarkably robust to the incidence angle. We note that the experimental frequencies (dots in Fig. 3.3b) do not fall at the edge of the BZ. The locus of the two mode frequencies in the three-dimensional dispersion diagram is better seen in Fig. 3.3c along with the theoretical dispersion relations (dotted lines) plotted as a function of both, $q_\perp$ and $q_\|$. Furthermore, the gap width narrows with increasing $q_\|$ or obliqueness. The mixing of the longitudinal with the transverse phonons becomes advantageous since it allows the estimation of the shear moduli of the individual layers.

The computed frequencies of modes `1` and `2` using the shear velocity $c_{\mathrm{T,SiO_2}}$ (Table 3.1) as adjustable parameter capture the experiment very well (Figs. 3.3b and 3.3c). Thus, implementation of particular sample rotation (Fig. 3.3) is beneficial as

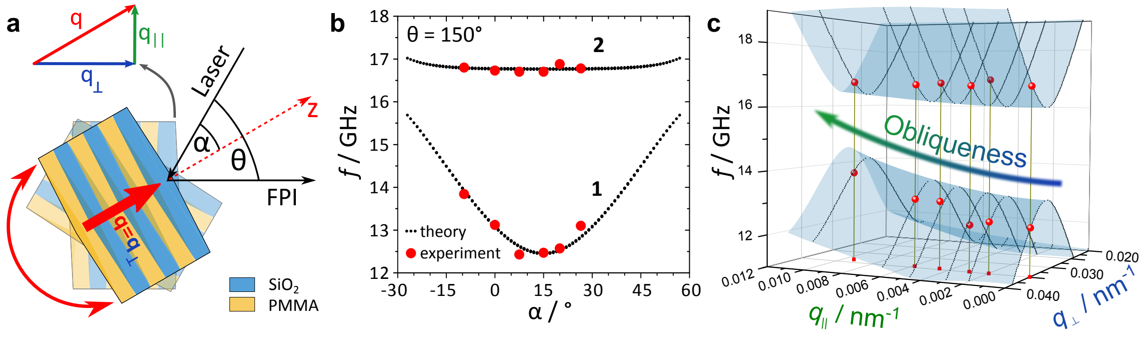

Figure 3.3: Oblique phonon propagation and impact on the dispersion relation. a) Scheme of experimental geometry. Laser and detector remain at fixed positions while the stack itself is turned around the normal of the scattering plane; α varies at constant $\theta (= 150°)$. b) Frequency for the low (1) and high (2) frequency Bragg modes in stack B as a function of the incident angle α. c) Theoretical dispersion relation $f(q_{\|}, q_{\perp})$ around the center of the longitudinal acoustic band is illustrated in a 3D surface. The experimental data obtained at various α are depicted in red (shaded if below the surface) and the theoretical dispersions $f(q_{\perp})$ at different $q_{\|}$ are presented by dotted lines.

it allows ease tuning of the gap and concurrent determination of the shear moduli which are inaccessible for normal incidence wave propagation.

3.3.3. Structure disorder and layer imperfections

Figure 3.4 contrasts the theoretical prediction of the modes near the edge of the BZ of an ideal 1D periodic structure with the experimental doublet of the BLS spectrum for stack A at a constant $q_{\perp}$. The left panel (Fig. 3.4a) shows the theoretical dispersion relation while panel 3.4b displays the calculated DOS with ten sharp peaks for each branch in the BZ equivalent to the number of periods in the stack. The peak separation is about 1.2 GHz in the DOS diagram, while their inherent broadening ($\Gamma^* \sim 0.25$ GHz, even smaller near the gap) is due to interaction of the superlattice discrete modes with the substrate continuum as these modes are propagating within the substrate. The modeled spectrum, displayed in Fig. 3.4c for $q_{\perp} = 0.0313\,\mathrm{nm}^{-1}$ (vertical dashed line in Fig. 3.4a), exhibits a triplet spectral structure (with the maximum at the fixed $q_{\perp}$). It had to be convoluted with the instrumental function (Gaussian with $\Gamma \sim 2\Gamma^* \sim 0.53$ GHz) to match the doublet shape of the experimental spectrum in Fig. 3.4d associated with the dispersion diagram of the infinite structure (Eq. 3.2 and Fig. 3.2c).

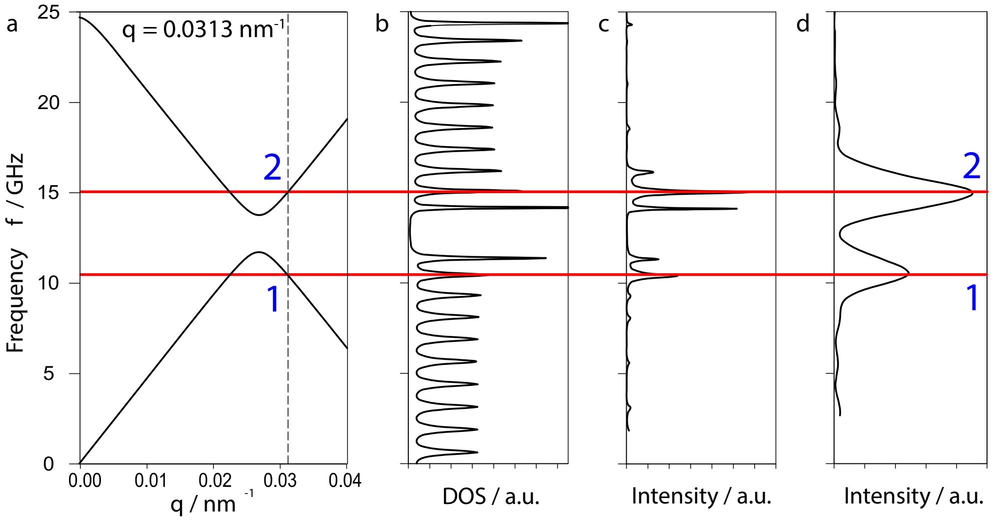

Figure 3.4: Dispersion curve at normal incidence (a), densities of states (DOS) (b) and two modeled spectra of different resolutions (c,d) at $q = 0.0313\,\mathrm{nm}^{-1}$ (vertical dashed line in a). The linewidth (FWHM) of the peaks in the DOS (b) is $\sim$0.25 GHz and the theoretical spectrum in (c) is a triplet spectral structure for each of the two Bragg bands 1 and 2 with maximum frequencies arising at f fixed by $q_\perp$ in the dispersion curve (a) (red guides). The triplet structure in (c) is smeared out to the experimental doublet (d) due to the reduced resolution ($\Gamma = 0.53\,\mathrm{GHz}$).

3.3.4. The role of structure incoherence

In order to elucidate the impact of unavoidable interfacial defects of layers (SEM pictures in Fig. 3.1), we note that state-of-the-art hybrid (inorganic/polymer) spin-coating cannot yet compete with semiconductor production techniques, *e.g.*, molecular beam epitaxy, in terms of roughness and structural coherence. However, the roughness is much smaller than the layer thicknesses and phonon wavelengths in the sub-micrometer range should render the scattering losses weak.

We therefore consider theoretically the effect of structural disorder exemplified by incoherent spacing. Figure 3.5a shows the experimental BLS spectrum of stack A at $q_\perp = 0.0313\,\mathrm{nm}^{-1}$ along with the computed spectrum indicated by the solid line as already shown in Fig. 3.4d. The sensitivity of this representative spectrum in the vicinity of the BZ to the variation of the thickness of the two constituent layers at fixed lattice constant a (=117 nm) is illustrated in Fig. 3.5b for three thickness combinations and the average spectrum over ten thousand realizations with different $d_{\mathrm{PMMA}}/d_{\mathrm{SiO_2}}$ ratios. It is remarkable that the spectral doublet is robust and only the lower frequency band 1 undergoes a blue shift leading to a gap narrowing with decreasing $d_{\mathrm{PMMA}}/d_{\mathrm{SiO}_2}$ whereas the large sampling (dashed line in Fig. 3.5) coincides with the spectrum for $d_{\mathrm{PMMA}}/d_{\mathrm{SiO}_2} = 0.5$ (∼39/78). The gap widening at increased volume fractions of PMMA, as well as the asymmetric shift of the low- and high-frequency peak are captured by Eqs. 3.4–3.6. This predicted trend is clearly seen in the non-convoluted spectra of Fig. 3.5c which indicates that the smearing of the triplet structure for both bands 1 and 2 (Fig. 3.5b) cannot be singly attributed to the particular kind of disorder (structure incoherence). We conclude that the smearing due to disorder is less than the experimental resolution, hence its effect can only be evaluated if the instrumental resolution could be significantly improved.

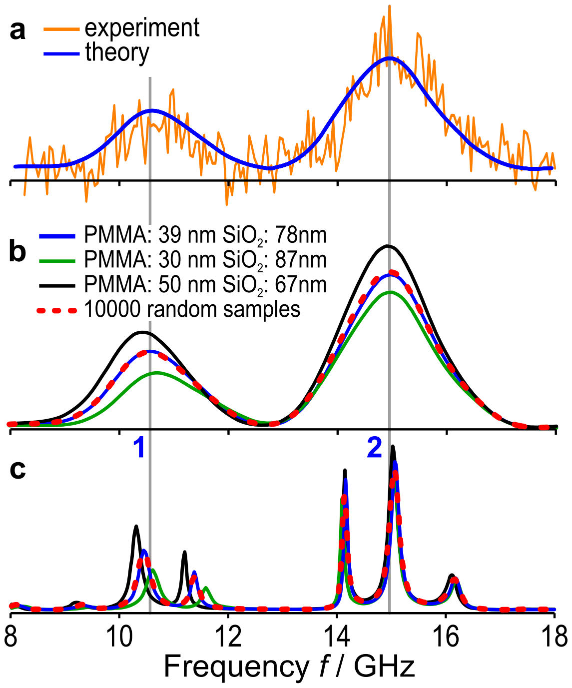

Figure 3.5: Structure incoherence. a) The experimental BLS of stack A at $q = 0.0313\,\mathrm{nm}^{-1}$ along with the (low resolution) theoretical spectrum (solid line) of Fig. 3.4d with $d_{\mathrm{PMMA}} = 38\,\mathrm{nm}$ and $d_{\mathrm{SiO}_2} = 79\,\mathrm{nm}$. b) Theoretical spectra at three different $d_{\mathrm{PMMA}}/d_{\mathrm{SiO}_2}$ ratios (solid lines), but fixed spacing $a = 117\,\mathrm{nm}$. The dashed curve represents a mean over 10 000 stacks of randomly chosen PMMA/p-SiO$_2$ fraction between the two extrema ($30\,\mathrm{nm} \leq d_{\mathrm{PMMA}} \leq 50\,\mathrm{nm}$). c) High resolution theoretical spectra without instrumental broadening corresponding to the four cases in (b) (cf. Fig. 3.4c).

3.4. Conclusions

One dimensional periodic hybrid phononic structures act as a model system for a fundamental understanding of elastic wave propagation in nanostructured matter. A phononic "Bragg" gap opens for wave propagation along the periodicity direction, *i.e.*, normal incidence. The width, the frequency at the center of the gap, and the intensities of the lower and upper frequency Bragg modes are all well described theoretically. The concurrent representation of the phonon dispersion and the amplitudes of the modes leads to the estimation of the out-of-plane longitudinal sound velocity and density of the individual layers. Inherent fabrication-related film imperfections such as inhomogeneous layer thicknesses lead to a smearing of the position of the lower Bragg mode. However, the width of the gap remains constant in the course of the examined thickness variations as indicated by the simulations.

Tuning of the gap position and width is readily obtained by rotation of the stack around the axis normal to the saggital plane of the film. At such oblique incidence due to the vector nature of the elastic wave propagation, mixing with in-plane saggital modes allows the estimation of the shear moduli of the individual layers at nanoscale. Access to both moduli opens a new way to investigate material behavior under confinement and address direction dependent mechanical properties.

The complete description of 1D hybrid phononics, *i.e.*, experimental dispersion relations and the density of states of one-dimensional hybrid stacks creates the fundamental knowledge necessary to engineer the band structure of high frequency phononics. Introduction of defect layers and design of dual gap structures for both, photons in the visible and hypersonic phonons look now more feasible.[167]

This work is the first demonstration of the utility of soft matter fabrication techniques in hypersonic phononics. As compared with classical semiconductor fabrication techniques leading to high quality periodic structures at shorter length scales,the present hybrid hypersonic structures possess distinct advantages, such as facile tuning of the elastic impedance contrast, realization of large phonon band gaps, and good perspectives for strong interactions of hypersonic phonons with visible photons. In addition, the reach of polymer and colloid science enables a wealth of soft periodic structures with ease tunability. Yet, their quality can be significantly improved using, *e.g.*, interference lithography fabrication techniques.[39,168]

4. Defect-controlled Hypersound Propagation in Hybrid Superlattices

This Chapter reports on spontaneous Brillouin light scattering spectroscopy and detailed theoretical calculations used to reveal and identify elastic excitations inside the band gap of hypersonic hybrid superlattices. Surface and cavity modes, their strength and anti-crossing are unambiguously documented and fully controlled by layer thickness, elasticity, and sequence design. This new soft matter based superlattice platform allows facile engineering of the density of states and opens new pathways to tunable phoxonic structures.

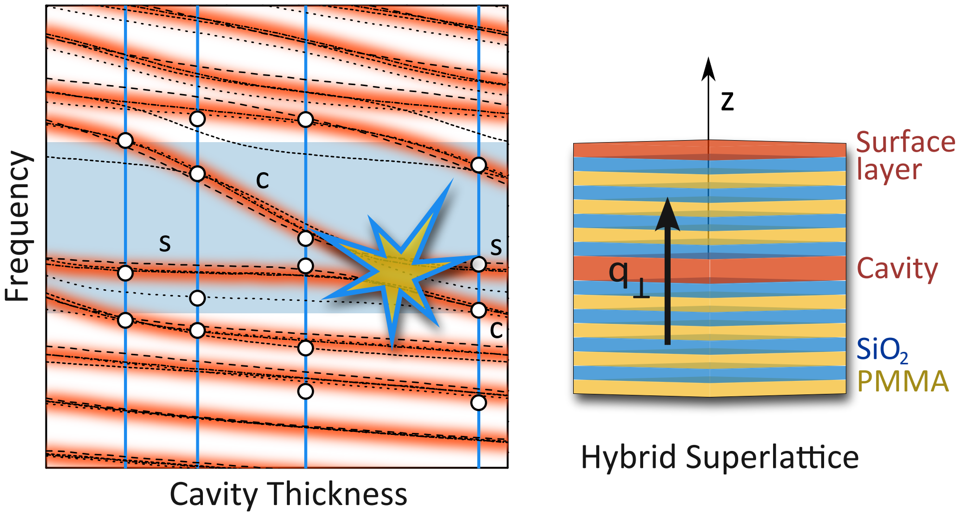

This Chapter is based on:
D. Schneider, F. Liaqat, E. H. El Boudouti, O. El Abouti, B. Djafari-Rouhani, W. Tremel, H.-J. Butt, G. Fytas, *Defect-controlled Hypersound Propagation in Hybrid Superlattices*, submitted to Phys. Rev. Lett.

4.1. Introduction

Selective transmission of elastic waves in superlattices (SLs), reported in 1979, has inaugurated the idea of *phonon filtering* by dielectric Bragg mirrors.[90] Fourteen years later, the study of phononic stop bands in 3D nanostructures was initiated by calculations of the full band structure of periodic composites,[32] a followup of the electromagnetic analogs proposed in 1987.[20] The necessity of combining materials of significantly different acoustic impedance in a periodically ordered assembly is the basis for phononic effects and has been exemplified both experimentally and theoretically.[34,36,39,146,169] SLs largely facilitate the study of phononic crystals, as the complex vector nature of the elastic wave propagation is subdued in one-dimensional structures. This platform allows the discovery of a new class of states and thereby the manipulation of elastic wave propagation in periodic structures. Longitudinal acoustic phonons folded to the Brillouin zone (BZ)[91] and confined acoustic vibrations in a phonon cavity of a SL embedded within an optical cavity[111] have been observed in semiconductor SL by Raman scattering. Defect modes, either surface localized within the frequency gaps of the zone folded phonons[102–104] or surface avoiding with wave vectors in the vicinity of the center[105] and edge of the BZ,[107] have been revealed by Raman and pump-probe experiments. Many applications benefit from SL designs with controlled defects such as coherent phonon generation,[69,94,108,109] concurrent modulation of light and sound,[58,61,111,112] acoustic diodes,[113] and reduction of heat conductivity.[114,115]

However, to date these functional SLs are exclusively based on semiconductor materials with relatively low elastic impedance contrast and strong optical absorption preventing probing far from the surface, while their fabrication requires epitaxial growth under clean-room conditions. Instead, hybrid SLs comprising hard inorganics and soft polymers pose an alternative flexible platform with distinct advantages: large and tunable band gaps,[95,96,101] easy fabrication[97] and variation of total thickness and spacing for concurrent operation at hypersonic phonon and visible photon frequencies. Using these new soft matter based SLs, we present the first unequivocal observation of surface modes and their interaction with cavity modes varying the material and the thickness of the top layer, as well as the thickness and position of the cavity layer. The full theoretical description of both the experimental phononic band structure and the Brillouin light scattering (BLS) spectra is based on a Green's function method in the frame of elasticity theory, as concisely presented in Section 2.2.4 and 2.3.3. This formalism directly accesses the density of states (DOS), which helps to identify the modes inside and near the edges of the 1^{st} BZ that are activated through breaking of the high symmetry. The gained understanding is a precondition for reliable predictions of phonon propagation in periodic composite structures.

4.2. Experimental

4.2.1. Fabrication

One-dimensional Bragg stacks (finite superlattices - SLs) of alternating poly(methyl methacrylate) (PMMA or P) and porous silica (p-SiO_2 or S) layers were built up on piranha cleaned glass substrate by high speed spin coating (5000 rpm; 5040 rpm/s; 20 s). All the layers except the defect layer are coated from the respective stock solutions of 2.2% PMMA in toluene (w/v) and 3.4% colloidal dispersion of silica nanoparticles (LUDOX AS-30) containing ammonia and sodium dodecyl sulfate

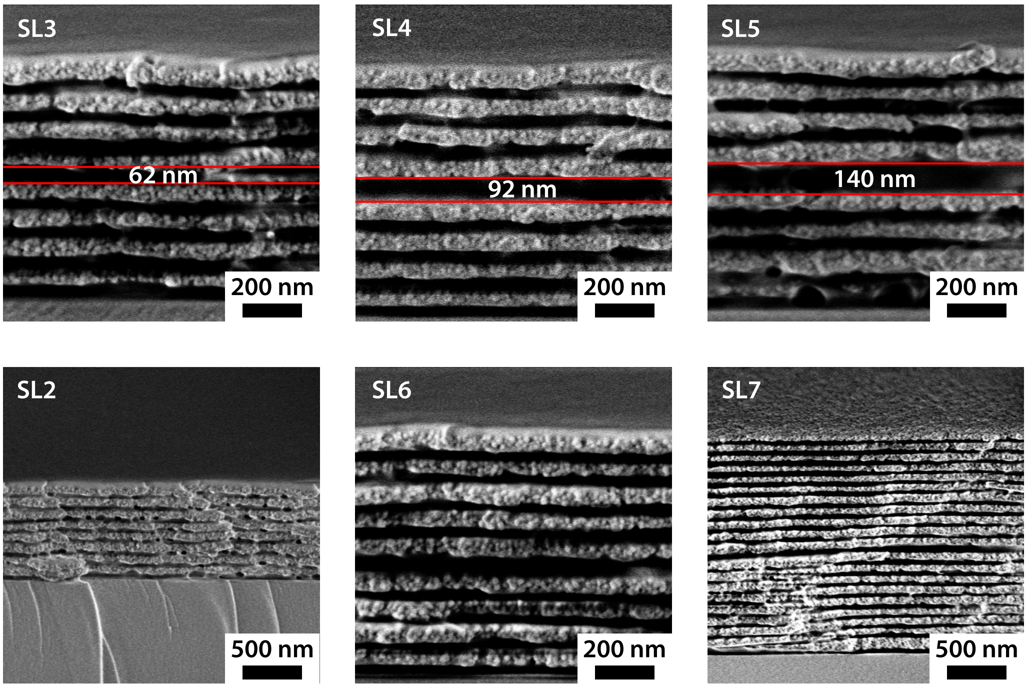

Figure 4.1: Electron micrographs of samples SL2–7.

Table 4.1: Architecture and elastic parameters of the hybrid Bragg stacks.

ID	$d_{\mathbf{PMMA},SiO_2}$ (Layer sequence[a]) / nm	$c_L(SiO_2)$ / ms^{-1}	$\rho(SiO_2)$ / $kg\,m^{-3}$	c_L(PMMA) / ms^{-1}	ρ(PMMA) / $kg\,m^{-3}$
SL1	$\Vert\mathbf{42}\mathit{56}\ \mathbf{42}\mathit{56}\ \mathbf{42}\mathit{56}\ \mathbf{42}\mathit{56}\ \mathbf{42}\mathit{56}\ \mathbf{42}\mathit{56}\ \mathbf{42}\mathit{56}\ \mathbf{42}\mathit{56}\ \mathbf{57}$	3150	1700	2800	1190
SL2	$\Vert(\mathbf{45}\mathit{55})_8\mathbf{80}$	3200	1750	2800	1190
SL3	$\Vert\mathbf{42}\mathit{55}\ \mathbf{42}\mathit{55}\ \mathbf{42}\mathit{55}\ \mathbf{42}\mathit{55}\ \mathbf{62}\mathit{55}\ \mathbf{42}\mathit{55}\ \mathbf{42}\mathit{55}\ \mathbf{42}\mathit{80}\ \mathbf{54}$	3150	1700	2800	1190
SL4	$\Vert\mathbf{42}\mathit{52}\ \mathbf{42}\mathit{52}\ \mathbf{42}\mathit{52}\ \mathbf{42}\mathit{70}\ \mathbf{92}\mathit{52}\ \mathbf{42}\mathit{52}\ \mathbf{42}\mathit{52}\ \mathbf{42}\mathit{70}\ \mathbf{44}$	3150	1700	2800	1190
SL5	$\Vert\mathbf{42}\mathit{52}\ \mathbf{42}\mathit{80}\ \mathbf{42}\mathit{52}\ \mathbf{42}\mathit{52}\mathbf{140}\mathit{52}\ \mathbf{42}\mathit{52}\ \mathbf{42}\mathit{52}\ \mathbf{42}\mathit{80}\ \mathbf{45}$	3150	1700	2800	1190
SL6	$\Vert\mathbf{41}\mathit{50}\ \mathbf{41}\mathit{50}\ \mathbf{41}\mathit{50}\ \mathbf{41}\mathit{50}\ \mathbf{95}\mathit{50}\ \mathbf{41}\mathit{50}\ \mathbf{41}\mathit{65}\ \mathbf{41}\mathit{50}\ \mathbf{41}\mathit{85}$	3000	1420	2800	1190
SL7	$\Vert\mathbf{40}\mathit{100}\ (\mathbf{40}\mathit{53})_8\ \mathbf{85}\mathit{53}\ (\mathbf{40}\mathit{53})_{10}$	3150	1700	2800	1190

[a] Bold (italic) numbers denote the thickness of PMMA (SiO_2) layers in nm.

(SDS). In an optimized system of alternating PMMA/SiO_2, heat treatment at 105 °C is an essential part of fabrication after each coating. To study the influence of anomalies in an otherwise perfect stack ($d^P = d^S \sim 50\,\text{nm}$), four samples were prepared, designed to introduce a PMMA defect layer (C) at the position of the 5th bilayer in the sequence $[(PS)_4CS(PS)_3P]$. The thickness of layer C was varied from 42 nm (SL1), 62 nm (SL3), 92 nm (SL4) and 140 nm (SL5). The actual thickness d(C) of each defect layer was determined from scanning electron microscopy (SEM, Fig. 4.1); it is expected to be lower than the targeted thickness due to partial infiltration of PMMA through the porous silica layer. In order to investigate the effect of the surface and cavity defects the samples were designed as follows: SL2 = $(PS)_8C$, SL6 = $(PS)_4CS(PS)_4$ and SL7 = $(PS)_9CS(PS)_9$, where $d_c = d_{P+S} \sim 100\,\text{nm}$.

Table 4.1 provides a detailed description of architectural design of the stacks. The second column lists the thickness of every layer used as a fixed parameter in the theoretical representation of the BLS spectra. The other columns report the sound velocity and density of the two composing materials. While the values for PMMA are constant, the porous silica strongly depends on condition of the stock solution used for casting, hence these values are subject to some deviations from the initially designed value of the SiO_2 layer. The refractive indices of the composing materials are as follows: n(substrate) = 1.46, n(PMMA) = 1.49, $n(SiO_2)$ = 1.46 and n(air) = 1. For the sake of simplicity, we assumed an effective refractive index ($n = 1.47$) for the calculation of the Brillouin spectra. The ratio of the photoelastic constants was set to $p_{\text{PMMA}}/p_{\text{SiO}_2} = 2$. We assumed the thickness of the SiO_2 layer underneath the top PMMA layer slightly larger in order to optimize the agreement with the experimental BLS spectra. However, this fine adjustment doesn't affect the mode count, i.e., no additional modes show up in the observed band gap region.

4.2.2. Brillouin spectroscopy

Brillouin Light Scattering (BLS) is as a non-destructive and non-contact technique (Section 2.4) to probe the propagation of (thermally activated) propagating phonons at hypersonic frequencies (GHz).[38] It is a sensitive tool to study structural and morphological features in composite materials, given that the phonon wavelength $2\pi/q$ commensurates their characteristic (periodic) spacing a, i.e., $q\,a = \mathcal{O}(1)$. Hence, BLS is of particular interest for the study of phononic structures with lattice parameter at few hundred nanometers. Photoelastic interaction between single mode incident photons with wave vector $\mathbf{k}_\mathrm{i}$ and thermally excited phonons give rise to momentum transfer $\mathbf{q} = \mathbf{k}_\mathrm{s} - \mathbf{k}_\mathrm{i}$ along a specified direction determined by the scattering geometry (with $\mathbf{k}_\mathrm{s}$ being the wave vector of the scattered photons). The associated phonon energy is represented by the frequency shift ω of inelastically scattered light of a single-mode (532 nm) laser beam, known as the Brillouin doublet. These small shifts (few GHz) are resolved by an actively stabilized tandem FP interferometer. Typical accumulation times for Brillouin spectra in thin ($\sim 1\,\mu\mathrm{m}$) composite films range from 12 to 24 h. Periodic structures with reciprocal lattice vector G require momentum conservation via $k = q + G$. The dispersion relation along a selected propagation direction is represented by the plot $\omega(k)$. Here, we focus on wave propagation along the axis of periodicity a.

Experimental (theoretical) spectra for various q-values are shown in black (red) together with the total DOS for each SL in Figs. 4.2 and 4.3. Good overall agreement is obtained using the elastic and geometrical parameters listed in Table 4.1.

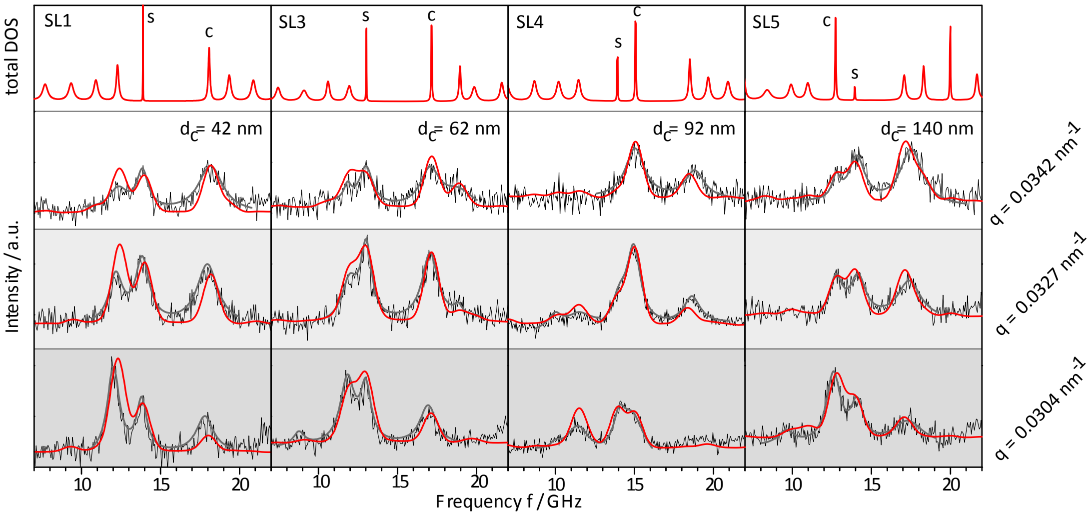

Figure 4.2: a) Experimental BLS-spectra for the four samples SL1, SL3, SL4, and SL5 at three q-values. Effective refractive index $n = 1.47$.

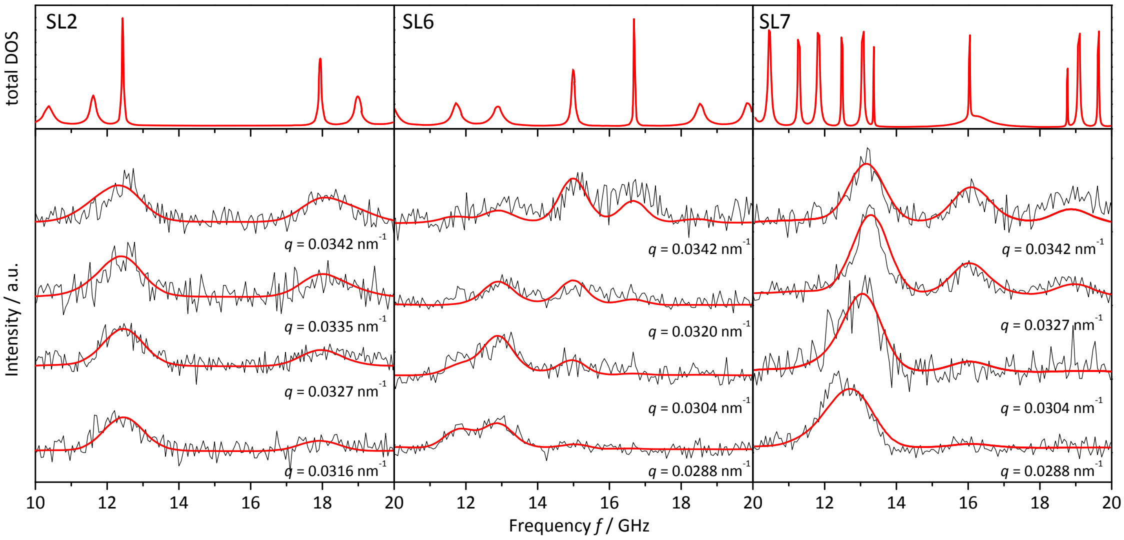

Figure 4.3: Spectra and DOS for SL2 (left panel), SL6 (middle panel) and SL7 (right panel).

4.3. Results and Discussion

Hybrid SLs with uniform lattice spacing exhibit large band gaps for phonon propagation normal to the layers.[95,96] Structural disorder due to thickness fluctuations (∼5%) was accommodated by the BLS instrumental width rendering the spectral pattern in the band gap region robust.[96] The theoretical spectra were convoluted with an instrumental function to represent the corresponding experimental BLS spectra. In this approach we can account for both the instrumental resolution and the conceivable weak hypersonic absorption in the hybrid SL structures. In fact, the acoustic attenuation, which can be described in the theory by using complex sound velocities for each sublayer, essentially causes broadening of the peaks in the DOS and hence the BLS spectra.

Insertion of defects into the hybrid SLs can, in principle, be realized by a manifold of different ways, e.g., variation of thickness and materials. Here, defected SLs are exemplified by surface and cavity layers of either constituent material (Table 4.1). The control of boundary conditions is implemented by the choice of the surface layer. The SLs are terminated with either a hard SiO_2 or soft PMMA layer that strongly impacts the band gap region as reported herein.

4.3.1. Surface modes in defected superlattices

Figure 4.4 is a paradigm for surface-defect induced qualitative changes in the band diagram as illustrated for SL1 with eight bilayers (8 BL) and PMMA surface layer (Table 4.1 and Fig. 4.4f). A new mode with frequency around 14 GHz falls inside the band gap region of an infinite defect-free SL;[96,101] the gray lines in Fig. 4.4a represent theoretical calculations for an infinite SL. The small thickness of SL1 enables mode resolution in the BLS spectrum (Fig. 4.4d) as the separation between the three modes (DOS in Fig. 4.4b) exceeds the instrumental width (∼0.5 GHz). Moreover, modes along the longitudinal acoustic (LA) branch are more intense than along the folded FLA^{-1} [96,170] as suggested by the contour plot in Fig. 4.4a. Hence, suitable q values have been selected for a strong detection (white circles in Fig. 4.4a). The optimal design of the present SL was based on theoretical simulations of the BLS spectra and the band diagram: thinner SLs, e.g., with 5 BL would reduce the BLS signal and the sampling quality of the dispersion relation (Fig. 4.4g); thicker

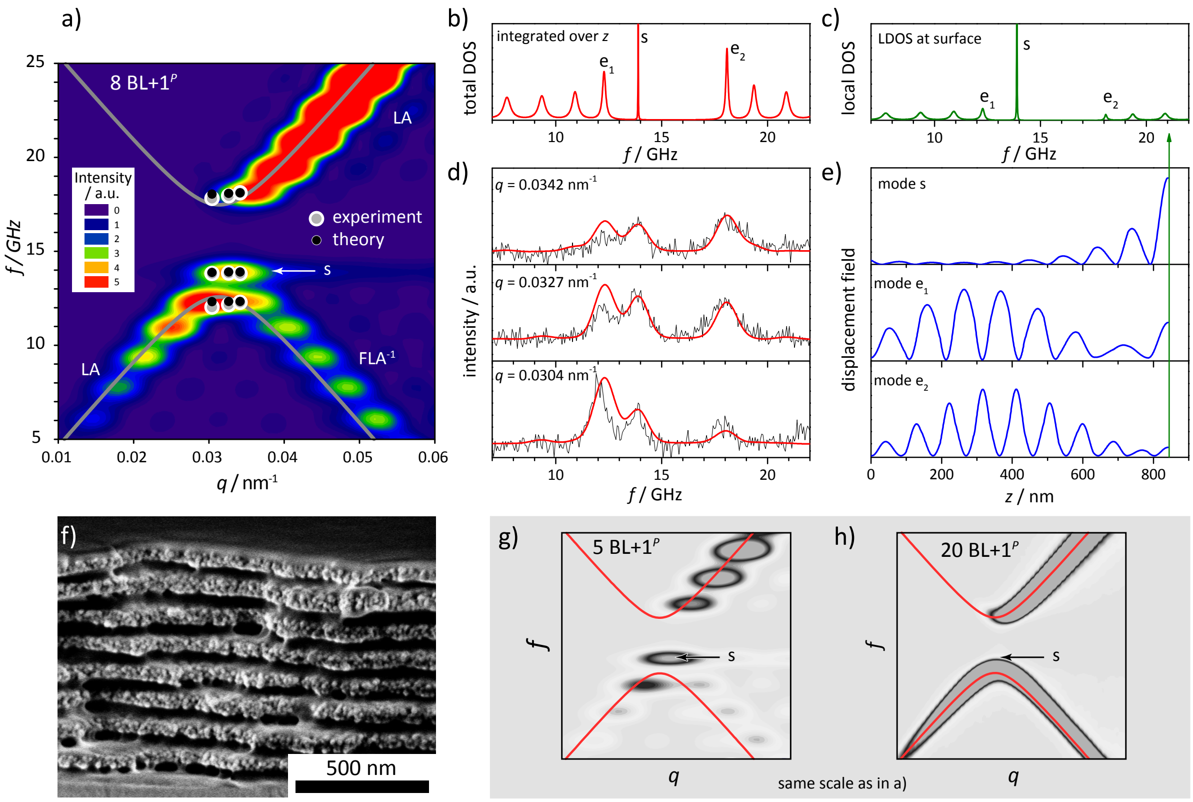

Figure 4.4: a) Dispersion relation for SL1 (Table 4.1) with 8 bilayers (BL) and a PMMA surface layer (17^P). The theoretical Brillouin intensity is given as a color scale and the dispersion of an infinite SL as gray lines. Peak positions of experimental (theoretical) spectra are given as white (black) circles b) Total density of states and local DOS at the surface (c) with indicated edge $\mathtt{e}_{1,2}$ and surface modes `s`. d) Experimental (theoretical) Brillouin spectra in black (red) at three q values. e) Displacement fields of the modes indicated in c). f) Cross sectional electron micrograph of SL1. g,h) Mode separation and strength of the surface mode `s` in SLs with 5 BL (g) and 20 BL (h); mode `s` (indicated by arrows) is hardly discernible in h).

SLs (20 BL) would decrease the separation of the individual modes rendering their experimental resolution hard (Fig. 4.4h). These finite size effect calculations for SLs have been reported by some of the authors earlier.[146] Some of these modes are observed as sets of small satellite lines in high-resolution Raman spectra.[92,171,172] However, this is the first experimental documentation utilizing the advantages of hybrid SLs and coherent BLS.

The total DOS for SL1 in Fig. 4.4b reveals three main contributions, the upper ($\mathtt{e}_2$) and lower ($\mathtt{e}_1$) edge modes, and the surface mode (`s`), whose nature can be identified

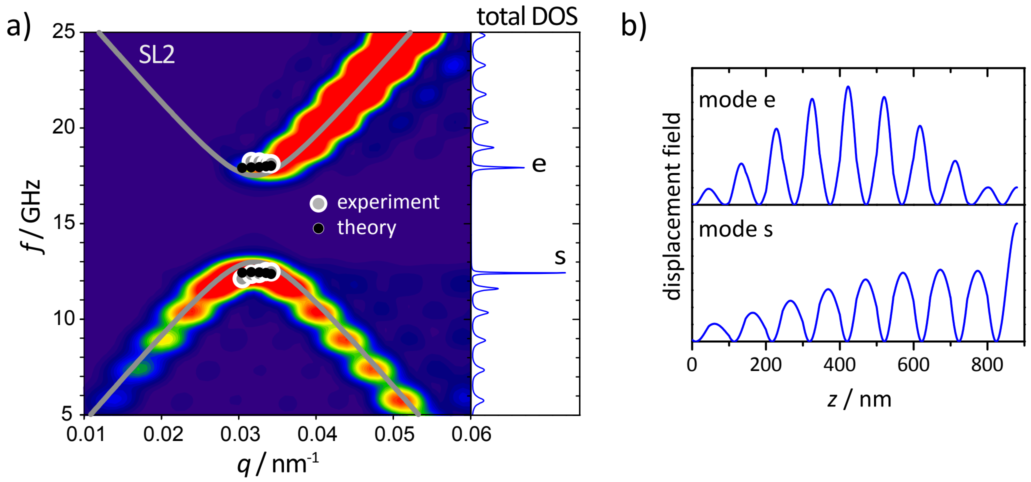

Figure 4.5: a) Dispersion relation and Brillouin intensity for SL2 with a thicker surface layer of PMMA compared to SL1. The gray lines indicate the band gap for the infinite SL. b) The displacement field reveals the upper edge mode (`e`) to be a surface avoiding mode while the lower band edge mode is merged with a surface mode `s` with slow decay into the SL.

by their displacement fields (Fig. 4.4e). This mode assignment is further supported by the pattern of the local DOS at the surface (Fig. 4.4c). It should be noted that the peak in the DOS associated with this `s`-mode becomes narrower as the number of BL increases; the coupling strength of the `s`-mode with the substrate modes weakens with surface-substrate separation. Hence, after convolution of this `s`-peak with the instrumental function, its documentation in the experimental BLS spectrum is severely affected. In fact, the contour plots for the notional SLs in Figs. 4.4g (5 BL) and 4.4h (20 BL) indicated by the `s`-arrows demonstrates the suppression of the `s`-mode with the SL thickness.

The local DOS at the surface (Fig. 4.4c) underlines the importance of the `s`-mode, while the `e`-modes have their maximum displacement centered in the middle of the SL (Fig. 4.4e). Moreover, the envelope function of the displacement field for mode $\mathtt{e}_2$ almost vanishes at the surface. The latter can therefore be qualified as a surface avoiding mode (SAM) recently reported for semiconductor SLs.[107,173] Additional evidence of the surface mode is its dependence on the top layer thickness.[146,174] Theoretically,[146] the frequency of mode `s` should decrease with d_s and its frequency could then be easily tuned inside the gap.

In fact, SL2 (Table 4.1) nicely exemplifies this situation as demonstrated by the good agreement with the theoretical predictions in Fig. 4.5. The upper band edge mode behaves as a SAM, whereas the lower edge mode is merged with a surface mode close to the lower band (gray line) and decays slowly into the SL.

4.3.2. Interaction of cavity and surface modes

Insertion of cavity layers in the interior of the SLs as schematically shown in Fig. 4.6c represents a second class of defects distinctly manifested in the band diagram. Additionally, a cavity mode (`c`) appears which can be affected by the interactions with mode `s`. In the gap region, Fig. 4.6a shows the variation of the frequency of modes `s` and `c` with the thickness of a cavity located in the middle of a 8 BL-SL. While the frequency of mode `s` remains almost independent of the cavity thickness d_c, the frequency of mode `c` decreases monotonically with d_c. When the two frequencies of modes `c` and `s` approach each other, the interaction between their evanescent fields

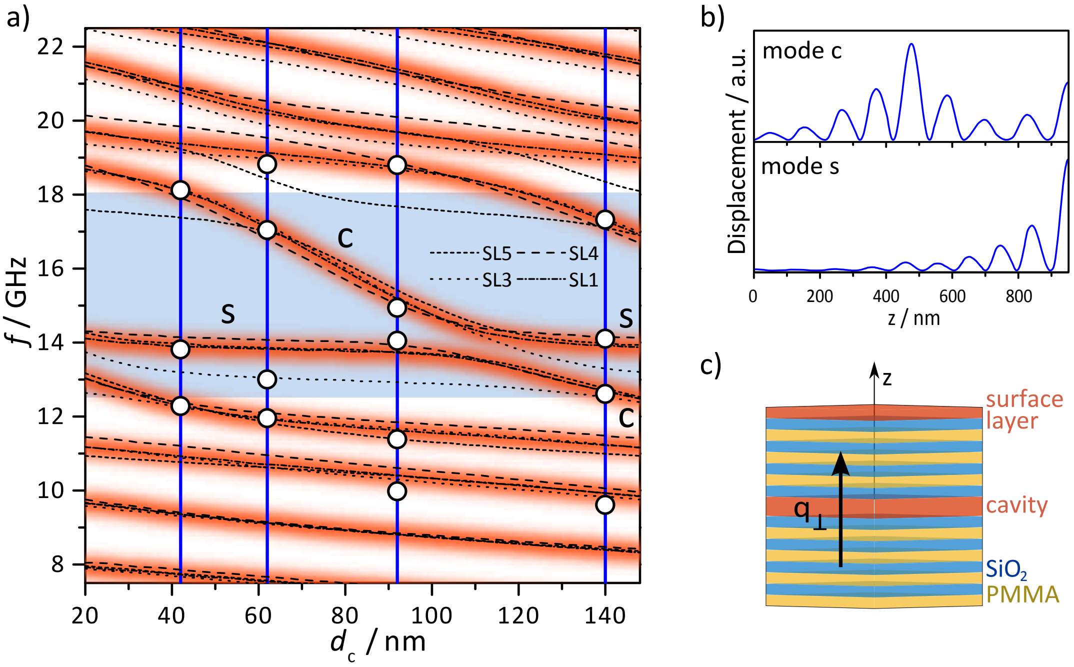

Figure 4.6: a) Mode dispersion around the Bragg gap as function of cavity thickness. As the central PMMA layer is enlarged the cavity mode shifts inside the band gap and interacts with a surface mode for large cavity stacks. Experimental data are given by circles. The shaded region denotes the gap region of SL1. b) Displacement field for modes `c` and `s`. c) Schematic indicating the position of the surface and cavity layers.

leads to an anti-crossing of the dispersion curves (Fig. 4.6a). For this observation a relatively small spatial separation between surface and cavity layers is required.

To address this predicted behavior experimentally, the thickness of the cavity layer located in the middle (9^P) of the hybrid SLs (SL1,3–5, Table 4.1) was stepwise increased (from 42 nm to 140 nm) while keeping the thickness of the surface layer roughly constant ($d_s \sim 50\,\text{nm}$). At large d_c, mode `c` anticrosses mode `s`, but maintains the characteristic features of a cavity mode as proven by the displacement plot (Fig. 4.6b). These findings conform well to theoretical work on the interaction of surface and cavity modes.[146]

4.3.3. Surface modes by hard cap layers

SLs terminated with the high elastic impedance layer exhibit no surface modes.[96,175] However, we show that if the top hard layer is significantly thicker than its precursor layer (inside the SL) the surface can again support a localized mode. Figure 3.4 displays the band diagram for SL6 bearing a SiO_2 top layer with $d_s \sim 2\,d_{SiO_2}$. According to the associated DOS, two of the well-separated modes inside the gap are identified as the surface mode (~16.5 GHz) and the cavity mode (~15 GHz) based on the displacement field (not shown). This is a clear evidence of the existence of the surface mode irrespectively of the rigidity of the top layer. In agreement

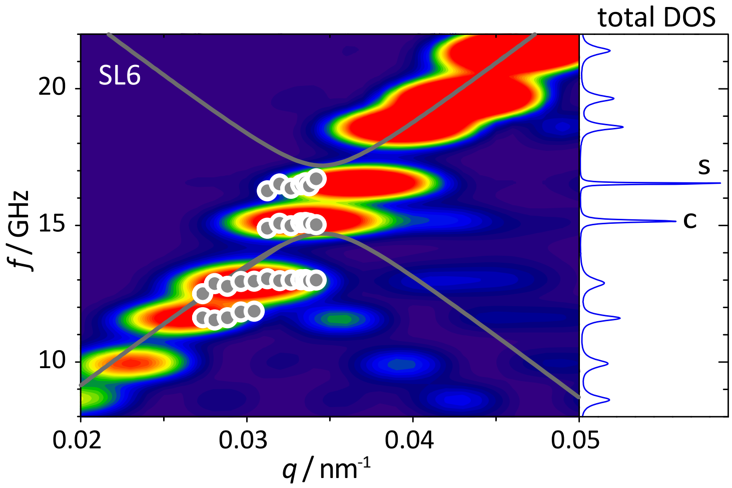

Figure 4.7: Dispersion relation with Brillouin intensity and DOS for SL6 (with a thick SiO_2 surface layer), which accommodates two well-separated modes in the band gap region, a surface (`s`) and a cavity mode (`c`). Experimental data is given by white circles.

with theoretical predictions[174] the existence of surface modes depends both upon the material and thickness of the top layer. Further, Fig. 3.4 shows the concurrent existence of mode `s` induced by SiO_2 at the surface and mode `c` induced by the PMMA layer in the middle of SL6. Similar to Fig. 4.6, these modes may interact with each other inside the band gap when changing the thickness of PMMA and/or SiO_2 layers.

4.3.4. The semi-infinite case

Finally, in the semi-infinite SL7 (Fig. 4.3) the experimental peaks are in fact the sum over several DOS contributions. It consists of a 20 BL SL with a PMMA layer in the middle and a SiO_2 cavity layer near the glass substrate. The experimental BLS peaks represent the sum of different SL modes due to their closer proximity and hence the band diagram (Fig. 4.8) approaches that of infinite SL (no boundary conditions) with a large normal incidence longitudinal Bragg gap (gray lines). However, the fine structure due to the PMMA cavity (mode c_1 at ~16 GHz) is robust to the total SL thickness. In fact, this cavity mode arises from the superposition of two cavity modes as depicted in the right panel of (Fig. 4.8). In addition to the PMMA c_1-mode, the DOS shows the presence of the SiO_2 cavity (c_2-mode) which is much broader due to its higher coupling to the substrate modes owing to the proximity

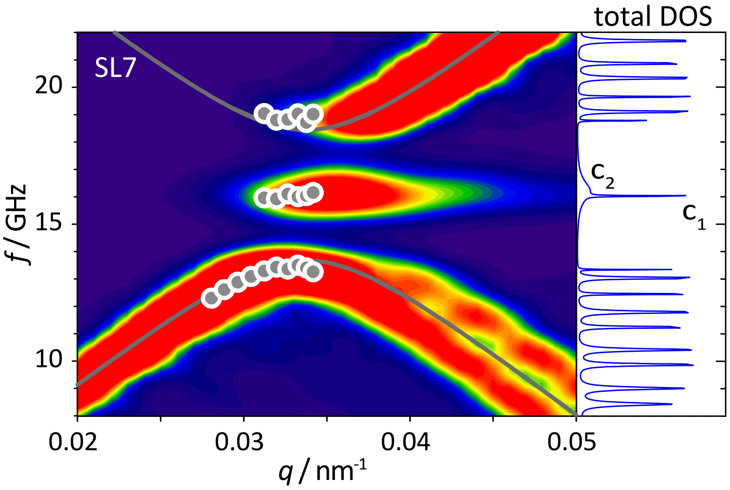

Figure 4.8: Dispersion relation and DOS for the semi-infinite SL7. The modes combine to continuous bands and align with the dispersion for infinite SLs. Cavity layers gives rise to a flat band (modes c_1 and c_2) inside the gap.

of this cavity to the substrate. Despite their different width, both contributions are needed to account for the total intensity of the defect mode.

4.4. Conclusions

The phononic band structure of hybrid SLs is proven to be very sensitive to periodicity perturbations due to the breaking of high symmetry by introduction of defect layers. We presented the first unambiguous experimental evidence for the existence and significant interaction of surface and cavity modes in finite SLs supported by well-established theoretical predictions. The strong response to layer thickness and sequence opens pathways to phononic devices based on soft matter. Dynamic tuning of cavity modes and interaction with other defect modes under external stimuli (e.g., phase transformation using thermo- or chemiresponsive layers) could be used for detection applications. Finally, because of both acoustic and optical mismatch of the composing materials, hybrid SLs constitute a platform for new dual phononic-photonic (or phoxonic) structures for concurrent tuning of acoustic transmission in the GHz range and optical transmission in the visible by adjustment of layer thicknesses. For instance sample SL1 displays an optical stop band around 290 nm (Fig. 4.9). Because of the optical mismatch between substrate, air and the layers composing the SL it can act as an optical cavity.

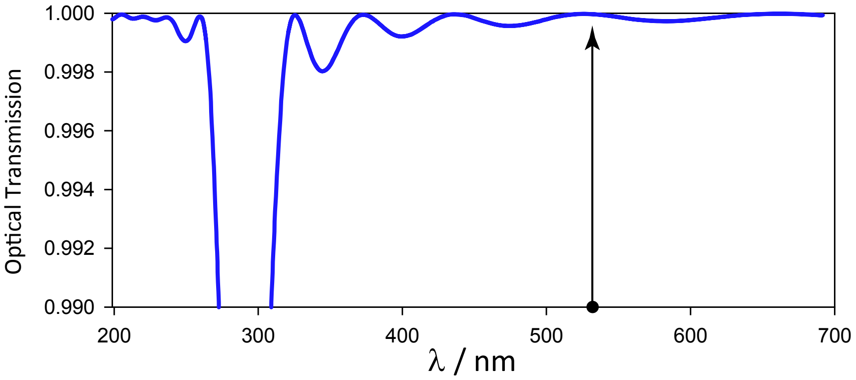

Figure 4.9: Calculated optical transmission of SL1 demonstrating a photonic gap at $\lambda \sim 290\,\mathrm{nm}$. The probing wavelength in this experiment is 532 nm, i.e., at a maximum of transmission (black arrow).

Part III.

Colloidal Phononics

5. Vibration Spectroscopy of Weakly Interacting Mesoscopic Colloids

In this Chapter, Brillouin spectroscopy is used to study the vibrational dynamics of clusters of polystyrene (PS) spheres with different size. In a first approximation, the spectra can be described by a single particle model within the continuum approximation of the Lamb theory, which yields excellent results for particles with diameter $d \sim 500\,\mathrm{nm}$. However, it fails in accounting for the (a) lineshapes of the observed lowest frequency signals in the vibration spectrum of smaller particles ($d \sim 400\,\mathrm{nm}$) and (b) additional very low frequency broad band attributed to phonon propagation in clusters governed by the interactions among particles. A simple model allows to represent the new spectral features and estimate the strength of the interactions and the long wavelength longitudinal velocity in the colloidal clusters. Annealing near the glass transition of PS enhances the interactions, manifested in the low frequency spectrum and the phonon bands associated with the vibrations of the individual spheres. The emerging particle vibration spectroscopy becomes a sensitive tool for the study of thermo-mechanical properties and interactions of colloids.

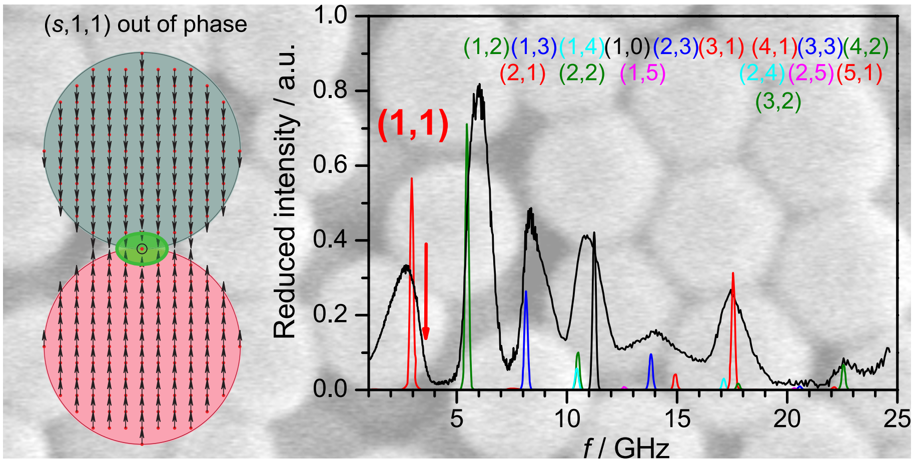

This Chapter is based on:
M. Mattarelli, M. Montagna, T. Still, D. Schneider, G. Fytas, *Vibration spectroscopy of weakly interacting mesoscopic colloids.* Soft Matter 2012, **8**, 4235.

5.1. Introduction

In the last decade, Brillouin light scattering (BLS) has been widely used for the study of the acoustic vibrational dynamics of submicron particles,[38,120,121,127,129,133,176–182] whereas smaller particles can be studied by Raman scattering[183–193] and pump-probe[194,195] techniques. Mesoscopic particles (sizes of few hundreds of nanometers) exhibit BLS spectra with many peaks of comparable intensities. In BLS experiments, spherical particles made of silica,[121,127,180] polystyrene (PS)[127,179,181] or poly(methyl methacrylate) (PMMA)[38,121,182] were investigated. BLS spectra recorded either in disordered powder-like or colloidal crystalline samples were, to a first approximation, very similar. The frequency of all resolved peaks in the BLS spectra were found to be independent of the magnitude of the exchanged wave vector of the scattered light, q, implying localized in space vibrational motion.[127,177] On the contrary, the intensity of the peaks should be q-dependent.[128] However, multiple Mie scattering of the exciting and scattered light, occurring when the light wavelength commensurate to particle diameter, d, almost precludes a q-dependence of BLS.[127] By considering that all wave vectors with magnitude from zero up to the maximum value at backscattering, q_{bs}, contribute to the spectra, frequencies and intensities of the observed peaks were well reproduced by a calculation based on the eigenfunctions of the acoustic vibrations of a homogeneous sphere.[127,128] Even if the spectra do not depend on the scattering angle, the number of the resolved vibration modes and their intensities did, however, depend on the particle size through the product $q_{\mathrm{bs}}d$. For small particles, few low frequency modes are observed; as the particle size increases, new higher frequency modes appear, and the relative intensity of the observed peaks is size-dependent. These studies laid the foundation of the particle vibration spectroscopy, the acoustic analog of the molecular vibration spectroscopy.

So far, no interaction was considered among the spheres which can form clusters of particles due to attractive interactions or bonding between particles. The main contribution to the linewidth of the observed peaks was attributed to a finite size distribution that causes inhomogeneous line broadening, since the frequencies of all acoustic vibrations are inversely proportional to d. This source of line broadening is not present in the experiments using a micro-Brillouin apparatus to investigate single particles.[129,180] The effect of interaction among spheres is important as it was indicated by the BLS spectra of infiltrated (wet) opals.[38,127] If the elastic mismatch between particles and matrix fluid is appreciable, the spectra of wet samples exhibit much broader lines than those of the dry opals associated with a shift of the peak frequency.[127] However, cluster formation due to attractive interactions between particles is also conceivable in dry opals.[179]

Broadening and shift of the single particle lines are expected also in dried aggregates, compared to the values predicted for free spheres in vacuo. The air filling the pores should have a negligible effect in mechanically coupling the spheres, due to the large mismatch of densities ρ and sound velocities c_{L} (longitudinal) and c_{T} (transverse) of the particles (p) and of the air (a), $\rho^{\mathrm{p}}/\rho^{\mathrm{a}} \sim 1000$, $c_{\mathrm{L}}^{\mathrm{p}}/c_{\mathrm{L}}^{\mathrm{a}} \sim 10$, $c_{\mathrm{T}}^{\mathrm{p}}/c_{\mathrm{T}}^{\mathrm{a}} = \infty$. More important should be the interaction caused by non-covalent or covalent bonds at the contacts among the spheres. This effect was recently studied for a coupled pair of spherical particles by continuum calculations.[196] The strength of the interaction was modulated by considering two interpenetrating spheres with centers at different distances $D < d$. Each localized vibrational mode of the single sphere is split into a doublet of modes of the dimer. For a weak interaction, the eigenmodes of the dimer can be regarded as the superposition of one eigenmode for each sphere with in-phase or out-of-phase oscillations of the two spheres.

In this Chapter, we demonstrate the sensitivity of the Brillouin vibration spectroscopy of mesoscopic clusters of spherical particles to measure the elastic constants and unveil interaction mediated effects among the particles. High resolution BLS spectra were recorded at room temperature for dry films prepared from suspensions of (elastically soft) PS particles with different diameters (90–550 nm). The strength of particle contacts was experimentally tuned by short thermal annealing near the glass transition temperature T_{g} of PS. The rich shape of the overall vibration spectrum and in particular its low frequency region near the Rayleigh line was considered theoretically for a face centered cubic (fcc) crystal of spherical particles. The dynamics of each sphere is simulated by an atomistic model with a finite number of atoms on a cubic lattice. A single atom is shared by two nearest spheres. The strength of the interaction is constant but its effect can be modulated by changing the number of atoms in the spheres. Each single particle acoustic mode is transformed on a shallow phononic band, except for the six translational and rotational modes. While these modes have zero frequency in the single free sphere, the corresponding bands of the crystal have important dispersion. The low frequency band in the BLS spectrum is attributed to these longitudinal phonons of the clusters, allowing the estimation of both the strength of the interaction among the particles and the long wavelength sound velocity in the cluster. The present study is a clear jump forward towards the foundation of the particle vibration spectroscopy of spherical colloids, so far.

5.2. Experimental

5.2.1. Samples

Particles with $90\,\mathrm{nm} < d < 550\,\mathrm{nm}$ were prepared by emulsion polymerization reported elsewhere.[123] Their diameter was determined by scanning electron microscopy (SEM) (1530 Gemini with acceleration voltages between 0.2 and 1.0 kV, inLens detection) averaging over at least 100 particles. The size polydispersity ranged from 7% to 2% for the smallest (93 nm) and largest (550 nm) sizes, respectively. For the BLS experiment, nontransparent dry powders of latex spheres were prepared by drop casting from their aqueous suspensions on a glass substrate and subsequent solvent evaporation under vacuum at ambient temperatures for several hours. In order to affect the interactions at the contact points between the particles in the dry state, we annealed the powder-like film (~20 µm) at different temperatures near T_g (100 °C) of bulk PS, for about two hours inside the BLS setup.[181] The film was then cooled to 24 °C within ca. 20 min with subsequent recording of the BLS spectrum.

5.2.2. Brillouin light scattering

BLS is a unique non-destructive and non-contact technique to probe acoustic excitations, e.g., propagating phonons, localized vibration modes in bulk, films and nanostructured materials at hypersonic (GHz) frequencies (Section 2.4). Hence, BLS is a sensitive index of structure, morphology, micromechanics, and photon-matter interactions in composite materials when the phonon wavelength commensurate their characteristic spacing, i.e., $qd = \mathcal{O}(1)$. BLS uses the interaction between single frequency incident photons with wave vector $\mathbf{k}_\mathrm{i}$ and thermally excited phonons $\mathbf{q} = \mathbf{k}_\mathrm{s} - \mathbf{k}_\mathrm{i}$ along a selected direction determined by the scattering geometry with $\mathbf{k}_\mathrm{s}$ being the wave vector of the scattered photons. In turbid media, $\mathbf{q}$ is ill defined due to light multiple scattering and scattering at all q-values is observed, at any detection angle. For the high resolution temperature BLS experiment, we utilized a set-up consisting of a six-pass tandem Fabry-Pérot interferometer, actively stabilized by a reference beam, a $\lambda = 532\,\mathrm{nm}$ Nd/YAG laser ($\sim 50\,\mathrm{mW}$) mounted on a goniometer and a cell holder allowing q-dependent experiments.[38,181] A typical accumulation time of the vibration spectrum in the colloidal powder-like film was 60 min.

5.3. Theory

The acoustic dynamics of a free homogeneous sphere was described by Lamb within a continuum model 130 years ago.[152] The normalized vibrational modes, $\mathbf{e}_\alpha$, with frequencies ω_α are labeled by four indices, $\alpha \equiv (p, n, l, m)$. Torsional modes ($p = t$) have pure shear motions, whereas spheroidal modes ($p = s$) involve both shear and stretching. The n, l, m indices label the radial and angular vibrations of spheres in analogy to the atomic orbitals. The frequencies ω_α are numerically calculated by using two parameters, c_L and c_T, and analytical expressions of the eigenfunctions $\mathbf{e}_\alpha(\mathbf{x})$, where $\mathbf{x}$ spans the volume of the sphere, are obtained.[197] The contribution of the α-th spheroidal mode to the polarized Brillouin intensity is given by[127,128,198]

$$I_\alpha(\mathbf{q}) \propto \frac{n(\omega_\alpha, T) + 1}{\omega_\alpha} P^2 \left| \int_V e^{-\mathrm{i}\mathbf{q}\cdot\mathbf{x}}\, \mathbf{q} \cdot \mathbf{e}_\alpha(\mathbf{x})\, \mathrm{d}\mathbf{x} \right|^2, \tag{5.1}$$

where $n(\omega_\alpha, T)$ is the Bose-Einstein factor, P is the polarizability density and the integral is over the volume V of the sphere.

We consider an fcc crystal of weakly interacting monodisperse homogeneous spheres with a primitive cell containing a single sphere. The Bloch theorem ensures that the vibrations are phonons with displacements given by

$$\mathbf{u}_{\mathbf{k},\alpha}(\mathbf{r}) = e^{\mathrm{i}\mathbf{k}\cdot\mathbf{X}} f_\alpha(\mathbf{x}), \tag{5.2}$$

where $\mathbf{r} = \mathbf{X} + \mathbf{x}$ with $\mathbf{X}$ being position vectors of the centers of the spheres and the wavevector $\mathbf{k}$ spans the first Brillouin zone (BZ) of the fcc crystal.

The usual approach to phononic crystals starts from phonons, i.e., plane waves traveling the crystal, and considers a mesoscopic periodicity that will break the continuous acoustic bands introducing gaps in the acoustic dispersion curve.[38,199–201] The approach is similar to that used for the electronic bands in crystals: starting from a free electron model, gaps appear for **k**-values at the edges of the BZ in the presence of a potential with the periodicity of the crystalline structure. The weak interaction among the spherical particles suggests an alternative approach similar to the tight-binding model for electrons. The interaction will couple the vibrations of the single spheres such that the discrete vibrational spectrum ω_α will be transformed into bands $\omega_\alpha(\mathbf{k})$.[202] If the interaction between pairs of particles is weak, the mode patterns within each sphere will be very similar to the patterns of Lamb modes of the free sphere. Any perturbation $\Delta\mathbf{e}_\alpha(\mathbf{x},\mathbf{k})$ will be small and limited to small volumes near the twelve contacts with the surrounding spheres. In this case, the acoustic vibrations of the system can be described by

$$\mathbf{u}_{\mathbf{k},\alpha}(\mathbf{r}) = e^{\mathbf{ik}\cdot\mathbf{X}}[\mathbf{e}_\alpha(\mathbf{x}) + \Delta\mathbf{e}_\alpha(\mathbf{x},\mathbf{k})], \tag{5.3}$$

and the perturbation $|\Delta\mathbf{e}_\alpha(\mathbf{x},\mathbf{k})| << |\mathbf{e}_\alpha(\mathbf{x})|$.

For the intensity calculations (Eq. 5.1) different approaches can be considered. The simplest case refers to a transparent crystal with full coherent contribution of the scattering volume to the Brillouin inelastic event. In an fcc crystal, the minimum exchanged q that fulfills the diffraction conditions is $k_{\min} = |\mathbf{G}(111)| = \sqrt{3}\pi/a = \sqrt{6}\pi/d$, where a is the side of the cubic cell with four spheres. On the other hand, the maximum exchanged q is $q_{\mathrm{bs}} = 4\pi n_{\mathrm{eff}}/\lambda$, where n_{eff} is the effective refractive index of the medium (spheres and holes). No diffraction can occur for $q_{\mathrm{bs}} < k_{\min}$ or $d \lesssim 220\,\mathrm{nm}$ ($n_{\mathrm{PS}} = 1.59$, $n_{\mathrm{eff}} = 1.46$ for a volume fraction of 0.74, and $\lambda = 532\,\mathrm{nm}$). In this case, there is no attenuation of incoming and scattered light and the amplitude of the scattered field is

$$\begin{aligned} F_\alpha(\mathbf{q}) \propto & \int_V e^{-\mathbf{iq}\cdot\mathbf{x}}\,\mathbf{q}\cdot[\mathbf{e}_\alpha(\mathbf{x}) + \Delta\mathbf{e}_\alpha(\mathbf{x},\mathbf{k})]\,\mathrm{d}\mathbf{x} \\ & \times \sum_j e^{-\mathbf{iq}\cdot\mathbf{X}_\mathrm{j}} e^{\mathbf{ik}\cdot\mathbf{X}_\mathrm{j}}, \end{aligned} \tag{5.4}$$

where the sum is over the spheres in the scattering volume.

The phonons with $\mathbf{k} = \mathbf{q}$ are allowed, producing the well known Raman and Brillouin selection rules, and in the case of bulk atomic crystals only the low-k

limit, far away from the border of the BZ, can be activated. For the present case of bigger spheres, a large volume of the BZ can be probed. Access to the whole volume of the BZ is allowed for $q_{\mathrm{bs}} > k_{\mathrm{max}} \simeq \sqrt{2}\pi/d$. If $\Delta\mathbf{e}_\alpha(\mathbf{x},\mathbf{k})$ can be neglected, the BLS intensity reflects the contribution of the single sphere.

A second approach refers to disordered clusters with $d \ll \lambda$. Disorder can be introduced by size distribution and fabrication procedures, e.g., drop casting, leading to random sequences of (111) planes and defects. Such clusters should be highly transparent to light with $\lambda \gg d$, as in nanoceramics, where the attenuation is much lower than that calculated for Rayleigh scattering from a random distribution of particles.[203,204] The attenuation in the low-q range is governed by long-range density fluctuations of the particles. Density fluctuations of nanocrystals in nanoceramics are small due to the dynamics of aggregation.[204] For clusters of spherical particles, density fluctuations are weak, even in the absence of crystalline order rendering therefore the transparency high. In this limit ($qd \ll 1$), the BLS spectrum resembles that from glasses. The exchanged $\mathbf{q}$ is well defined, but the acoustic vibrations are not well defined plane waves. Longitudinal acoustic vibration are approximatively plane waves only at low frequencies, producing a sharp peak at $\omega = c_{\mathrm{L}}q$, but the peak broadens with q, as shown by X-ray Brillouin scattering measurements.[205,206] It should be noted that for small particles ($d \ll \lambda$), a different mechanism of inelastic light scattering becomes dominant. This “Raman” scattering (not considered in this Chapter) allows the contribution of $l = 0, 2$ spheroidal mode even at $q = 0$.[128,183–193,207]

A third simple approach refers to turbid multiple scattering media. In this case, the BLS spectra appear completely q-independent.[127] For crystals made of large particles ($q_{\mathrm{bs}} > k_{\mathrm{max}}$), all phonons at any $\mathbf{k}$ in the BZ will contribute to the BLS spectrum. The intensity of any phonon band will be given by Eq. 1, taking the integral over all q-values for $0 \leq q \leq q_{\mathrm{bs}}$, and the shape of the peaks will reflect the density of states (DOS) of the particular band. In a disordered cluster, the vibrations are not plane waves with a defined $\mathbf{k}$, and their spatial Fourier transform contains a distribution of $\mathbf{k}$-vectors. The spectral shape reflects the vibrational DOS of the systems assuming now a rounded shape with respect to the corresponding DOS of the crystal.

An atomistic model can describe how the discrete set of single particle modes (p, n, l, m) is transformed into phonon bands $(p, n, l, m, \mathbf{k})$ of the crystal. Here, we

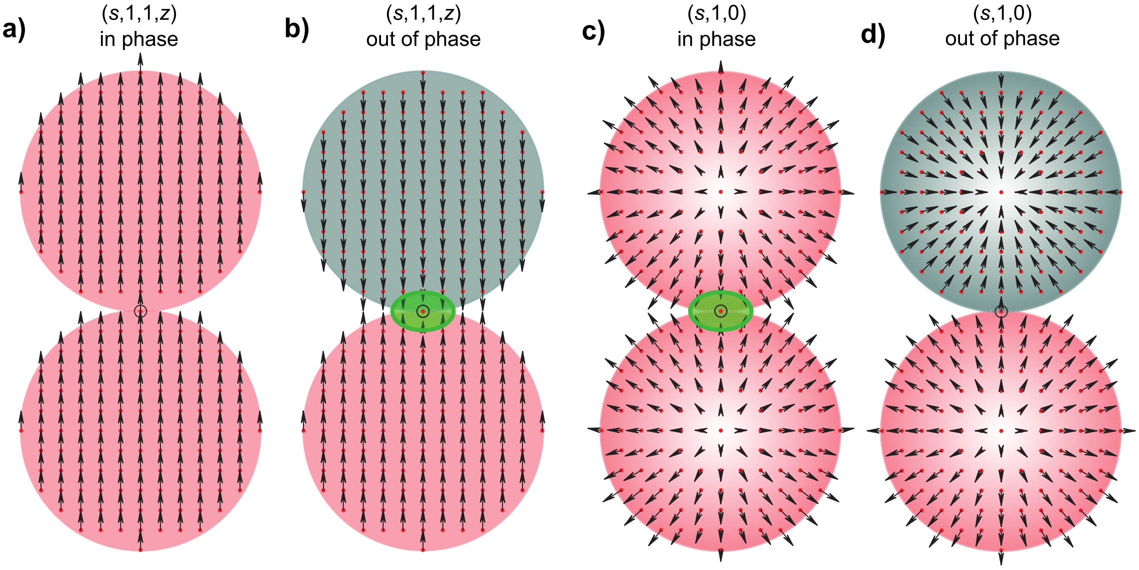

Figure 5.1: Illustration of the pattern (arrows) of four modes of a dimer of interacting spherical particles, simulated by finite clusters sharing an atom. The displacements of atoms in a plane containing the center of the sphere are shown. a) z component of the translational mode of the dimer, derived from the $(s, 1, 1, z)$ Lamb mode of a single sphere. b) In this mode the two spheres move out of phase. The common atom (circled) at the contact region is standing. c) Both spheres expand and contract in phase with motions derived from the (s,1,0) mode. d) The mode deriving from the (s,1,0) mode, but with the two spheres moving out of phase.

resume the main results; a detailed discussion will be given elsewhere. For a weak interaction among particles, a shallow phonon band appears in correspondence to any (p, n, l, m) single particle mode. The band has its low frequency edge at the frequency of the single particle mode. Important dispersion is present only for the (s,1,1) and (t,1,1) phonon bands, which are parent of the zero-frequency pure translational and rotational modes of the free particle. For all modes, the pattern of the vibrational displacement in the interior of each sphere is identical with that of a free sphere, with **k**-dependent phase difference among spheres. The perturbation $\Delta\mathbf{e}_\alpha(\mathbf{x}, \mathbf{k})$ becomes significant only in a small region around the contacts. Figure 5.1 illustrates the model for four modes of a dimer, chosen instead of an fcc crystal for graphical reasons. The zero-frequency dimer mode of Fig. 5.1a is the translation along the dimer axis, derived from the $(s, 1, 1, z)$ Lamb mode of a single sphere. The two spheres move in phase without any strain at their contact. The mode of Fig. 5.1b is the translation along the dimer axis, derived from the $(s, 1, 1, z)$ Lamb

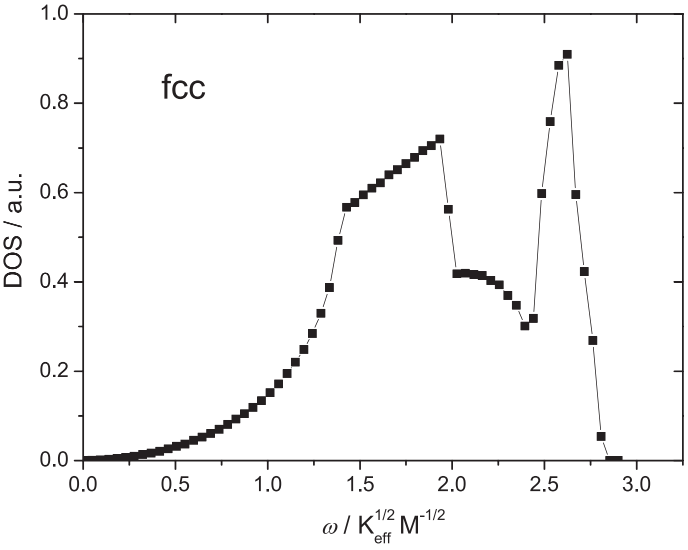

Figure 5.2: Density of vibrational states of an fcc crystal made of masses M connected by springs with stiffness K_{eff}. The highest frequency of the DOS in the tail of the sharp peak (at $\omega(k_{\text{X}}) = 2\sqrt{2(K_{\text{eff}}/M)}$) yields the long wavelength longitudinal sound velocity by Eq. 5.5.

mode of a single sphere, but with the two spheres now moving out of phase. The common atom is standing and the perturbation $\Delta\mathbf{e}$ is significant only in a small region near to the contact. The two modes of Fig. 5.1c,d are derived from the $(s, 1, 0)$ symmetric Lamb mode of a single sphere, with the two spheres moving in and out of phase, respectively. For the in-phase vibration, the common atom is standing and the perturbation $\Delta\mathbf{e}$ is significant only in a small region near the contact. Alternatively, the two spheres move freely in the out-of-phase vibration and hence, this mode maintains the same frequency of the corresponding vibration of the single sphere. All phonons of the fcc crystal maintain these characteristics of the dimer modes. In particular, the (s,1,1,m,$\mathbf{k}$) and (t,1,1,m,$\mathbf{k}$) phonons are nearly rigid relative translations and rotations of each sphere with important strains only in the contact region. This suggests a simple model to describe these two kinds of phonons, assuming rigid spheres connected by springs.

Such a model was used to explain the dynamics of aggregates of macroscopic metal spheres under an external pressure.[208–210] The contacts are modeled by two springs for normal and transverse interactions.[210] Here we will consider a single normal elastic spring with stiffness K_{eff}, since (i) the nature of the interaction is unknown;

(ii) the rotational modes are not relevant for BLS; (iii) transverse interactions have low impact on the dispersion curves of the longitudinal and transverse vibrations.[210] Figure 5.2 shows the density of states of an fcc crystal made of masses M ($M = \frac{\pi}{6} d^3\rho$, where ρ is the density) connected by springs (K_{eff}). The sharp high frequency peak is due to the longitudinal vibrations, whereas the low frequency structures are mainly due to transverse phonons.[141,211] The maximum acoustic frequency is expected for longitudinal modes at the X point of the BZ. For $\mathbf{k} = [k, 0, 0]$, the distance between neighboring planes of atoms moving in phase is $D_{100} = a/2 = d/\sqrt{2}$. The frequency of the acoustic (longitudinal (L) or transverse (T)) modes is $\omega(k) = 2(K_{100}^{\mathrm{L,T}}/M)^{1/2}|\sin(kD_{100}/2)|$ (at the X point $\omega(k_{\mathrm{X}}) = 2(K_{100}^{\mathrm{L,T}}/M)^{1/2}$), where $K_{100}^{\mathrm{L,T}}$ are effective spring constants connecting (100) planes. Each mass is connected to twelve masses in the [110] directions. Four links are with masses in the same (100) plane and two times four links (at 45° with the normal) with masses in the adjacent planes. Therefore, $K_{100}^{\mathrm{L}} = 2K_{\mathrm{eff}}$ and $\omega(k_{\mathrm{X}}) = 2\sqrt{2K_{\mathrm{eff}}/M}$. Eq. 5.5 connects the "long-wavelength" longitudinal velocity (for modes near the Γ-point) to the frequency of the mode at the X-point.[141]

$$v_{100}^{\mathrm{L}} = \left(\frac{K_{100}^{\mathrm{L}} D_{100}^2}{M}\right)^{\frac{1}{2}} = d\left(\frac{K_{\mathrm{eff}}}{M}\right)^{\frac{1}{2}} = \frac{\omega(k_{\mathrm{X}})d}{2\sqrt{2}}. \tag{5.5}$$

The present theoretical calculations are made for colloidal crystals, while the vibrational spectra are recorded for powder-like amorphous colloidal samples. However, experimental spectra of dry PS opals do display the low frequency pattern (see Fig. 2 in Cheng et al.[179]) as for the present PS particles. Hence our approach can yield physically meaningful information on the strength of the interaction among particles and of the sound velocity in the colloidal clusters.

5.4. Results and Discussion

5.4.1. Vibrational spectra of interacting colloidal particles

Fig. 5.3a shows the room temperature BLS spectrum of colloidal clusters of PS spheres with diameter $d = 186\,\mathrm{nm}$ obtained by splicing together spectra with different free spectral ranges (*fsr*: 7.5, 12, and 30 GHz). Figure 5.3b shows the reduced spectrum, where the intensity is multiplied by the square of the frequency,

f^2 ($f = \omega/2\pi$), after splicing of the spectra recorded at three different free spectral ranges and subsequent subtraction of a constant background. This representation allows for a better comparison of the experimental spectrum with the calculated Brillouin activity, the dynamical structure factor in Eq. 5.1,

$$I_\alpha(\mathbf{q}) \cdot \frac{\omega_\alpha}{n(\omega_\alpha, T) + 1} \propto P^2 \left| \int_V e^{-\mathrm{i}\mathbf{q}\cdot\mathbf{x}}\, \mathbf{q} \cdot \mathbf{e}_\alpha(\mathbf{x})\, \mathrm{d}\mathbf{x} \right|^2 , \tag{5.6}$$

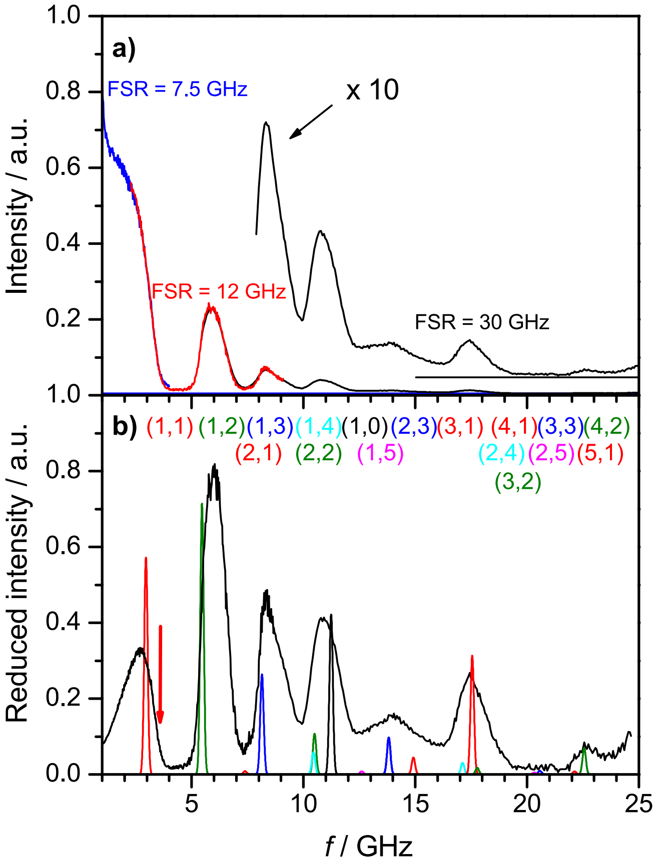

Figure 5.3: a) Brillouin spectrum of a colloidal cluster consisting of PS spheres (d=186 nm) recorded at three different resolutions given by the free spectral range (*fsr* = 7.5, 12 GHz, and 30 GHz) in the figure. b) Reduced Brillouin spectrum, obtained by multiplying the intensity of (a) by f^2, after the subtraction of a constant background indicated by the horizontal line in the high frequency range of the spectrum amplified by a factor 10. The arrow indicates the frequency in the tail of the $(s, 1, 1)$ peak at 20 % of the maximum reduced intensity (see Fig. 5.2). Calculated contributions of 17 (n, l) spheroidal Lamb modes (labeled at the top of the figure) of a single sphere with c_L = 2400 m/s, $c_\mathrm{L}/c_\mathrm{T} = 1.99$ are represented by the sharp lines.

correcting for the thermal factor $\frac{n(\omega,T)+1}{\omega} \propto \omega^2$ at $kT \gg \hbar\omega$. A well defined low frequency peak appears in the reduced spectrum of Fig 5.3b. In the original experimental spectrum this scattering appears as a shoulder of the elastic line. We assign this peak to the longitudinal phonons of the cluster, deriving from the (s,1,1) zero frequency spheroidal Lamb modes, in the presence of a finite interaction among particles. The intensity of the sharp lines with labels indicating the (n,l) spheroidal modes are calculated, with $c_{\mathrm{L}} = 2400$ m/s and $c_{\mathrm{T}} = 1210$ m/s, by Eq. 5.6, summing over the $2l+1$ components, and integrating over all q-values in the range $0 \leq q \leq q_{\mathrm{bs}}$. In the strong multiple scattering limit, the light scattered at all angles $0 \leq \theta \leq \pi$ is collected at any angle of measurement.[127] A single free sphere model is used for the intensity calculation with the simplifying assumptions that the interaction transforms the sharp lines of a discrete spectrum into phonon bands, without modifying the intensity. The calculated spectrum is shown in Fig. 5.3b by the sharp lines at the vibration frequencies of the free particle modes.

Besides the Lamb modes, Eq. 5.6 allows the calculation of the intensity of the (s,1,1) band, a rigid translation of the entire sphere with $\omega_{s11} = 0$ in the free particle. This line should be positioned at $\omega = 0$. However, for graphical reasons and for better comparison with the intensity of the lowest frequency peak, the line is positioned at a frequency $\omega > 0$ on the observed peak. The observed peak (1,1) in Fig. 5.3 is much broader than the calculated DOS of an fcc crystal (Fig. 5.2). Besides the finite but narrow experimental line width, other broadening sources are disorder and anharmonicity, both not considered by the simple model.

Disorder in an fcc crystal is due to a finite size distribution of the spherical particles. For large particles ($d > 500\,$nm) size polydispersity is rather low ($< 2\%$) but increases as the sizes decrease ($\simeq 3\%$ for $d = 186\,$nm). Size polydispersity will introduce finite distributions of both masses and spring constants. Molecular dynamics simulation in systems with mass and spring disorder show that acoustic vibrations are no more pure transverse or longitudinal plane waves. As the frequency increases, the acoustic waves become distorted including extended diffusive vibrations, and the high frequency wing of the DOS is due to localized vibrations.[212] Compared to the crystal case, DOS can have much broader distribution. Anharmonicity could be the source of further broadening. Polymers are known to have important anharmonicity, since longitudinal sound velocity measurements as a function of pressure and temperature show large Grüneisen parameters,[213] and the Brillouin peaks of bulk polymers are quite broad.[182] While the preceding arguments can rationalize the observed broad DOS (Fig. 5.3b vs. Fig. 5.2), it is nevertheless not clear how to extract the stiffness K_{eff} and longitudinal sound velocity v_{L} in the clusters from the experimental BLS spectra of Fig. 5.3. We therefore deliberately chosen to compare the frequency (f_{co}) at 20 % above the (1,1) signal's maximum intensity (arrow in Fig. 5.3b) with the cut-off frequency in the DOS of Fig. 5.2:

$$2\pi f_{\text{co}} = 2\left(\frac{2K_{\text{eff}}}{M}\right)^{\frac{1}{2}}. \tag{5.7}$$

Taking $\rho = 1050\,\text{kg/m}^3$ and $d = 186\,\text{nm}$ for the estimation of M, K_{eff} is computed from eq. 5.7 and $v_{\text{L}} = d\left(\frac{K_{\text{eff}}}{M}\right)^{1/2}$ from Eq. 5.5. A similar analysis was performed for the spectra of the other drop casting colloidal clusters of PS particles with $d = 93$, 130, 260, 306, and 365 nm; for the largest $d = 550\,\text{nm}$, the (1,1) peak is hardly discernible, even in the reduced spectrum. We should note that there is no particular physical reason for the choice of f_{co} at 20% of the signal's maximum intensity, apart for the fact that simulations in glasses show some localized acoustic modes having frequencies higher that the maximum frequency of the corresponding crystal. A systematic error due to the rough model cannot be excluded.

Figure 5.4 shows the reduced Brillouin spectra of all examined samples with seven particle sizes plotted versus fd for better comparison of the shapes of the (n, l) bands that appear superimposed; in fact this presentation accounts for the d^{-1} dependence of the eigenfrequencies of an isolated particle. Pertinent issues emerge from the high resolution vibrational spectra of Fig. 5.4.

First, we consider the lowest frequency band which represents the longitudinal translational band of the colloidal cluster; this band presumably relates to the (s,1,1) Lamb mode. As the particle size increases, its frequency decreases more than those of the other (s, n, l) bands, for which $f \propto 1/d$. Its relative intensity decreases with increasing size and the lowest frequency band is hardly resolved for $d > 500\,\text{nm}$ (Fig. 5.4). This intensity decrease is well reproduced by the calculations with Eq. 5.6 for the three degenerate (s, n, l) translational modes. The frequency of the longitudinal translational band expressed by f_{co} for six particle sizes shown in Fig. 5.5a appears to conform to the steeper scaling $f_{\text{co}} \sim d^{-1.2\pm0.1}$ compared to d^{-1} of the particle eigenfrequencies. The spring constant K_{eff}, obtained from Eq. 5.7, is plotted in Fig. 5.5b. It should be noted that $k_X < q_{bs}$ for all studied samples, but the sample with $d = 93\,\mathrm{nm}$ ($k_X = q_{bs}$ for $d \simeq 120\,\mathrm{nm}$), so that the full DOS of the phonon bands should appear in the spectra.

The computed K_{eff} weakly increases with d, assuming values in the range 13–18 eV/Å^2. For comparison, the covalent bond in H_2 has 27 eV/Å^2. The value of K_{eff} might indicate the presence of many binding sites characterized by much weaker

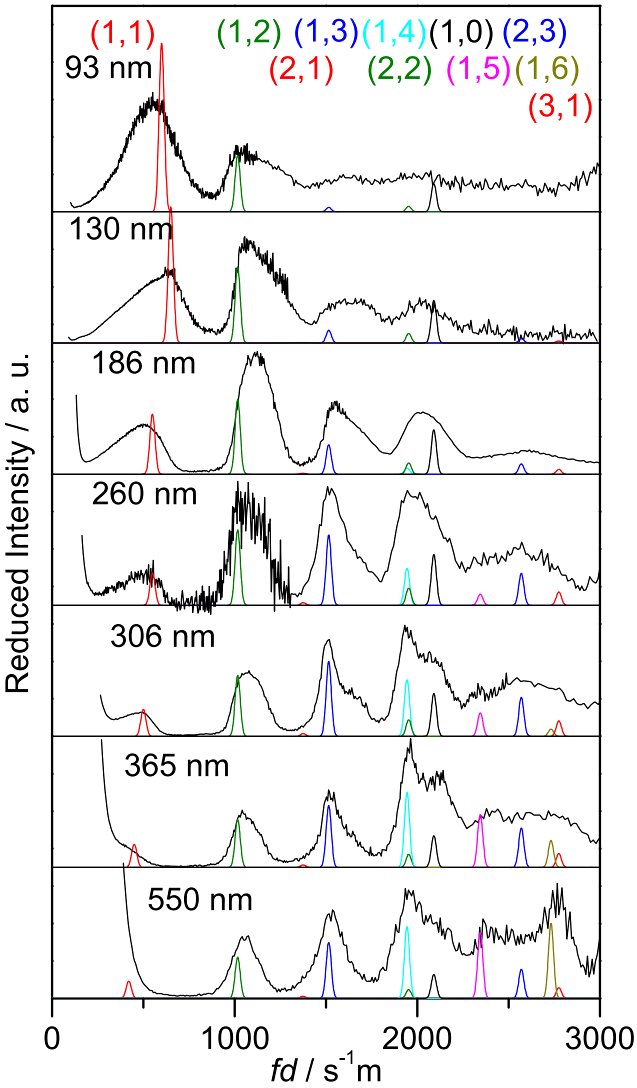

Figure 5.4: Reduced Brillouin spectra of PS clusters of spheres with different sizes plotted as a function of the product $f \cdot d$. Calculated contributions of the (n, l) spheroidal Lamb modes of a single sphere with $c_L = 2400\,\mathrm{m/s}$ and $c_T = 2010$ m/s. Only the Stokes side is shown for clarity.

spring constant, e.g., van der Waals noncovalent bonding. The variation of K_{eff} with d (Fig. 5.5b) can be estimated from the $f_{\text{co}} \propto d^{-1.2}$ relation (Fig. 5.5a): $K_{\text{eff}} \propto Mf_{\text{co}}^2 \propto d^{0.6}$. The estimated error ($\Delta K_{\text{eff}}/K_{\text{eff}} = 2\Delta f_{\text{co}}/f_{\text{co}} + 3\Delta d/d$) does not include possible systematic errors related to the use of a simplified model for deriving f_{co} from the spectra. The dependence of K_{eff} on the particle size cannot be clearly understood within the limitations of the presented simple model.

Figure 5.5c shows the long wavelength longitudinal sound velocity calculated by Eq. 5.5, that decreases with d as $v_{\text{L}} \propto f_{\text{co}}d \propto d^{-0.2}$. The obtained values are

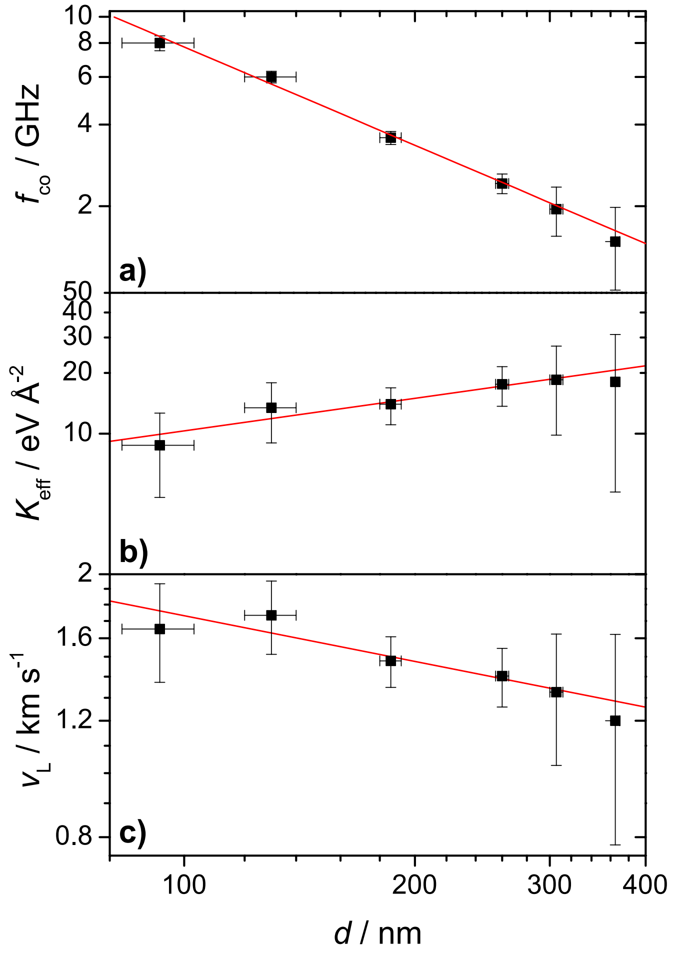

Figure 5.5: a) The high frequency cutoff at 20% of the peak intensity for the lowset frequency peak of the reduced spectra of Fig. 5.4 as a function of the particle diameter. b) Spring constant (Eq. 5.7) for the bonded masses in the colloidal cluster of the PS particles with diameter d. c) Long wavelength longitudinal sound velocity in the colloidal cluster (Eq. 5.5).

of the same order but significantly smaller than the longitudinal sound velocity $c_\mathrm{L} = 2400\,\mathrm{m/s}$ in the bulk PS in the glassy state. Within the rigid sphere model the sound propagation should have stepwise character, as within the Herz-Mindlin model.[208–210] Within a sphere the sound should have a fast propagation, the bottleneck being at the contacts among spheres. In any case, the sound velocity of the system, which also in the Hertz-Mindlin model slightly decreases with the size of the beads, should be much smaller than the sound velocity of the bulk system.[208–210] In fact, the data of Fig. 5.5c clearly show a drop of v_L relatively to c_L, being approximately $c_\mathrm{L}/2$ for the largest particle size. In the absence of a quantitative theoretical estimate for a given size, the data of Fig. 5.5c corroborate the notion that the simple rigid sphere model unveils the essence of the interactions between the spheres. A detailed investigation of q-dependent BLS of clusters with smaller PS particles (to increase the optical transparency) will shed more light on the nature of interactions.

Next, we turn to the effect of interactions among colloidal particles on the localized (n,l) spheroidal Lamb modes, also shown in Fig. 5.4. In particular, the (1,2) and (1,3) bands render the analysis more straightforward, since they appear for all examined particles and are well separated in frequency from other contributions. Relatively sharp symmetric peaks appear in the 550 nm sample, where the effect of the interaction is quite weak as judged from the soft (1,1) mode; $f_\mathrm{co} < 1\,\mathrm{GHz}$.

As the size decreases, the two bands broaden and appear more and more distorted and structured, indicating a progressive increase of the effect of the interaction. The (1,3) band presents a main sharp peak with a higher frequency tail in the sample with $d = 306\,\mathrm{nm}$. This tail becomes stronger with decreasing particle size and finally dominates the spectra for the two smallest sizes. Preliminary results from a simulation of the vibrational dynamics in crystals made of finite spheroidal cluster are in good agreement with the observed spectra, showing that the widths of the phonon bands increase with the interaction, maintaining their low frequency edge close to the frequency of the corresponding single free particle. Furthermore, the effect of the interaction is stronger on the low frequency modes. This explains why the frequencies of the single particle modes appear at the low frequency edges of the observed phonon bands for modes (1,2) and (1,3), as seen in Fig. 5.4.

5.4.2. Enhanced interaction by annealing

A crucial experiment on the origin of the low frequency peak in the vibration spectrum of colloidal clusters and thereby its connection to the (s,1,1) single particle mode would enable a controlled tuning of the interparticle interactions. This requires a systematic elaborative study beyond the aim of the present work. Instead, we decided to modify the particle stickiness through their short annealing near T_g. Figure 5.6 is a compilation of the BLS spectra (all recorded at 24 °C) for two samples with $d = 120\,\mathrm{nm}$ and $d = 182\,\mathrm{nm}$ particle diameter. We started with the virgin sample after drop casting and then the same sample after thermal annealing for 2 h at 92 °C, 97 °C and 102 °C. The two samples were cooled down to 24 °C after each thermal treatment in order to avoid broadening and shift due to the thermal effects of anharmonicity.[214]

After annealing at 92 °C, the lowest frequency peak shifts to higher frequency, indicating an increase of the sound velocity in the cluster caused by a strengthening of the interaction among particles. An increasing blue shift is observed after annealing at 97 °C in the 182 nm sample. At the same time, the (1,2) and (1,3) signals broaden and shift to higher frequencies, evolving their spectral shape. After annealing at 102 °C, the distinct signals disappear and a broad peak, with a maximum at about 13.7 GHz in the 120 nm and at 12.5 GHz in the 182 nm sample, with a long tail towards low frequency, dominates the spectrum. The high frequency tail of the peak at about 14 GHz corresponds to that of the Brillouin peak of a bulk PS in backscattering geometry ($f_\mathrm{bs} = 14.3\,\mathrm{GHz}$ for $c_\mathrm{L} = 2400\,\mathrm{m/s}$). After this last annealing cycle at 102 °C, the colloidal cluster collapses, filmation occurs, and the BLS spectrum contains contributions from q's other than q_bs leading to an asymmetric towards lower frequencies peak. The spectrum for the sample with 120 nm particles exhibits a very broad and asymmetric band peaked at 11 GHz following the annealing at 97 °C. This shape can be accounted for by considering a partial collapse of the cluster with large spatial inhomogeneities of the particle-particle interaction and therefore large inhomogeneities of the sound velocity in different parts of the cluster.

The SEM images of Fig. 5.7, taken after the last annealing at 102 °C in the sample of 182 nm particles, and after an even higher temperature annealing (121 °C) in the sample of 93 nm particles, indicate a largely collapsed film with the particles

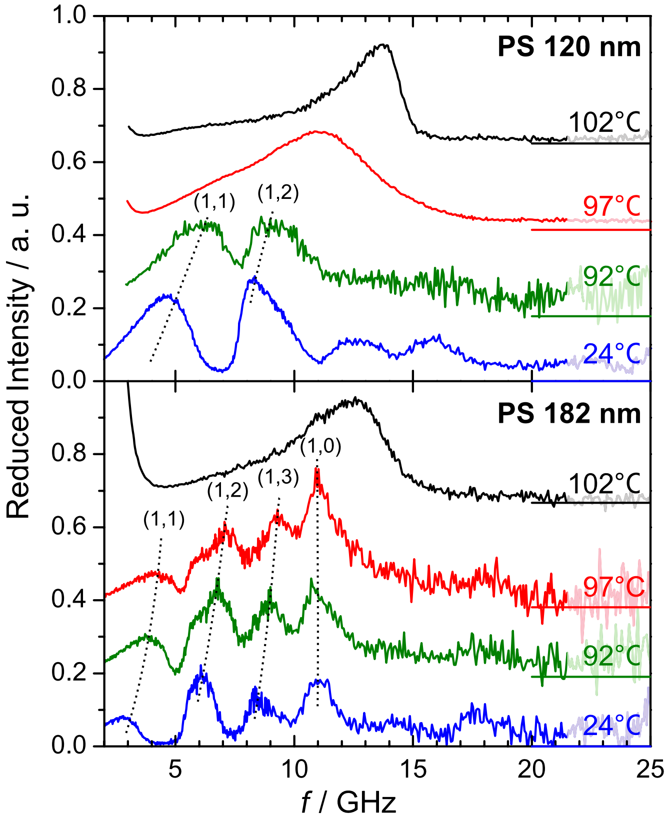

Figure 5.6: Room temperature reduced spectra of the colloidal clusters for two PS spheres (120 nm, 182 nm) at different annealing temperatures as indicated in the plot. After annealing at 92 °C, 97 °C and 102 °C the two samples were cooled down to 24 °C to record the BLS spectrum. The dotted lines connect peaks associated with the (1,1), (1,2) and (1,3) modes.

still maintaining their character. Hexagons appear in the picture showing that the spheres have been deformed to dodecahedrons with large contact areas due to an entanglement between polymer chains of neighboring spheres. The large contact areas strongly increase the effective coupling allowing the propagation of the sound with a velocity close to that of the bulk material (cf. Fig. 5.5c). Yet, the clear blue shift of the (1,1) signal for both particle sizes in Fig. 5.6 is in accord with the increasing particle overlap with annealing temperature seen in the SEM images (Fig. 5.7). The presence of residual porosity, as indicated by the arrows, is the source of important light scattering that avoids the observation of any q-dependence of the spectra, causing the detection of broad Brillouin bands due to scattering at all q-values, at any detection angle.

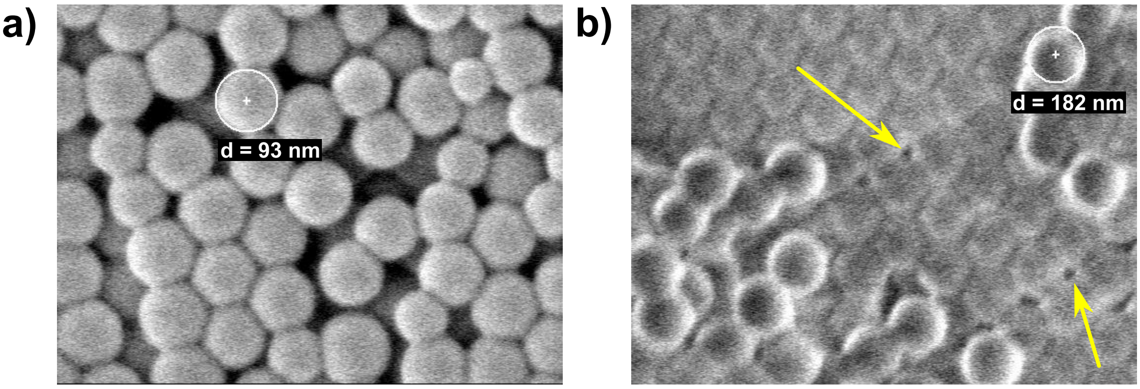

Figure 5.7: SEM images of annealed clusters of PS particles after annealing at high temperatures. a) Cluster of $d = 93\,\mathrm{nm}$ particles after annealing at 121 °C for 2 h. The particles maintain their individual structure but the spheres, when close packed, have been converted to dodecahedrons. b) Cluster of $d = 182\,\mathrm{nm}$ (mean size) particles after annealing at 102 °C for 2 h, with residual porosity clearly indicated by the arrows.

5.5. Conclusions

Brillouin light scattering from dry non-transparent samples of mesoscopic colloids emerges as a powerful spectroscopic tool to resolve numerous vibrational modes, which sensitively index the geometrical and thermo-mechanical characteristics of the spherical particles. Hence, this newly developed "particle vibration spectroscopy" becomes the acoustic analog of the molecular vibrational spectroscopy. While the BLS spectrum (frequencies and intensities) of large particles (diameter $d > 500\,\mathrm{nm}$) can be well represented by the eigenmodes of the individual spheres, the low frequency regime of the BLS spectrum clearly displays different lineshapes. In addition to this pertinent quantitative differences, we observed a new broad band at frequencies lower than the lowest finite energy particle eigenfrequency (1,2) of PS particles. Within the continuum approximation of Lamb theory, we have attributed the failure of the single particle model to the inevitable interactions among the spheres in a dry powder-like sample.

We have experimentally documented the contribution of the spheroidal Lamb modes of a single PS spheres for seven different diameters to the BLS spectrum $I(\omega)$ of drop-cast dry colloidal clusters (Fig. 5.4). The additional low-energy mode was well resolved in the reduced spectrum ($\omega^2 I(\omega)$) for $d < 400\,\mathrm{nm}$, falling at frequencies below the lowest vibration eigenfrequency (1,2). We note that the spheroidal (1,1) mode of an individual sphere is purely translational (zero frequency).

We have accounted for the presence of the aforementioned interactions in an fcc colloidal crystal in which neighboring spheres are connected by an effective spring constant, K_{eff}. Depending on the strength of the interactions (modulated by the spring stiffness), the zero-frequency modes in a single free sphere become dispersive bands of the crystal. In particular, the (1,1) phonon band was identified with the new lowest frequency broad peak of the BLS spectrum, and the cut-off frequency, f_{co}, of the sharp high frequency peak in the density of vibrational states (Fig. 5.2) was related to the longitudinal sound velocity, v_{L}, of the colloidal cluster. Interestingly, $f_{\text{co}}(\propto d^{-1.2})$ drops faster with the particle diameter than the free particle eigenfrequencies ($\propto d^{-1}$).

Comparison between experimental BLS and computed vibrational spectra led to the estimation of K_{eff} and v_{L} in the colloidal clusters consisting of different particle sizes. The sound velocity in the colloidal cluster was expectedly found to be about half of the sound velocity $c_{\text{L}}(2400\,\text{m/s})$ in the bulk PS indicative of a much lower modulus due to the relatively weak interactions among spheres. $K_{\text{eff}} \sim 15\,\text{eV/Å}^2$ ($240\,\text{J/m}^2$) corresponds to several hundreds van der Waals bonds. Qualitatively, we validated these findings and thereby support our simple model, by short thermal annealing of the colloidal samples near the PS glass transition temperature T_{g}. "Sintering" of colloidal crystals strengthens the interactions between neighboring spheres due probably to polymer chain entanglements and non-covalent bonding as indicated by the blue-shift of the (1,1) band BLS spectra (Fig. 5.6) and hence higher K_{eff}. Longer annealing few degrees above T_{g}, however leads to filmation via flowing. A more controlled tuning should be feasible using cross-linked PS particles.

Thus BLS particle vibration spectroscopy does not only reveal the nanomechanical properties of individual colloidal particles, but also provides a simultaneous access to the interactions between neighboring spheres forming the colloidal cluster. These novel insights into the adhesion of colloids extend the applications of a relatively new non-contact technique to new mesoscopic particle systems allowing for the characterization of different types of interactions.

6. Elongated Polystyrene Spheres as Resonant Building Blocks in Anisotropic Colloidal Crystals

This Chapter addresses the mechanical properties of stretched polystyrene colloids (spheroids). Eigenmodes resolved by Brillouin spectroscopy are considered fingerprints of the particles' shape, size and composing materials. A single particle model is used to simulate the experimental data by calculation of all active modes and subsequent evaluation of their contribution to the spectrum. Compared to spheres (high symmetry) more modes contribute to the spectra that limit the resolution at very high frequencies, due to the lifted mode degeneracy. Knowing the nature of the principal modes of spheroids is a precondition to understand the phononic dispersion in the respective colloidal crystals, in particular those responsible for anticrossing interactions with the effective medium acoustic phonon.

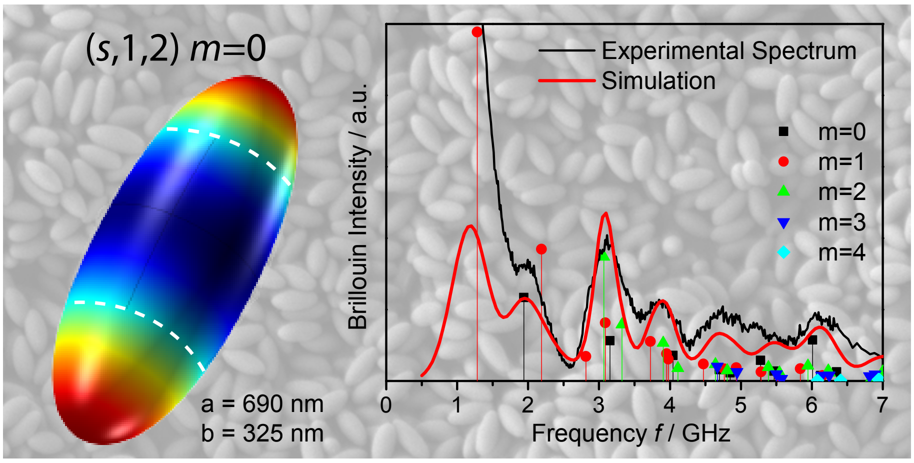

This Chapter is based on:
D. Schneider, P. J. Beltramo, M. Mattarelli, P. Pfleiderer, J. Vermant, D. Crespy, M. Montagna, E. M. Furst, G. Fytas, *Elongated polystyrene spheres as resonant building blocks in anisotropic colloidal crystals.* Soft Matter 2013, **9**, 9129.

6.1. Introduction

In recent years, a vast library of colloidal building blocks has emerged from which novel materials may be created by directed self-assembly.[215–217] An open challenge to using directed self-assembly techniques in the nanomanufacture of complex materials with designed functionality is the ability to i) identify desired ordered structures to achieve such functionality and ii) develop efficient routes to manipulate the interparticle interaction energies to realize the assembly. To accomplish both goals, an understanding of the particle's physical properties is warranted.

Particular interest has emerged in the ordered assembly of ellipsoidal (spheroidal) particles due to the expanded range of final structures and additional flexibility in design allowed by shape anisotropy. The self-assembly of spheroids has been examined at fluid interfaces[218,219] and using magnetic,[220,221] electric[222–224] or flow[225] fields. Specific to electric and magnetic fields, the anisotropy in polarizability along the short and long axis of an ellipsoid allows for preferential, tunable, particle orientation ranging from parallel to perpendicular with the applied field.[226] Combining this orientational control with convective flows to concentrate the particles and "lock-in" the structure circumvents kinetic arrest that occurs at high volume fractions due to glassy dynamics and opens up the possibility of realizing the theoretically predicted close-packed phases of hard ellipsoids.[227,228] From a practical perspective, such structures may impart noteworthy photonic, phononic, mechanical and/or thermal properties to the resulting material due to alignment and periodicity. One recent example of the utility of controlling the orientational order of ellipsoidal particles was presented by Hopkins et al.,[229] where the thermal conductivity of convectively assembled titania films is modulated by the film microstructure.

At room temperature, thermal conductivity in dielectric materials relies mainly on phononic transport of energy in the sub-THz regime. Hence, direct access to the phononic dispersion becomes important. Brillouin spectroscopy has proven to be the tool of choice to investigate phononic band diagram in the GHz range.[40] Colloidal crystals are of particular interest as they can accommodate both Bragg-type band gaps (due to destructive interference of elastic waves) and hybridization band gaps (due to level repulsion between the acoustic branch and a localized mode).[41] In the latter, the exact knowledge of a particle's eigenmode spectrum poses a substantial role. This particle vibration spectroscopy based on Brillouin light scattering (BLS) becomes a valuable method for the mechanical characterization of sub-micron particles.[127] Eigenmode measurements have been reported for spheres,[127,182] nanorods,[116] cubes,[117,120] octahedrons,[118,133] and more complex geometries[194,230] using BLS, Raman and time-resolved spectroscopy. While nanocolumns[231] were shown to shift the resonance line with respect to spherical particles, the eigenmode spectra of elongated spheres have not been fully investigated until now. Some of the aforementioned particles were synthesized from crystalline materials, whose anisotropic mechanic properties affect their eigenmodes in addition to the shape dependence.

Here we present a comprehensive particle vibration spectroscopy study of amorphous polystyrene (PS) spheres and spheroids (elongated spheres with rotational symmetry) utilizing the powerful technique of Brillouin light scattering combined with computational simulation of the spectra. To the best of our knowledge, this is the first work that provides theoretical representation for vibrational spectra of spheroidal nanoparticles studied by Brillouin spectroscopy.

6.2. Experimental

Polystyrene particles were stretched by a matrix assisted elongation process and the change of their eigenmode spectra was followed by Brillouin spectroscopy. The experimental strategy is outlined as follows:

6.2.1. Materials

The seed particles used were 400 nm diameter carboxylate modified PS latex spheres (Invitrogen, Eugene, OR, cat#C37238) with molecular weight of $M_w \sim 240\,\mathrm{kDa}$. The spheroid synthesis procedure is described elsewhere.[124,125] In short, seed particles are dispersed in an aqueous poly(vinyl alcohol) (PVA) solution, spread in a dish and allowed to dry into a thin film after water evaporation. The film is then heated to 145 °C for less than 5 min (oil bath) and stretched to a given strain to produce 2.12:1, 3.52:1 and 3.99:1 aspect ratio prolate ellipsoids of revolution. The processed film was cut into small sections and cleaned from silicon oil by fivefold washing with isopropyl alcohol (IPA). The particles were recovered by dissolution in water/IPA 7:3 (v/v) and the suspensions are observed to be stable. These are washed via stirring (12 h), heating to 75 °C for one hour (to aid PVA removal), centrifugation, decantation and resuspension (sonication) in water/IPA. This cleaning cycle was repeated three times and finally the particles were stored in water. The suspensions were rewashed in 0.1 mM KCl and concentrated to a volume fraction $\phi \approx 0.05$ before being drop cast onto a glass slide and dried at ambient conditions.

The size of the particles is characterized by scanning electron microscopy of the disordered casts (Fig. 6.1) and a summary of the particle dimensions is given in Table 6.1.

Table 6.1: Size characterization of particles studied and material parameters used in calculations. a and b being the long and short axis of the spheroids, respectively. ρ is the mass density and n_{ref} the refractive index at 532 nm.

ID	a/b	a / nm	b / nm	ρ / kg m^{-3}	$n_{\mathrm{ref}}{}^{b}$
S0	1	400±14	–	1050	1.599
S1 [119]	1.28±0.07	459±15	358 ± 16	965.1^{a}	1.540
S2	2.12±0.16	690±42	325±15	921.9^{a}	1.511
S3	3.52±0.20	986±15	280±15	869.4^{a}	1.477
S4	3.99±0.22	1078±93	270±23	854.7^{a}	1.468

^{a} calculated based on stretched particle volume.

^{b} calculated from density via Clausius-Mossotti relation.

6.2.2. Brillouin spectroscopy

Brillouin Light Scattering (BLS) serves as a non-destructive and non-contact technique to probe acoustic behavior, e.g., thermally activated propagating phonons and localized vibration modes in bulk as well as nanostructured materials in the hypersonic frequency regime (GHz). Hence, BLS is a sensitive tool to study structure, morphology and light-matter interactions in composite materials, given that the phonon wavelength $2\pi/q$ commensurates their characteristic (periodic) spacing d, i.e., $qd = \mathcal{O}(1)$. BLS relies on the interaction between single mode incident photons with wave vector $\mathbf{k}_{\mathrm{i}}$ and thermally excited phonons $\mathbf{q} = \mathbf{k}_{\mathrm{s}} - \mathbf{k}_{\mathrm{i}}$ along a specified direction determined by the scattering geometry ($\mathbf{k}_{\mathrm{s}}$ being the wave vector of the scattered photons). For localized modes in nanostructures, BLS gives a structured spectrum with contributions from all modes having a $\mathbf{q}$-component. In multiply scattering samples, $\mathbf{q}$ is no longer well-defined (the sample appears tur-

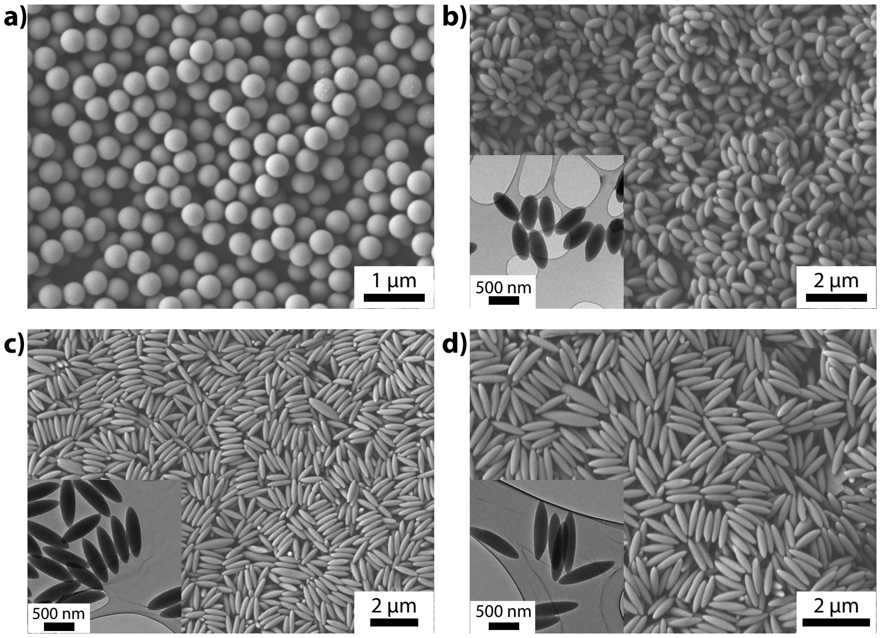

Figure 6.1: Scanning electron micrographs (SEM) of seed spheres S0 (a) and spheroids S2–S4 (b–d) of various aspect ratio. Insets denote transmission images (TEM) of the respective particles.

bid) and hence all possible q-values contribute to the observed spectrum, regardless which scattering angle θ is chosen. Realization of a high-resolution BLS experiment (Fig. 2.12) requires convenient and stable operation of an energy-dispersive detector. This is achieved using a six-pass tandem FP interferometer, which is actively stabilized by a reference beam and capable to detect a (Anti-)Stokes shift of 0.5–300 GHz (via different free spectral ranges – *fsr*). A $\lambda = 532\,\text{nm}$ Nd/YAG laser mounted on a goniometer and a (heatable) cell holder allows for q-dependent and temperature dependent experiments.[38,41] Together, this setup provides the tool-kit necessary for high-resolution acoustic measurements at the nanoscale.

The typical accumulation time of the vibration spectrum in a drop cast powder-like film ranges from 30 to 120 min. Thin films or weakly scattering particles (size and material dependent) may require accumulation times up to 48 h.

BLS spectra obtained at $\theta = 60\,^\circ$ for the samples listed above (Table 6.1) were processed (stitched spectra at *fsr* = 7.5, 15, 30 GHz) and plotted in a common graph (Fig. 6.2). The upper panel (Fig. 6.2a) displays spectra for large changes in asphericity, from sphere up to an axis ratio of $a/b = 3.99$, while the lower panel (Fig. 6.2b)

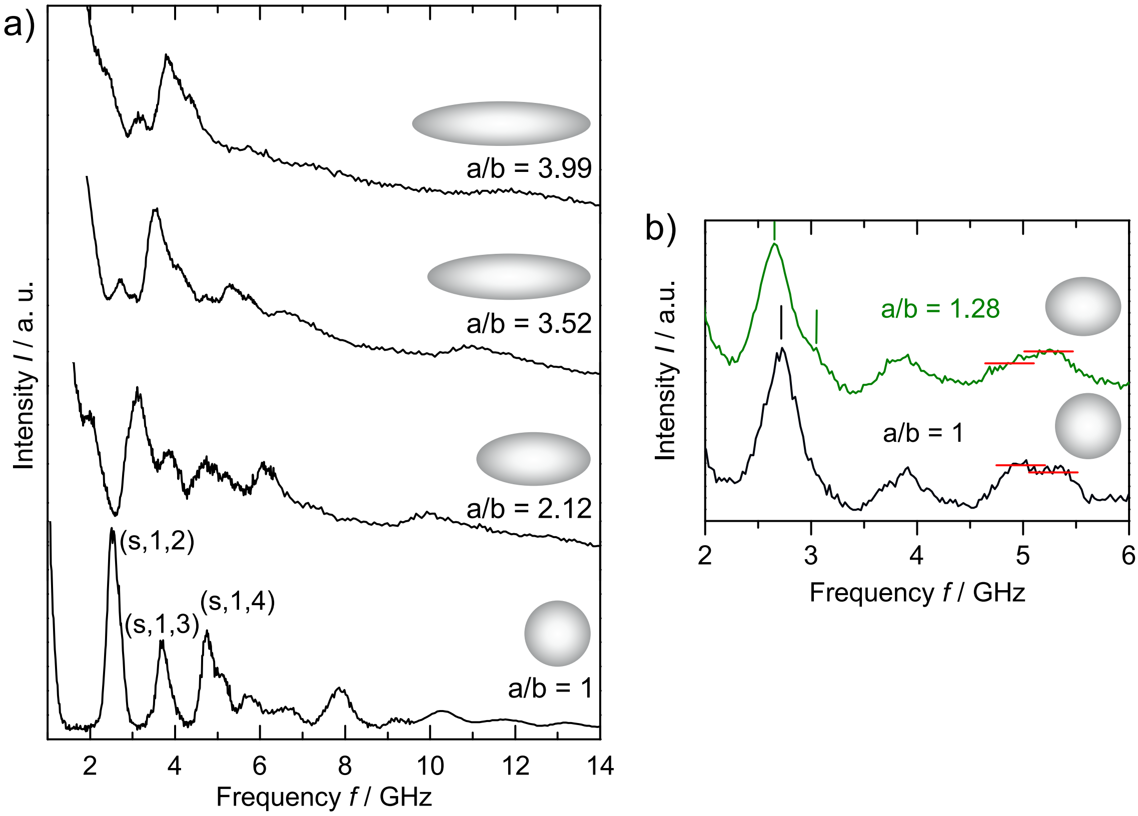

Figure 6.2: a) Brillouin light scattering (BLS) spectra of the spheroids with three different aspect ratios along with the rich spectrum of the seed spheres displaying the contribution of the principal modes $(s, 1, l{=}2;3;4)$ in the low frequency region. b) Onset of asphericity and the accompanying bifurcation of the lowest frequency $(s, 1, 2)$ mode due to the lifting of degeneracy in m.

examines the small differences in the spectrum between the sphere (S0) and the particle with only slight elongation (S1).

6.3. Theory

6.3.1. Vibrational modes of spheroidal particles

Propagating and localized acoustic modes in a medium induce fluctuations of the dielectric constant which can be probed by inelastic scattering of light. Limiting ourselves to the effect of density fluctuations, the contribution of the α-th mode, with frequency ω_α and $\mathbf{u}_\alpha$ displacements, to the scattered field in an one-phonon process was derived earlier.[128]

$$I_\alpha(\mathbf{q}) \propto \frac{n(\omega_\alpha, T) + 1}{\omega_\alpha} P^2 \left| \int_V e^{-\mathrm{i}\mathbf{q}\cdot\mathbf{x}}\, \mathbf{q} \cdot \mathbf{u}_\alpha(\mathbf{x})\, \mathrm{d}\mathbf{x} \right|^2 , \tag{6.1}$$

where $n(\omega_\alpha, T)$ is the Bose-Einstein factor, q is the exchanged wavevector, P is the polarizability density and the integral is over the volume V of the particle.

For spherical free homogeneous particles, the displacement field can be calculated following the theory developed by Lamb, using as parameters the sound velocities c_L and c_T and the size of the particle.[152] Within a continuum model, the normalized vibrational modes, $\mathbf{u}_\alpha$ are labeled by four indices, $\alpha \equiv (p, n, l, m)$. Torsional modes ($p = t$) have pure shear motions, whereas spheroidal modes ($p = s$) involve both shear and stretching. The n, l, m indices label the radial and angular vibrations of spheres in analogy to the atomic orbitals. For any l, we have $2l + 1$ modes whose Brillouin activity depend on the angle between the z-axis and the exchanged wavevector. The total intensity is anyway constant. Given the symmetry of the problem, it is possible to calculate it for an angle equal to zero, where the only active modes are those with cylindrical symmetry ($p = s, m = 0$). This procedure allowed reproducing the details of the particle vibration spectra with high sensitivity to the sound velocities.[127,134,207]

When we consider the light scattering induced from the vibrations of particles with different shapes, (6.1) still holds once we have specified the displacements. Finite elements method (Comsol Multiphysics) was used to illustrate the displacements of two low-order modes for spheroid S2 with $m = 0$ (Fig. 6.3, right panel). The analytically calculated displacement for the two vibrational modes (s,1,2) and (s,1,3) are shown in the left panel of Fig. 6.3 and coincide with the numerical results.

A more precise displacement field of the vibrational modes is needed for the calculation of the Brillouin activity. This was achieved by following the procedure reported by Kang and Leissa, which considers the symmetry of the system.[232] The quantities needed for the calculation are the aspect ratio and the transverse and longitudinal sound velocities. The model has been validated comparing the results with those obtained by an analytical evaluation of the Lamb modes in a sphere. The mode frequencies and patterns show a very high agreement . Up to 7 GHz Brillouin spectra calculated from the two models are practically identical.

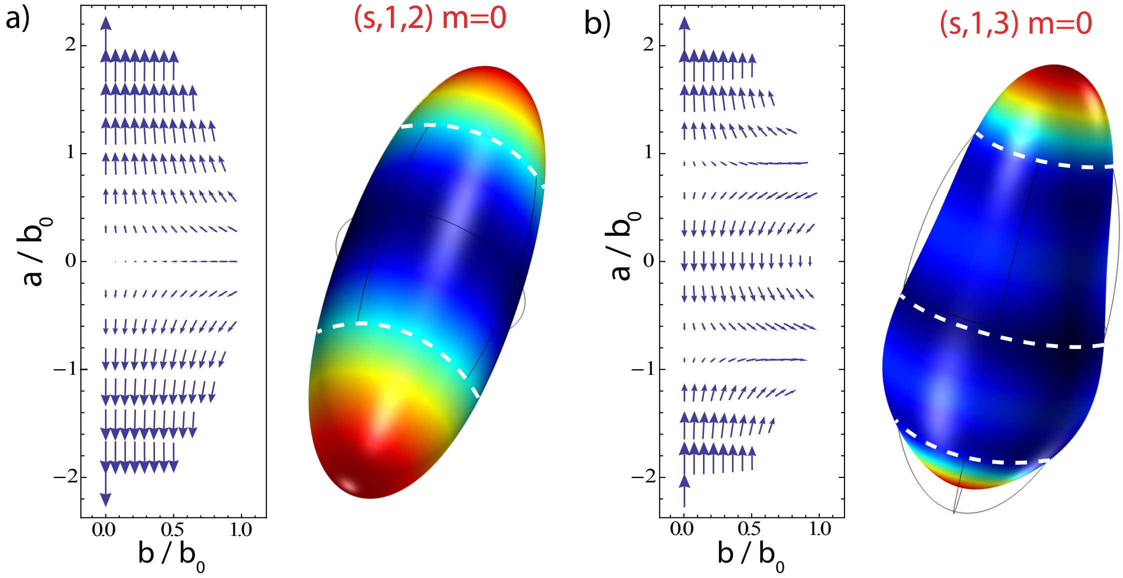

Figure 6.3: Displacement fields of two low frequency modes commonly observed in Brillouin spectroscopy. The depicted aspect ratio corresponds to sample S2, with $a/b = 2.12$. a) First $m = 0$ mode, mainly derived from $(s, 1, 2)$, with two nodal lines (white dashes) and b) second $m = 0$ mode, mainly derived from $(s, 1, 3)$.

Figure 6.4a shows the adimensional frequencies of the first vibrational modes as a function of the aspect ratio for a spheroid with fixed volume and $c_L/c_T = 1.96$. For clarity, only the modes with $m = 0$ are displayed. The blue dashed lines denote the aspect ratio of the particles under study. Figure 6.4b shows the vibrational modes with m ranging from 0 to 3 for the same frequency range, whereas the dashed lines denote purely torsional modes, which are not Brillouin active. The solid vertical line marks the spherical case where the modes are degenerate in m.

While for spherical particles we can assign (p, n, l, m) quantum numbers, as the axis ratio departs from 1 there is important mixing between the various modes of the sphere. For the spheroid vibrations l is no more a good quantum number and only for aspect ratios close to 1 it is possible to identify modes with a dominant l number. In fact, the $(2l+1)$ degeneracy in m of the (n, l) modes is lifted and we can discriminate the modes which correspond to $m = 0, 1, 2, 3\dots$ Modes with opposite m $(n, l, \pm m)$ are still degenerate.

A detailed analysis of the complex behavior of modes dispersion is out of the scope of this work. It is, however, relevant to note that crossing and anticrossing

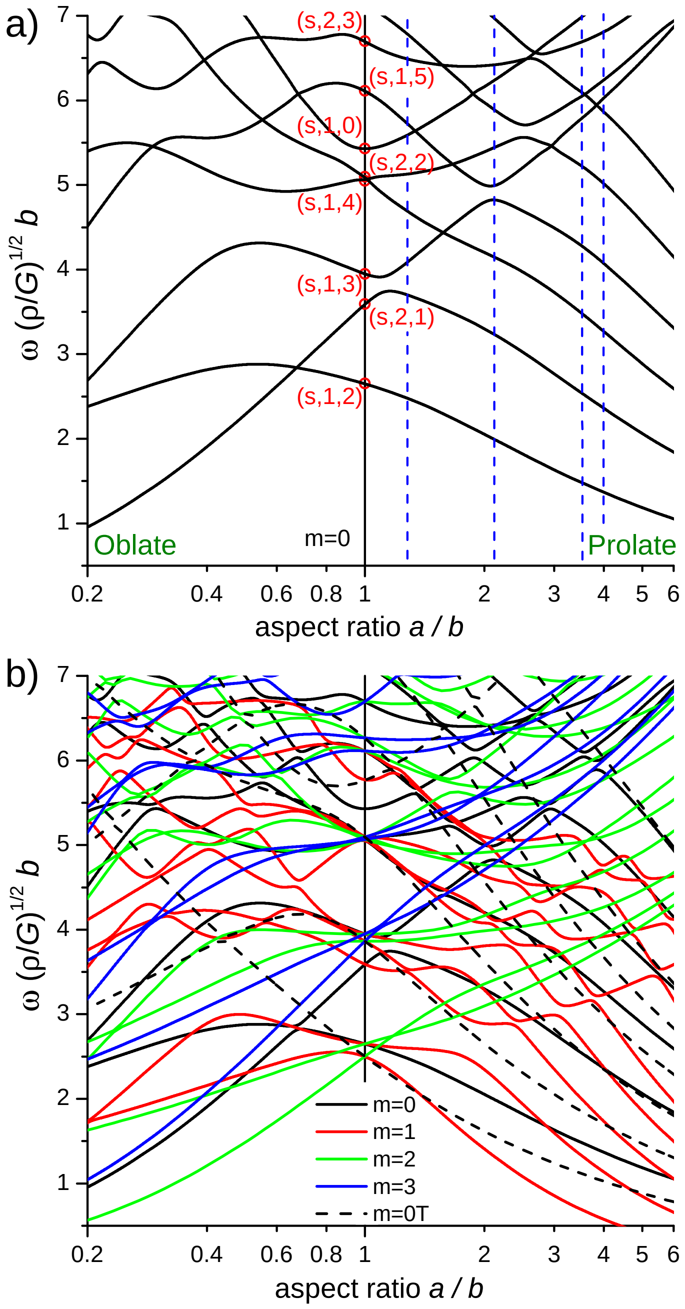

Figure 6.4: a) Adimensional frequency of the first vibrational modes as a function of the aspect ratio displayed for $m = 0$ only, for clarity. G is the shear modulus and ρ the density of the particle. b) Additional bands shown for $m = 0, 1, 2, 3$ as function of the aspect ratio. For $m \neq 0$ no discrimination between torsional and spheroidal modes can be made, as both are active in BLS. Torsional modes (dashed lines) were calculated separately for $m = 0$, being non-active in BLS, as they produce no local dilatation.

between the modes are present. Anticrossings which indicate a strong mixing, show that the spheroid modes have no memory of the symmetry of the sphere modes from which they are derived apart from the m and the parity index. Note in particular that the torsional and spheroidal nature of the modes is not conserved. Only a subset of $m = 0$ modes are in fact torsional (with no local dilatation) and silent in the inelastic light scattering (dashed lines in Fig. 6.4b). All other modes present a stretching component and are active.

With increasing frequency the number of active modes increases (Fig. 6.4b) with concurrent decrease of their life time. These two facts lead to an increasing broadening of the vibration spectra of monodisperse spheroids with frequency. In addition, the inevitable presence of size/shape polydispersity renders the shape of the high frequency spectra featureless (Fig. 6.2a). Thus the low frequency regime of the BLS spectra becomes important for the determination of the thermomechanical properties of spheroidal particles with large aspect ratio. In fact, for rods the only modes are the longitudinal (with displacement along the main axis and constant for any section), the bending (displacement perpendicular) and torsional ones.[194]

6.3.2. Simulation of Brillouin spectra

Having determined the displacement field for the vibrational modes of the spheroid, the Brillouin activity can be calculated by (6.1). For a given mode, it will depend on the exchanged wavevector q and on the angle α between q and the main axis of the spheroid; note that differently from the sphere case, we cannot invoke symmetry in order to reduce ourselves to $\alpha = 0$. The studied samples show a significant turbidity which is the mark of the intense multiple scattering. In these conditions, we cannot consider a single exchanged q or α, even for aligned particles. The intensity has to be averaged on all angles between 0 and $\pi/2$ and all q's between 0 and $4\pi n_{\mathrm{ref}}/\lambda$, where n_{ref} is the refractive index (Tab. 6.1) at the laser wavelength λ (=532 nm).

Operatively, we calculated frequency and displacements of the vibrational modes below 7 GHz of homogeneous spheroids with the aspect ratios of the samples in Table 6.1. The value of the Young's modulus and of the Poisson's ratio (and therefore of the velocity ratio) has been considered constant for all samples (S0–S4) being $E = 4.0\,\mathrm{GPa}$ and $\nu = 0.32$ (corresponding to a velocity ratio $c_{\mathrm{L}}/c_{\mathrm{T}}$ of about 2). However,the values of c_{L} and c_{T} are conceivable to change upon stretching[233] affecting also the density of the particles (Table 6.1). To a first approximation, the velocities scale with $\rho^{-1/2}$. The Brillouin activity was calculated on a grid of q and α values with steps respectively $1/3b$ and $\pi/16$. Discrete integration between 0 and $4\pi n_{\mathrm{ref}}/\lambda$ and between 0 and $\pi/2$ with appropriate weights will produce the scattered intensity by any mode. Note, that for the stretched particles, the refractive index (Table 6.1) was evaluated using Clausius-Mossotti equation and considering that the polarizability of the scattering units has not changed after elongation. For a direct comparison with the experimental spectrum, the discrete calculated spectrum was broadened with Gaussian lineshapes. The latter take into account the experimental linewidth (0.25 GHz), the polydispersity in size ($\sigma_f/f = \sigma_d/d$) and aspect ratio k ($\sigma_f = \partial f/\partial k\, \sigma_k$), with f denoting the vibrational frequency and σ the variance either in f or particle size d. This last source of broadening is very important for the lowest frequency $m = 1$ modes, whose frequency is strongly dependent on the aspect ratio as shown in Fig. 6.4. One effect of line broadening is a shift of the peaks toward lower frequency with respect to the average position calculated for the mean values, as it clearly appears for the low frequency peaks of Fig. 6.2b. It is caused by the $(n(\omega, T) + 1)/\omega$ term of (6.1), which favors particles with larger size and aspect ratio.

Here, we point out that all calculations were performed using no fitting parameters. Furthermore, no anisotropy of elastic properties was regarded along the two axes. Mechanical anisotropy induced by the elongation process would be a conceivable source of broadening.[234] AFM assisted fractal analysis of the surface texture is a conceivable method to identify ordering modification (due to chain elongation) in the stretched particles.[235] However, this method is not applicable when using a sacrificial PVA matrix. Although mild, processing modifies the surface structure with regard to topography, charge and residual PVA.

6.4. Results and Discussion

6.4.1. Lifting of degeneracy in quantum number m

In order to check the accuracy, the simulation procedure was applied to the spherical particles before (untreated) and after (treated) embedding them in PVA. The agreement (Fig. 6.5) is quite good and comparable to earlier results for spheres.[127]

Note, that the fitting of the treated sample (blue line in Fig. 6.5) has been made considering a larger size polydispersity ($\sigma_d/d = 0.06$ vs. 0.035 in the untreated) and a decreased volume (6%), resulting from the removal of the PVA matrix. The vibrational spectrum in particular at low frequencies seems to be very sensitive to size/shape changes even after mild processing conditions.

Clearly, processing is able to modify the particle identity, as monitored by BLS. This change of spectral shape exemplifies the sensitivity to surface fluctuations which is induced by the stretching process. While the shift of frequencies due to size decrease or a mixed PVA/PS surface layer can be attributed to the etching process, the observed broadening has not such a clear attribution. In the fit it has been considered by increasing the size dispersion, but it could also be due to a departure

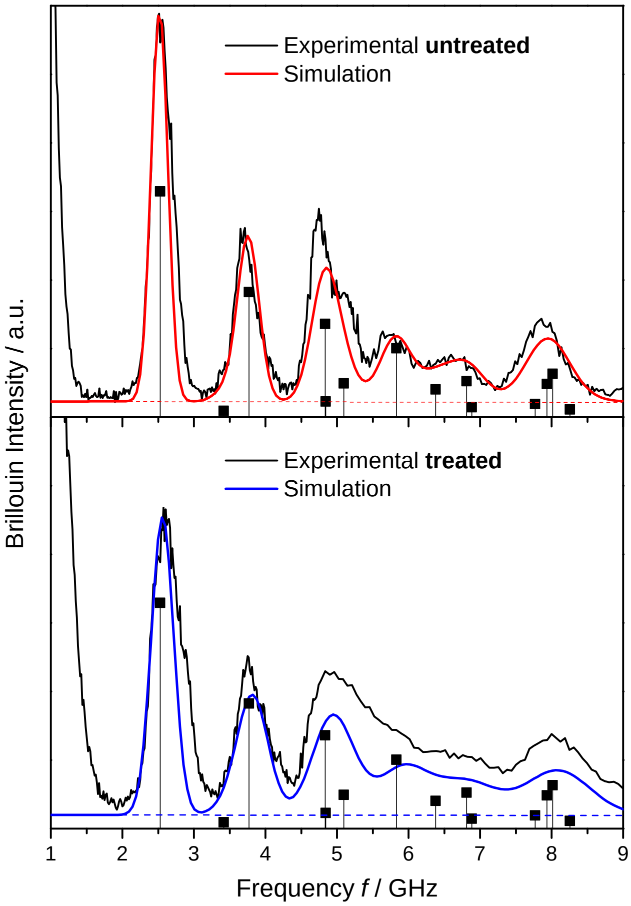

Figure 6.5: Brillouin spectra and simulation of spheres, before (upper panel) and after (lower panel) embedding in the PVA matrix. Recovered particles exhibit reduced volume and larger size dispersion.

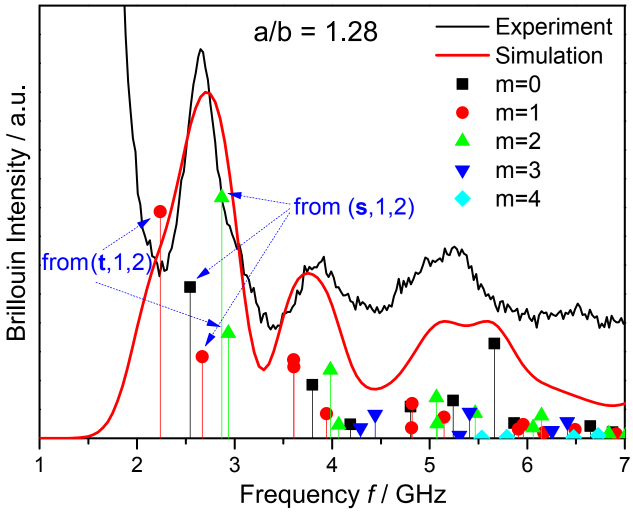

Figure 6.6: Brillouin spectra for relatively low asphericity (a/b=1.28). The shift of spheroidal and torsional lines (blue arrows) cause significant broadening of the low-frequency peak.

from spherical symmetry. Furthermore, it should be noted that a single particle model has been considered neglecting the (possibly increased) interaction between neighboring particles, which causes a line broadening.[134] Finally the particles were considered homogeneous with no density gradient near the surface, a possible result of the mild processing.

As the particle shape departs from spherical symmetry the degeneracy in m is lifted and more modes contribute to the spectrum. This reduced symmetry[118] and to a lesser degree mechanical anisotropy[234] cause the spectral features to be washed out at higher frequency, in addition to size/shape polydispersity. An aspect ratio of 1.28 (Fig. 6.2b) is already large enough that the distinction, found in parent spheres, between torsional and spheroidal modes is no longer valid. Therefore any peak is in fact the sum of several contributions with different m. In Figure 6.6 the first peak at 2.65 GHz can be considered as the sum of the m-splitted (s,1,2) mode of the parent sphere and causes the broadening, even if the contribution from $m = 1$ (red) and $m = 2$ (green) modes derived from the (t,1,2) Lamb mode is not negligible. The situation for the peak at 5 GHz is even more complicated as it consists of many contributions already in the parent sphere. The swapped intensity between the two shoulders (red horizontal lines in Fig. 6.2b) is just a consequence of the manifold shift of lines.

In order to follow this transition trend from homogeneous spheres towards an homogeneous rod, we examined higher aspect ratios. Figure 6.7 (upper panel) displays the superposition of experimental and simulated spectra for sample S2 ($a/b = 2.12$). Peak positions and relative intensity are well represented. Sound velocities larger than that of PS were used to account for the reduced density at constant elastic constants via $M, G = \rho c_{\mathrm{L,T}}^2$. M (G) being the longitudinal (shear) modulus.

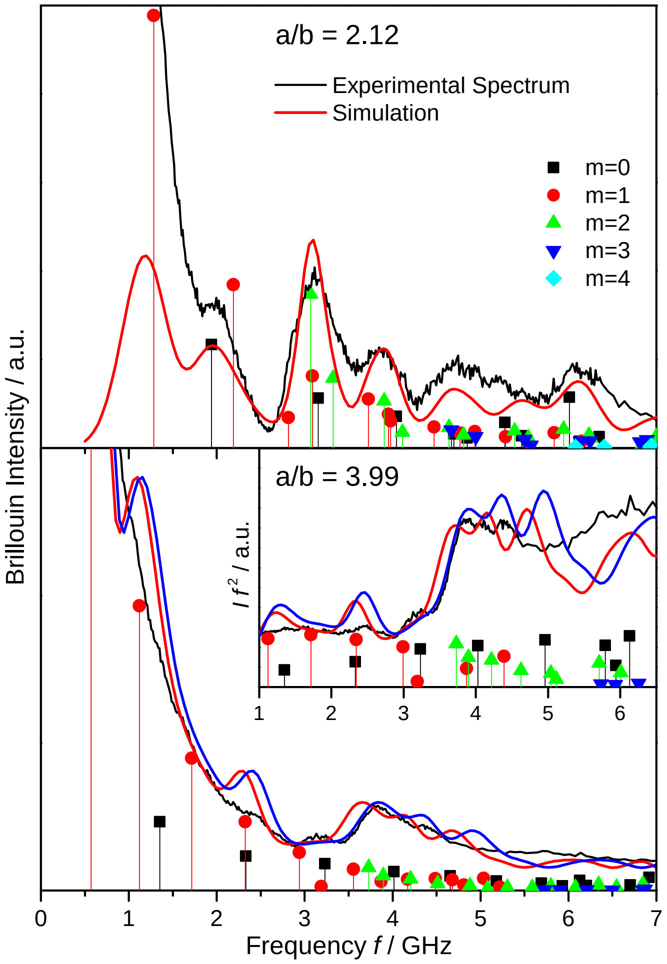

Figure 6.7: Brillouin spectra for spheroids of aspect ratio 2.12 (upper panel) and 3.99 (lower panel). The inset to the lower panel displays the reduced spectrum for S4. Theoretical Brillouin intensity (red lines) as calculated from the sum of the individual contributions $m = 0 \ldots 4$ (modes with $m > 4$ have frequencies higher than 7 GHz). Sources of broadening are the instrumental resolution as well as size and shape dispersion of the spheroids. The blue line in the lower panel gives the simulation with 6% increased sound velocity.

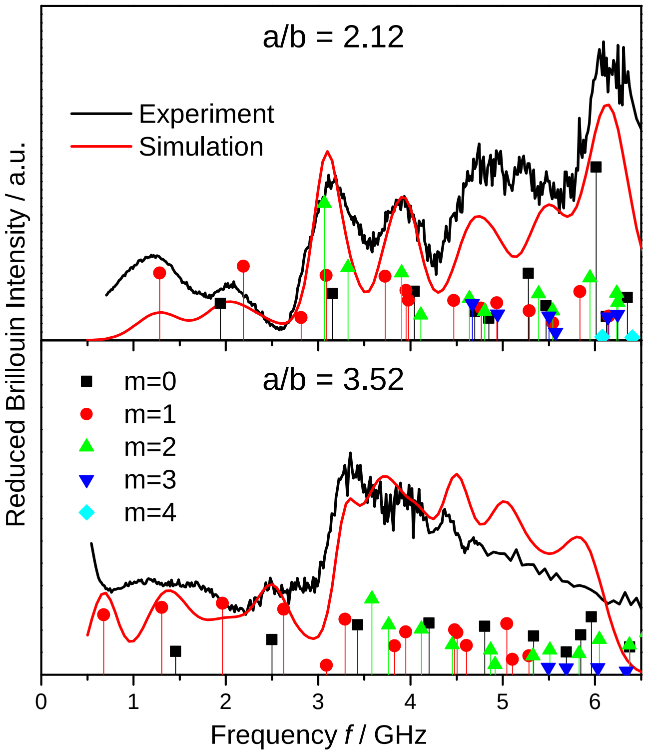

Figure 6.8: Reduced Brillouin spectra ($I\,f^2$) for spheroids of aspect ratio 2.12, and 3.52 reveal the contribution of modes at low frequencies.

At very low frequencies the flanks of the elastic line disturb the inspection of the lower order peaks (e.g., for $m = 1$). In a reduced plot (Fig. 6.8, upper panel) the low-frequency contribution at about 1.3 GHz, which is not observed in Fig. 6.7, is clearly resolved. Due to experimental restrictions (lowest free spectral range and in particular the strong elastic line) frequencies below ~ 1 GHz were not accessible.

6.4.2. Mechanical anisotropy at high aspect ratio

As the aspect ratio is increased (bottom panel of Fig. 6.7) the agreement of simulation and experimental spectra isn't as good as for $a/b = 2.12$. Possibly, the mechanical anisotropy introduced by the stretching process to achieve high aspect ratios cannot be neglected anymore. The modes contributing to the spectrum are too many to be observed individually. The peaks appear much more broadened than those of the upper panel. A broad peak at about 2.5 GHz seams to be reproduced by a couple of nearly resonant modes, the 4th $m = 1$ and the 2th $m = 0$. It better appears in the reduced spectrum (inset to Fig. 6.7), that is obtained by multiplying the experimental spectrum by f^2. The calculated spectrum reproduces well the sharp increase of the intensity occurring at about 3.5 Ghz, which is attributed to several different modes. The representation of the spectrum for $a/b = 3.99$ using sound velocity values adjusted to the density is of moderate quality (red line). Instead, a further increase ($\sim 6\%$) of the sound velocities, while keeping constant their ratio ($c_\mathrm{L}/c_\mathrm{T}$) leads to better agreement with the experimental spectrum (blue line in Fig. 6.7) as without any adjustable parameter (red line). This hardening in stretched polymers has been reported before[236] and reflects the mechanical anisotropy caused by the stretching process. Only for the particles with the largest aspect ratio, the moduli increase by about 12% compared to the spherical parent particles. For the particles with lower aspect ratio, it is noteworthy mentioning the insensitivity of the average moduli and hence the Poisson's ratio to the stretching of the PS spheres. This preserved mechanical strength is an unprecedented information from the particle vibrational spectra.

6.5. Conclusions

This work presents the capability of a computational method combined with Brillouin spectroscopy as an effective tool for the characterization of the elastic properties of elongated spheres. Notwithstanding the significant approximation involved, we were able to reproduce reasonably well the experimental spectra of spheroidal particles. However, a few obstacles are faced with respect to the results for the spherical particles: i) the m-splitting of the modes, which multiplies any sphere (n, l) mode into $l + 1$ ones at different frequency; and ii) the polydispersity of the samples (size and aspect ratio). The mixed effect of increasing the number of active modes and of the polydispersity induced broadening leads to practically featureless spectra for frequencies higher than ~ 7 GHz (Fig. 6.2a). In any case the apparent peaks in the Brillouin spectra are indeed the sum of many different contributions (e.g., the peak at ~ 4 GHz in the spectrum of sample S4 is the sum of 7 peaks of comparable intensity).

From the good theoretical representation of the experimental vibration spectra, all four but the highest aspect ratio spheroidal PS particles preserve the same orientation averaged elastic constants with the seed spheres while the density (sound velocity) decreased (increased) with asphericity. The highest aspect ratio ($a/b \sim 4$) spheroids possess elastic moduli increased by 12%. As an outlook, the low frequency vibrational spectrum can be also utilized to assess the thermomechanical properties and determine the glass transition temperature of these spheroids through a temperature dependent study and establish the analogy to the spherical particles.[134]

This knowledge can be used for the study of phononic properties of an ordered assembly. The opening of hybridization gaps requires strong localization of elastic energy in the building units.[41] It becomes even more important, as energy leakage is allowed when the local resonator is placed in a liquid to assure optical matching.[43] For spheroids, mostly the rather well separated vibrational states in the low-frequency regime will play a major role for anticrossing interaction with the acoustic branch, i.e. opening of hybridization gaps. Colloidal crystals with spheroidal building blocks will exhibit inherently anisotropic mechanical and optical properties. Hence, thermal conductivity as well as transmission of light and sound will be a function of the orientation relative to the asymmetric particles.

7. Phononic Band Gaps in Anisotropic Colloidal Crystals

A colloidal crystal with anisotropic acoustic properties and a unidirectional hypersonic band gap is fabricated using AC electric field-directed convective self-assembly of elongated spheroids. The opening of a band gap most likely originates from hybridization of the primary eigenmode peak, the m-split (s,1,2) particle vibration mode and the effective medium phonons. The frequency of the gap and the effective sound velocities can be tuned by the particle aspect ratio. These results reveal large potential for enhanced control of the phononic band diagram using a combination of anisotropic particles and their ability of self-assembly.

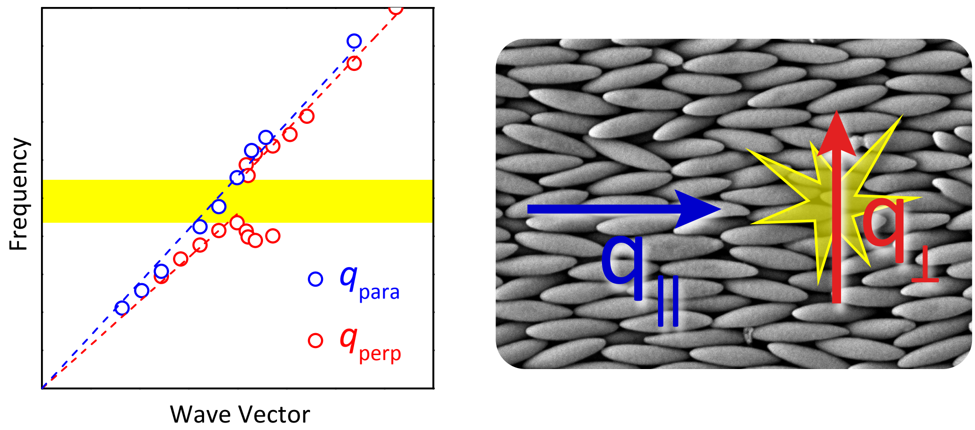

This Chapter is based on:
P. J. Beltramo, D. Schneider, P. Pfleiderer, J. Vermant, G. Fytas and E. M. Furst
Anisotropic hypersonic phonons in films of aligned colloidal spheroids. unpublished.

7.1. Introduction

The ever-expanding library of colloidal building blocks allows for the potential fabrication of complex structured, functional materials that react to and guide sound, energy, light and/or chemical species via directed self-assembly techniques.[215–217] However, creating structures with long range order from nonspherical building blocks remains a challenge. In particular, the realization of theoretically predicted close-packed phases of anisotropic particles[227,228,237,238] is frustrated by slowing translational and rotational dynamics[239,240] and high nucleation barriers,[241] leading to jammed or glassy random structures.[241,242] Overcoming these barriers to ordered assemblies with directed self-assembly techniques is important because periodicity in microstructures can be exploited to control the transport of phonons, photons, charge and/or molecular species.

Extensive work has been done examining the propagation of phonons through colloidal crystals assembled from spherical building blocks. Such materials exhibit a Bragg-type bandgap whose frequency and width can be tuned by sphere diameter and infiltrated fluids.[40] An additional bandgap at lower frequencies, termed a hybridization gap, has also been found in similar crystals.[41,181] This hybridization gap forms from level repulsion between the acoustic branch and a localized resonant mode within particle, and as a result persists upon the loss of structural order in the sample. The width of these gaps depends on the contrast of density, longitudinal (c_L) and transverse (c_T) sound velocities of the particles and infiltrating liquid. For submicron colloids the gaps occur in the GHz frequency range which is readily probed by Brillouin light scattering (BLS). These materials (and analogs with smaller length scales) are of particular interest for heat management applications since the thermal conductivity in dielectric materials partially relies on phononic transport of energy in this frequency regime.[161] Here, the probed frequency range (few GHz) covers only the lower range of the heat carrying phonons that exhibit a wide spread in the sub-THz range. Previous BLS studies have characterized the eigenmode spectra of spheres[127,134,177] and their resulting phononic band diagram.[40,41,43] Only recently, the vibrational spectra of particles with more complex shapes has been identified[135,243] while the phononic band diagram of ordered arrays of such particles has not previously been examined.

This Chapter presents the phononic band diagram of aligned films of polystyrene (PS) spheroids. The films are fabricated by AC field-directed convective self-assembly and subsequently infiltrated with poly(dimethylsiloxane) (PDMS) for BLS measurement. We find that the preferential particle alignment with the directing field leads to unprecedented anisotropy in the mechanical properties of a colloidal thin film, and a unidirectional band gap is observed perpendicular to the axis of orientation. This demonstrates how self-assembly of colloidal materials from anisotropic particles allows for additional control over the flow of sound (or heat) in novel materials.

7.2. Experimental

7.2.1. Film preparation

We have fabricated spheroids of three aspect ratios (a/b = 2.12, 3.52 and 3.99) by mechanical stretching of 400 nm diameter carboxylate modified PS spheres (cat. #C37238, Invitrogen, Eugene, OR). The details of the stretching procedure are described elsewhere.[124,125] Briefly, seed particles were dispersed in an aqueous poly(vinyl alcohol) (PVA) solution, spread in a thin layer and allowed to dry into a thin film after water evaporation. The film was then heated above the polystyrene glass transition temperature (145 °C) in an oil bath and stretched to a given strain to produce the three aspect ratio particles. The processed film was cut into small sections and cleaned from silicon oil by fivefold washing with isopropyl alcohol (IPA). The particles were recovered by dissolution in water/IPA 7:3 (v/v) and the suspensions are observed to be stable. These were repeatably washed via centrifugation-decantation-resuspension, first in the water/IPA and then in 0.1 mM KCl to remove any contaminants. The size of the spheroids was characterized by scanning electron microscopy (SEM) and a summary of the particle dimensions is given in Table 7.1. The suspensions were concentrated to a volume fraction $\phi \approx 0.15$ before being introduced to the AC electric field assembly cell.

To align the particles into orientationally ordered thin films, we made use of an AC electric field-directed convective assembly technique. The assembly cell consists of coplanar gold electrodes on a glass slide with a 1.5−2 mm electrode gap. A thin sample chamber is created by spreading UV glue with ten micron diameter glass beads on top of the electrodes, carefully placing a coverslip on top and curing

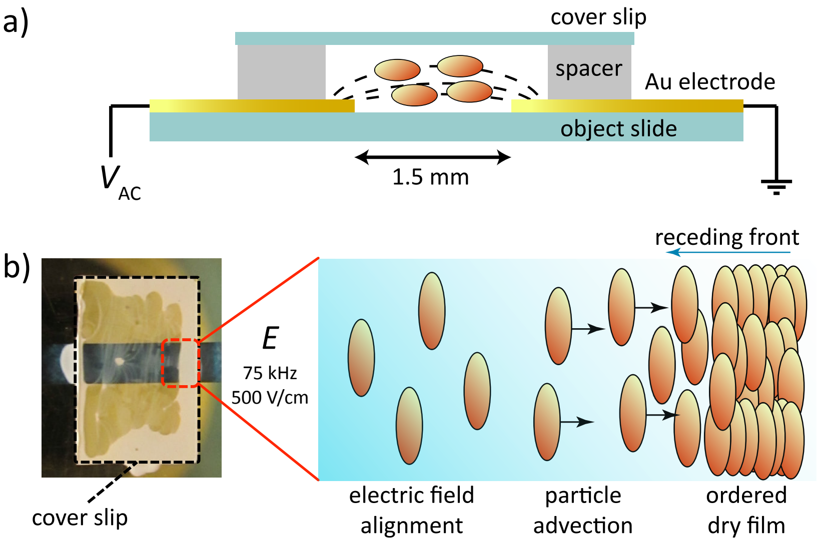

Figure 7.1: a) Schematic side view of the AC field-directed assembly cell b) Schematic of the ordered film formation process near the edges of the assembly cell.

(Fig. 7.1a). The cell was placed on a temperature controlled stage at 22 °C before loading 3–5 µL of suspension by capillary forces at the open ends. Then, an AC electric field of 75 kHz and 500–700 V/cm was applied. The edges of the cell were left open, allowing the particles to align in suspension as a result of the applied field, advect towards the drying front at the edge of the cell, and dry into an orientationally ordered thin film (Fig. 7.1b).

SEM images of the resulting film show the orientational order persists throughout the ~20 µm film thickness (Fig. 7.2). Analysis of top-view SEM images of films fabricated with all three aspect ratios show that greater than 90% of the particles are aligned within ±30° of the electric field direction in every case (Fig. 7.3). Initially

Table 7.1: Size characterization of particles studied and material parameters used in calculations.

a/b	a / nm	b / nm	ρ / kg-m^{-3}
1	400±14	–	1050
2.12±0.16	690±42	325±15	921.9^{a}
3.52±0.20	986±15	280±15	869.4^{a}
3.99±0.22	1078±93	270±23	854.7^{a}

^{a} calculated based on stretched particle volume.

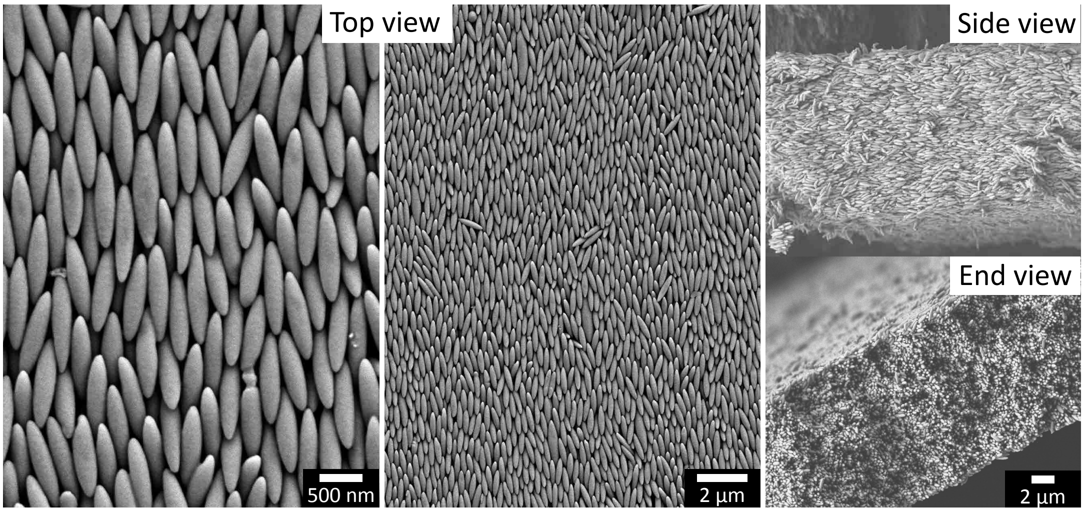

Figure 7.2: Scanning electron microscopy (SEM) images of the top, side and end view of the resulting aligned film for $a/b = 3.99$.

field-aligning anisotropic particles in a more dilute suspension before concentrating the particles with convective deposition avoids jamming; this successful assembly path has also been used to crystallize slightly anisotropic magnetic ellipsoids,[220] align titania ellipsoids[223] and crystallize PS dicolloids.[241] After the drying process is complete, the top coverslip is carefully removed, keeping the film intact and allowing infiltration with PDMS (M_w = 770 Da) for BLS measurement. The sample is rotated in the holder to measure thermal phonon propagation both parallel ($\|$) and perpendicular ($\perp$) to the particle alignment.

7.2.2. Brillouin light scattering

High-resolution BLS measurements of the ordered films were performed using a six-pass tandem Fabry-Perot interferometer in conjunction with $\lambda = 532\,\text{nm}$ Nd/YAG laser mounted on a goniometer, allowing for q-dependent experiments. Thermally excited phonons cause inelastic scattering of the incident laser light due to elasto-optic coupling. The scattering vector $\mathbf{q} = \mathbf{k}_s - \mathbf{k}_i$ specifies the direction of propagation thas is probed. Here $\mathbf{k}_i$ and $\mathbf{k}_s$ refer to the incident and scattered photon wave-vector, respectively. The desired dispersion relations are obtained by recording the phonon frequencies as a function of scattering wave-vector $\mathbf{q}$. The BLS spectrum

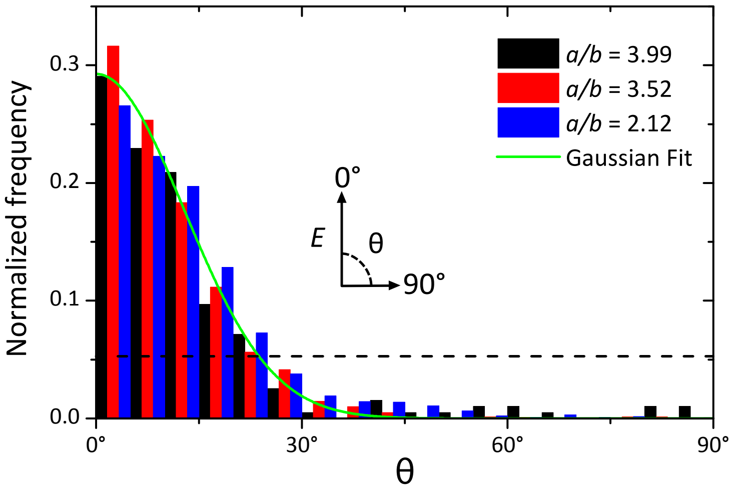

Figure 7.3: Histogram showing the degree of particle alignment with the electric field estimated from top view SEM images. The green line denotes a Gaussian fit to the data of the highest aspect ratio. The dashed horizontal line represents an isotropic distribution.

consists of doublets centered around the elastic frequency with $f = \pm c_\mathrm{L} q/2\pi$, where c_L is the sound velocity for homogeneous (over the probed length scale) films. BLS spectra were obtained over a wide range of angles, $\theta = 20°–120°$, corresponding to a q-range of $q = 0.0041–0.0205\,\mathrm{nm}^{-1}$. The free spectral range was varied between 6, 7.5 and 10 GHz depending on the scattering angle to achieve optimal resolution of the phonon peaks. For turbid samples, multiple scattering causes loss of the well-defined q-vector. Therefore the films were infiltrated with PDMS to reduce elastic scattering of light by (almost) matching the refractive index of the particle with the index of the surrounding liquid. However, the turbity enabled the measurement of q-independent resonance modes of the individual spheroids (Chapter 6). The resolved modes are an unique fingerprint of the particles' shape and elastic properties, hence are invaluable for the understanding of the anisotropic mechanical properties of the aligned films.[135] The particle vibration spectra of opaque isotropic and aligned colloidal films were checked and are expectedly consistent (Fig. 7.4). The BLS measurements of infiltrated, index matched films allow access to the q-dependent acoustic modes along the desired propagation direction, i.e. along or perpendicular to the long axis a.

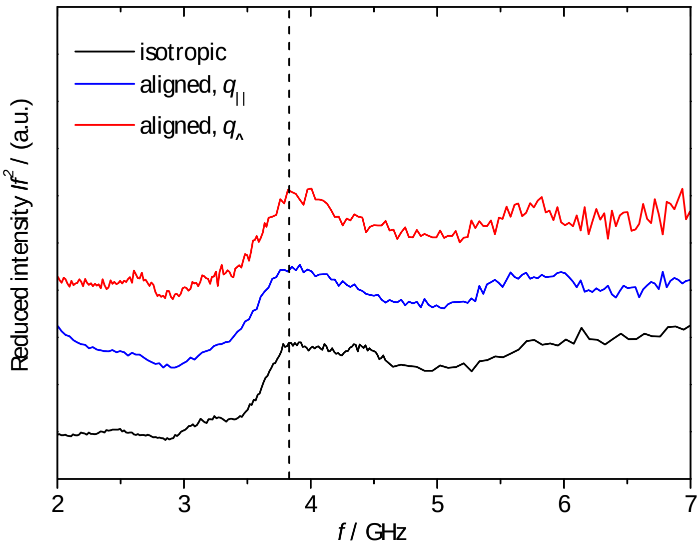

Figure 7.4: The reduced eigenmode spectra for aligned, non-infiltrated, particles of aspect ratio $a/b = 3.99$ are independent of film morphology and scattering geometry. Minor variances are likely due to the length of measurement time and thickness of the sample, the isotropic (drop cast) film is significantly thicker and was measured for a longer time; as a result the peaks are resolved in greater detail.

7.3. Results and Discussion

Prior to measurements of elastic moduli of elongated PS spheres, we have checked the phononic dispersion of the seed spheres, as shown in Fig. 7.5. The presence of a Bragg gap and hybridization gap is evident and has already been described for slightly smaller PS particles, in 2008.[41] For this film the longitudinal sound velocity $c_\mathrm{L} = 1460\,\mathrm{ms}^{-1}$ was extracted from the single acoustic (non-bending) phonon branch at low q-values, which reflects an effective medium of PDMS ($c_\mathrm{L} = 1050\,\mathrm{ms}^{-1}$) and PS ($c_\mathrm{L} = 2350\,\mathrm{ms}^{-1}$).[41]

7.3.1. Anisotropy of phonon dispersion

The BLS spectra for aligned films of aspect ratios $a/b = 2.12$, 3.52 and 3.99 at several q-values are given in Fig. 7.6. For clarity, only the anti-Stokes side of the symmetric BLS spectra is shown. At low q-values, the system appears homogeneous and a single Lorentzian peak is seen. As q is increased, the peak width increases and a double peak feature is observed in some cases. This splitting marks the edges of a

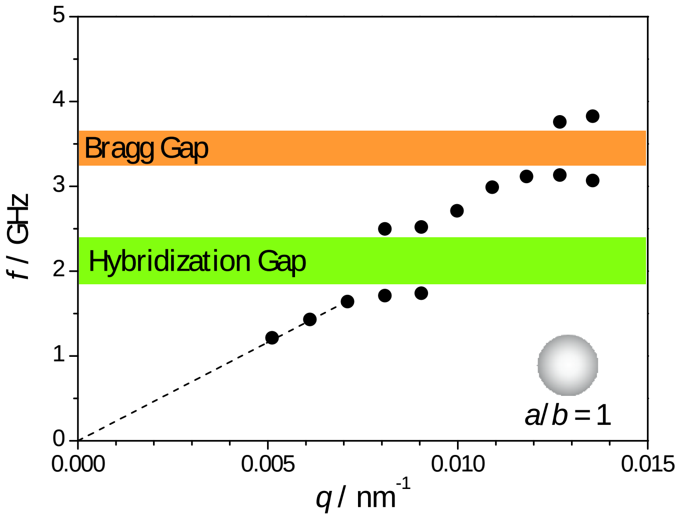

Figure 7.5: Phononic band diagram for the assembled PS sphere seed particles. Two phononic band gaps are observed: a hybridization gap (green) and a Bragg gap (orange).

frequency gap and occurs at a distinct q most likely due to hybridization between the acoustic branch and a flat mode stemming from a particle resonance. The difference in the spectra as a result of propagation direction is obvious, with peaks occurring at higher frequencies for the $q_{||}$ than the $q_{\perp}$ direction at a given scattering angle.

In Fig. 7.7 the complete dispersion relations of the three films are shown, that exhibit several noteworthy features. First, as expected from Fig. 7.6, the frequency of the acoustic peaks varies with propagation direction over the entire q-range covered. In the direction parallel to the particle alignment, the $f(q_{||})$ is relatively linear over the entire range, resulting in a large effective longitudinal sound velocity of 1753 ms^{-1} (1899; 1584 ms^{-1}) for the $a/b = 2.12$ (3.52; 3.99) spheroid films, compared to spheres or perpendicular propagation. At low q-values in the direction perpendicular to the particle alignment, $f(q_{\perp})$ is also linear with a significantly lower effective sound velocity of 1441 ms^{-1} (1535; 1453 ms^{-1}), for the respective films. It is worth pointing out that these spectra were obtained from the same aligned films, only the sample was rotated in plane to probe either propagation direction. This leads us to the first major finding: films of aligned spheroids indeed exhibit anisotropic acoustic properties. Furthermore, the degree of stretching dictates the effective sound velocity mainly in the parallel direction, while staying relatively constant (and equal to the seed spheres) in the perpendicular direction. A possible scenario for this mechanical

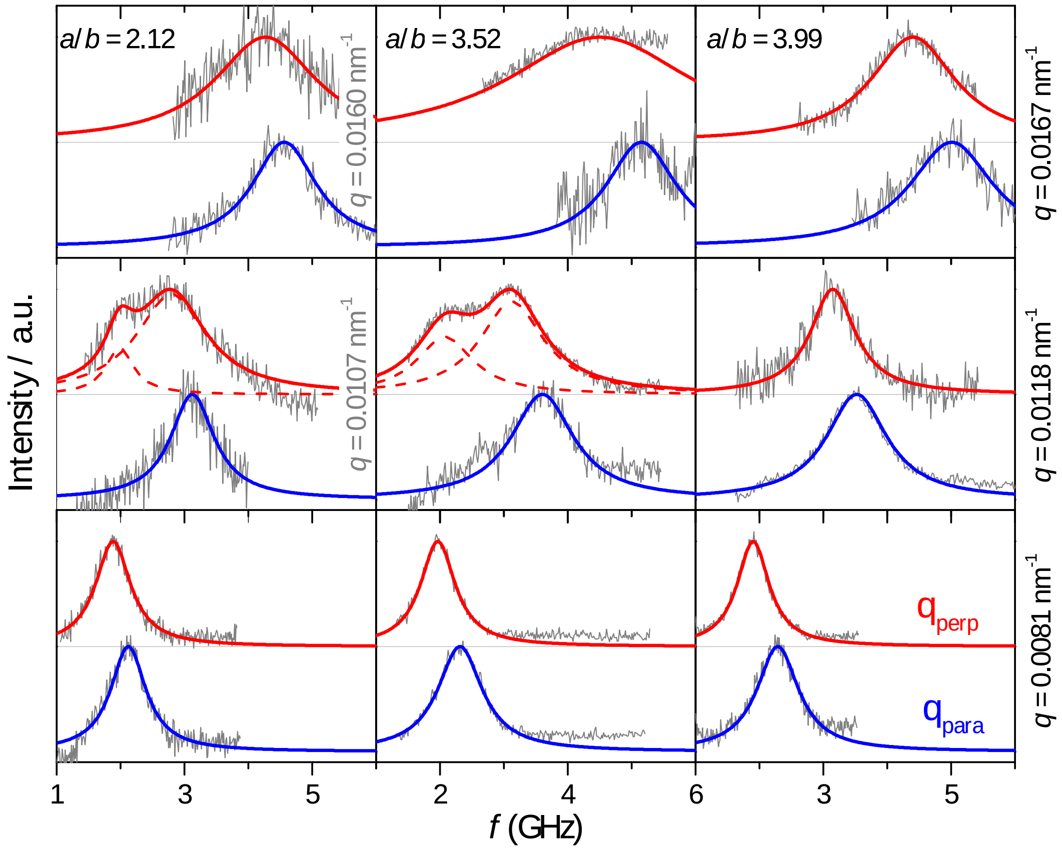

Figure 7.6: Selected BLS spectra of the infiltrated aligned films with aspect ratio and $a/b = 2.12$ (left), $a/b = 3.52$ (middle) and $a/b = 3.99$ (right) as function of scattering vector q (increasing from bottom to top). The blue (red) lines denote a Lorentzian fit of the experimental spectra for sound propagation parallel (perpendicular) to the long-axis. Note, in the left panel the higher q-values slightly deviate from those in the other panels.

anisotropy is the increased number of PS/PDMS grain boundaries in the perpendicular versus parallel direction, which consequently is subject to augmented phonon scattering. A more likely explanation is the unidirectional stretching procedure that causes different elastic moduli of PS inside the particle, depending on the direction. Of course, the effective sound velocity will be also a function of the particle packing fraction. All films were fabricated by the same method, and estimation of the packing fraction from SEM images leads to a consistent $\phi \approx 0.7$ across all films. This value is slightly less than the maximum theoretical packing of $\phi = 0.77$ for ellipsoidal particles[227,228] and notably higher than for spheres (random close packing $\phi \sim 0.64$).

7.3.2. Unidirectional hybridization gaps

The second striking feature is the presence of a unidirectional band gap, centered at q-values of 0.0095 and 0.0113 nm^{-1} for the low and high aspect ratio films (Table 7.2). Here, the peak in the BLS spectra splits and the slope of the dispersion $f(q_\perp)$ is steeper above the band gap (Fig. 7.7). This behavior suggests the existence of a hybridization gap (HG), arising from anti-crossing interaction of the effective medium phonon with low-f particles resonances. Note that this gap is completely absent in the parallel direction, where the slope of $f(q_\parallel)$ is constant and the material exhibits homogenous, effective medium-like properties over the entire q-range. A previous study of the eigenmode spectra of the same particles revealed the $(s, 1, 2)$ mode of the seed spheres splitting into multiple modes as the symmetry of the particle is lost (Chapter 6).[135] In particular, the $m = 0$ mode shifts to lower frequencies while the $m = 2$ mode moves to higher frequencies. It is this latter mode that gives the strongest contribution to the BLS eigenmode spectra (cf. Fig. 6.2b) and has the same frequency dependence across different aspect ratios as the observed HG. Finite element method (FEM) calculations of the displacement revealed this mode essentially as a "pinching" of the short axis of the spheroid (Fig. 7.8b). Since the perpendicular direction is measuring propagation across the short axis,

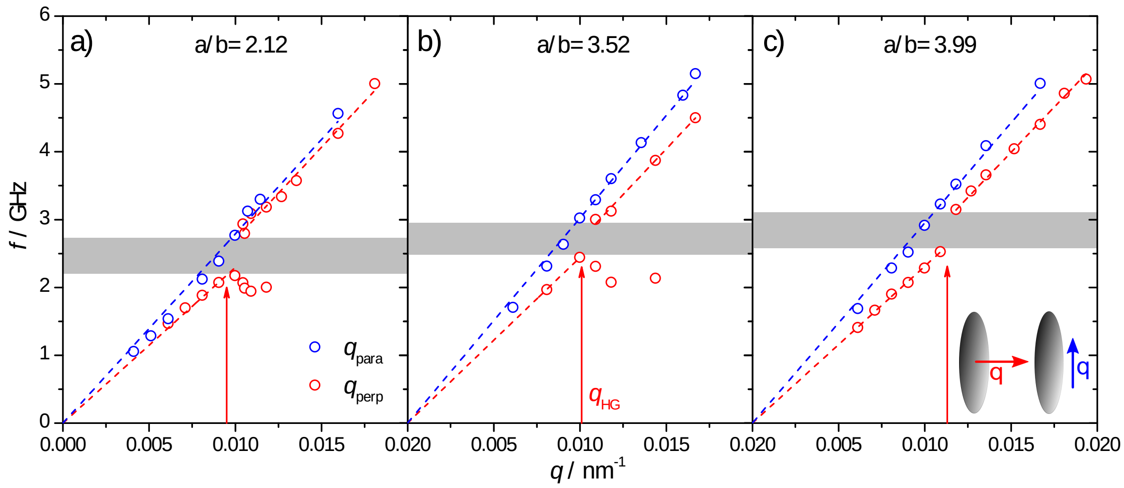

Figure 7.7: Dispersion relations for phonon propagation along the long (blue) and short axis (red) of aligned spheroid films with aspect ratio $a/b = 2.12$ (a) 3.52 (b) and 3.99 (c). A band gap is only observed in the $q_\perp$ direction (grey shading).

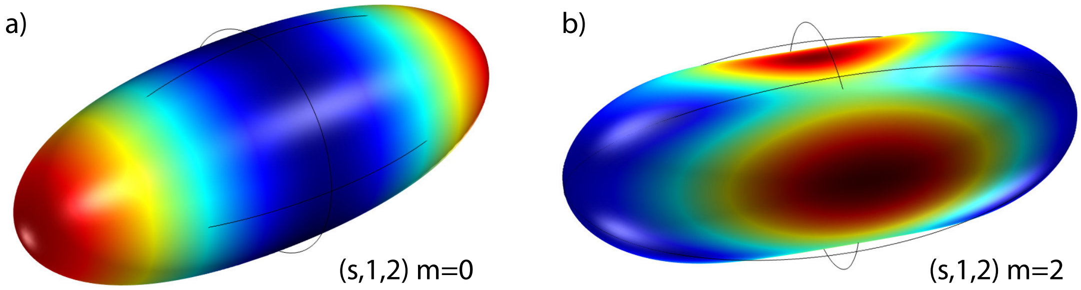

Figure 7.8: Displacement field of two principal modes calculated by the finite elements method. The generacy of the fundamental spheroidal mode (s,1,2,m) is lifted in m, hence the displacement along a) the long ($m = 0$) and b) short axis ($m = 2$) is clearly distinguished.

the hybridization of this vibrational state with the propagating acoustic phonon should occur merely along this direction. FEM calculations of the $m = 0$ $(s, 1, 2)$ mode reveal that its deformation is a stretching of the particle along the long axis (Fig. 7.8a). This mode exhibits weaker intensity and shows up at lower frequencies due to the longer a-axis (which corresponds to a lower q). Therefore, observation of a HG in the $q_{\|}$-direction is unlikely given the size of the particles and instrumental limitations (too low frequency).

A complete summary of the results for the $a/b = 1$, 2.12, 3.52 and 3.99 aligned films is given in Table 7.2. The results for the 2.12 particle films are of particular interest. The effective sound velocity found in the $q_{\perp}$ direction above the hybridiza-

Table 7.2: Sound velocities, band gap location and eigenfrequencies of aligned spheroids.

a/b	$c_{\mathrm{L},\|}$ / ms^{-1}	$c^*_{\mathrm{L},\perp}$ / ms^{-1}	$c_{\mathrm{L},\|}/c_{\mathrm{L},\perp}$	q_{HG} / nm^{-1}	f_{HG} / GHz	f(s,1,2) / GHz
1	n/a	1460	1	0.0076	2.13	2.57
2.12	1753±85	1441±59 1703±46	1.22	0.0095	2.50	3.10
3.52	1899±46	1535±05 1693±23	1.24	0.0101	2.89	3.58
3.99	1854±53	1453±16 1672±20	1.28	0.0113	2.85	3.79

*For sound propagation perpendicular to the long axis two velocities are given for frequencies below and above the band gap, respectively.

tion gap is close to that in the $q_{\|}$ direction. Hence, phonons with these frequencies propagate isotropically with the same speed of sound, while at lower phonon frequencies the propagation is retarded along a specific direction. This increased sound velocity above the gap is a direct consequence of the opening of a band gap that shifts the upper bands to higher frequencies.

However, for an exact analysis of stretched colloidal crystals complete band structure calculations are needed. Although the films presented here are well aligned (Fig. 7.2), they hardly form structures of sufficient cristallinity to apply Bloch's theorem. This makes a Bragg interference a very unlike origin of the gap. Furthermore, the decreased lattice parameter along the short axis (upon stretching) should result in a Bragg gap located at even higher frequency; here the opposite is observed. The favored hybridization gap is further underpinned by a consistent increase of the q_{HG}-values (Table 7.2) with aspect ratio, that clearly remain below $q_{\mathrm{BG}} = 0.012\,\mathrm{nm}^{-1}$ of the sphere (Fig. 7.5). The q-shift of the HG is intimately connected with the increase of the aspect ratio as proven by $q_{\mathrm{HG}}/q^{\circ}_{\mathrm{HG}} \approx b^{\circ}/b$ ($\circ$ denoting the respective quantity of the sphere). Therefore we have to turn our attention to the vibrations of

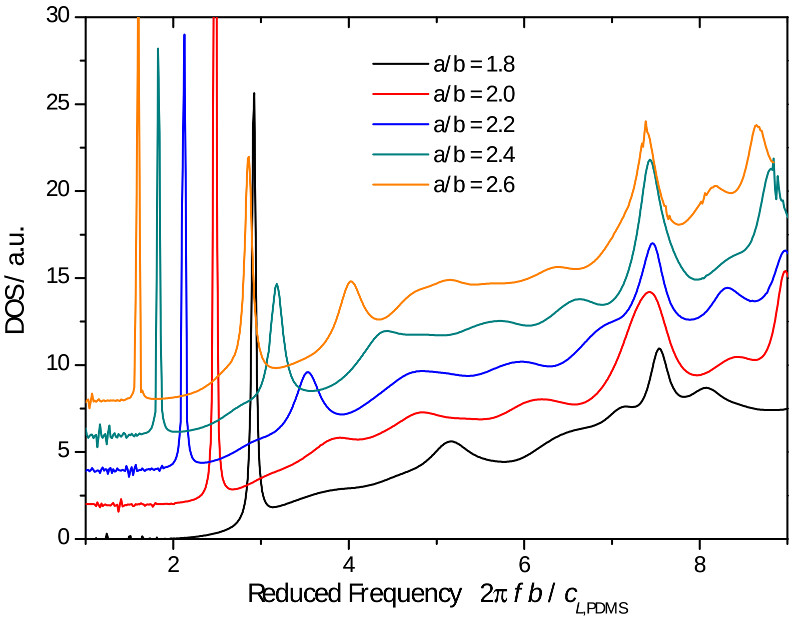

Figure 7.9: Vibrational DOS for particles of different aspect ratio (vertical offset for clarity). A reduced frequency $f^{*} = 2\pi f b / c_{L,\mathrm{PDMS}}$ is used to eliminate the absolute particle size and the properties of the matrix. (provided by N. Papanikolaou and N. Stefanou)

the individual particles. While the eigenmodes of dry colloids are easily measured (Fig. 6.2a), the vibrational density of states (DOS) of infiltrated spheroids has to be calculated to account for the different elastic properties of the matrix.[41] Fig. 7.9 displays the DOS as function of reduced frequency and various aspect ratios. Due to symmetry decomposition in m (Chapter 6) the DOS consists of many contributions. The most striking is a well-localized (narrow) mode at low frequencies that strongly varies with aspect ratio and its frequency falls well below the band gap (for the $a/b = 2.12$ film at 1.1 GHz). In contrast, the mode at $f^* = 7.5$ is relatively robust to stretching and corresponds to 3.6 GHz, i.e. slightly above the band gap (f_{HG}=3.1 GHz). The theoretical results were derived for an isolated particle in PDMS, disregarding any multiple scattering of phonons that could further affect the dispersion relation. However, these semiquantitative findings already represent a localized mode that scales with aspect ratio and probably evokes the formation of a HG. The correct values will be given by fine adjustment of the elastic parameters, which might be necessary to account for the mechanical anisotropy caused by the stretching procedure. Therefore the computational elucidation of the mechanical anisotropy is further pursued.

Although the particles have excellent orientational order, they are not arranged on a periodic crystal lattice, which prevents the observation of a Bragg gap in the spheroid films. Refined self-assembly techniques that achieve such robust control over translational order could lead to new functional materials. These make the simultaneous realization of anisotropic Bragg gaps (tunable by the dimensions of the building blocks) and unidirectional hybridization gaps (tunable by aspect ratio and packing fraction) conceivable.

7.4. Conclusions

In conclusion, we have shown how AC field-directed self-assembly can be used to fabricate a material with fascinating acoustic properties. Due to shape anisotropy in the spheroidal building blocks, acoustic phonons propagate with different velocity depending on alignment with respect to the directing field. For the first time, a unidirectional hybridization gap is observed. The nature of this gap has to be further supported by theoretical calculations. Soft matter colloids provide unique building blocks to study the phonon-matter interactions in mechanically anisotropic materials. As self-assembly techniques are applied to non-spherical particles, the creation of increasingly complex ordered structures may lead to further refinement and control over the phononic band structure and thus the propagation of heat/sound in nanostructures.

Part IV.

Epilog

8. Final Remarks

8.1. Conclusions

The thesis yields insight to current research on hypersonic wave propagation in mesoscopic composite structures. Access to the micromechanical properties of artificially designed systems is provided by a combination of inelastic light scattering and theoretical calculations. High-resolution Brillouin spectroscopy is employed to probe elastic excitations at GHz frequencies, enabling the study of the phononic dispersion relation in multilayered thin films (superlattices) and local resonant modes in colloidal particles. As the elucidation of full vector-wave propagation in 3D structures is quite demanding, the problem is approached by initially limiting ourselves to the one-dimensional case.

Structures with periodicity along a single direction are suitable model systems for fundamental studies of elastic wave propagation. Herein, we proposed the use of hybrid superlattices composed of alternately spincoated layers of hard SiO_2 and soft PMMA using conventional soft matter fabrication techniques. First, the opening of Bragg gaps along the direction of periodicity was reported for normal incidence, i.e. for an elastic wave traversing a SL perpendicular to the layers. Concurrent theoretical representation of the phonon dispersion and amplitudes of the modes provided reliable determination of the longitudinal moduli of the respective materials. The characteristics of the band gap (width, central position and the intensity of the edge modes) were all adequately described by theory. The impact of fabrication-related film imperfections on measured Brillouin spectra was examined by modeling a disordered structure, having a surprisingly robust dispersion as result. Transverse moduli were accessed via oblique incidence experiments, exploiting the vector nature of the elastic wave propagation. The resulting mode mixing of longitudinal acoustic waves with in-plane sagittal modes can be immediately seen from the dispersion relation as a function of obliqueness. The complete description of these hybrid SL laid the foundation for a subsequent study on defect-designed SLs.

Next, we demonstrated the sensitivity of the band diagram by introduction of defect layers. After various other works have described the indication of surface modes,[105,107,175] we reported the first unequivocal evidence for the existence and interaction of surface and cavity modes in finite SLs.[132] The findings open pathways for dynamic tuning of cavity modes and mode interaction under external stimuli, such as phase transformation induced by thermo- or chemiresponsive layers). The fact that hypersonic phononic crystals also act as phononic crystals, makes them interesting candidates for concurrent modulation of light and sound. These new dual photonic-phononic structures are often referred to as “phoxonic crystals” and might play a pivotal role in future tunable optomechanic devices.

For the colloid-based phononics, eigenmodes play a vital role in the dispersion diagram. Dry non-transparent films of mesoscopic colloids yield the spectrum of vibrational eigenmodes, which sensitively index the geometrical and thermomechanical characteristics of the respective particles. Therefore, this particle vibration spectroscopy can be considered the elastic analog of the molecular vibrational spectroscopy (FT-IR, Raman). We found the BLS spectra of relatively large particles to be well represented by theory based on a freely vibrating sphere,[127] but the line shapes of small particles were shown to be significantly different from the simple theory. To account for the effects of interactions being important for smaller spheres, we considered a fcc colloidal crystal in which adjacent spheres are connected by springs. Modes that have zero frequency in a single sphere can become dispersive bands if the interaction among the particles (given by the effective spring constant) is increased.[134] Thus, a broad band at low frequencies was attributed to the $(s, 1, 1)$ mode which is purely translational, hence only seen in clusters of particles. These findings were qualitatively validated by annealing of colloidal films near the glass transition temperature. Besides the determination of nanomechanical properties, we gained novel insights into the adhesion of colloids, which will enable the characterization of different types of interactions.

The utility of particle vibration spectroscopy has been used to characterize the elastic properties of non-spherical particles. Although a few approximations had to be used, the experimental spectra of spheroidal particles (elongated PS spheres) were well reproduced. The most striking feature was the practically featureless spectrum at higher frequencies and large aspect ratios. Apart from the increased size dispersion due to the stretching process, this “washing-out” of peaks mainly arises from the lifting of degeneracy in the quantum number m. The m-splitting of the principal $(s,1,2)$ mode was confirmed by investigating particles of small asphericity.

Successful theoretical representation of moderately stretched spheres was entirely based on the change in shape. Young's modulus was held constant by assuming an increased sound velocity to account for the decreased density.

These spheroids were used as building blocks to form aligned colloidal crystals with anisotropic mechanical properties. An immediate evidence for mechanical anisotropy is given by the acoustic phonons traveling with a fast or slow pace parallel or perpendicular to the aligned assembly, respectively. Strong localization of elastic energy in the particles can lead to the opening of hybridization gaps or distorted phonon dispersion diagrams.[41,43] The spheroids presented here, have well separated vibrational states at low frequencies that can contribute to such a gap opening. This work demonstrates for the first time, that a unidirectional hybridization gap can show up in mechanically anisotropic aligned colloidal crystals, despite the considerable degree of disorder. While the theoretical representation of the gap nature is still in progress, preliminary calculations based on the hybridization mechanism are already intriguing. More elaborate self-assembly techniques hold the potential to create increasingly complex ordered structures.

8.2. Outlook

When concluding on this thesis' work, it becomes obvious that future work is needed to further advance the fundamental research and potential applications of phononic systems. As mentioned above, the design of dual gap (phoxonic) structures[167] for manipulation of both, photons (in the visible) and (hypersonic) phonons is a promising expansion of this work with convincing perspectives towards applications in optomechanics and acoustic MEMS. Hypersonic phononics with wavelengths similar to that of visible light hold an important place in the spectrum of elastic waves. At the high-frequency edge, the THz regime will be entered which is the realm of thermal phonons and vibronic transitions. On the low-frequency side we find the ultrasonic and sonic regime with numerous applications in our daily life. A number of efforts were already reported[51,162,244] that aim to manipulate elastic waves in a given frequency range with either much larger or much smaller structures. Here, the buzzword is optical/acoustic metamaterials that involve negative refractive index (optics) or negative effective mass (acoustics). These materials have fascinating abilities for unconventional interactions with electro-magnetic or elastic waves manifested, e.g., in the design of acoustic cloaks or superlenses.

An interesting development is the reach of polymer and colloid sciences towards fields, thus far dominated by condensed matter physics. This work demonstrated the utility of soft matter fabrication to be able to compete with classical semiconductor fabrication techniques with regard to tunability and ease of fabrication. Although, there is still a way to go when it comes to the accuracy and other inherent limitations of soft matter, basic concepts like phonon folding and gap formation have been realized using hybrid superlattices. During the course of this thesis, first experiments on lamellar 1D structures with periodicity along the sample plane were performed (so called *nanoridges*). Here, the use of laser interference lithography grants the production of high-quality periodic structures with sub-wavelength dimensions.[168] Regarding system complexity polymer science becomes the link between biological tissue engineering and solid state research. Nanocomposites composed of an organic component and an inorganic such as clay, silica or calcite are very interesting with regard to biomimetic devices.[245] Of particular technological importance are the strong backbones (the spicules) of deep sea sponges[246] and corals or the dragline of spider webs.[247,248] BLS measurements on these transparent materials have high potential, since the (high) elastic moduli are readily and non-destructively probed.

So far, only thermal phonons were probed by selecting a well-defined q-vector and observing the associated phonons. The next step is to excite phonons of a specific frequency above the thermal equilibrium, either by electrostriction or heat pulses arising from absorbed GHz-pulsed lasers. Such stimulated hypersound experiments will provide deeper insight to phonon propagation and dissipation in soft nanostructures, and open perspectives towards advanced heat management.

Bibliography

[1] C. Huygens, *Traité de la lumière* (chez Pierre vander Aa, 1690).

[2] I. Newton, Philosophical Transactions **6**, 3075 (1671).

[3] T. Young, Philosophical Transactions of the Royal Society of London **94** (1804).

[4] J. C. Maxwell, Philosophical Transactions of the Royal Society of London **155**, 459 (1865).

[5] H. Hertz, Annalen der Physik **7**, 421 (1887).

[6] M. Planck, Verhandlungen der Deutschen physikalischen Gesellschaft **2**, 235 (1900).

[7] A. Einstein, Ann. Phys. **322**, 132 (1905), ISSN 1521-3889.

[8] J. Mehra and H. Rechenberg, *The historical development of quantum theory* (Springer-Verlag, 2001).

[9] G. N. Lewis, Nature **118**, 874 (1926).

[10] J. I. Frenkel, *Wave Mechanics. Elementary Theory.* (Clarendon Press, Oxford, 1932).

[11] L. de Broglie, Ph.D. thesis, Sorbonne University of Paris (1924).

[12] C. Davisson and L. H. Germer, Nature **119**, 558 (1927).

[13] M. Arndt, O. Nairz, J. Vos-Andreae, C. Keller, G. van der Zouw, and A. Zeilinger, Nature **401**, 680 (1999), ISSN 0028-0836.

[14] E. Rutherford, Philosophical Magazine Series 6 **21**, 669 (1911), ISSN 1941-5982.

[15] W. Gerlach and O. Stern, **9**, 349 (1922), ISSN 0044-3328.

[16] W. Gerlach and O. Stern, **9**, 353 (1922), ISSN 0044-3328.

[17] W. Friedrich, P. Knipping, and M. Laue, Ann. Phys. **41**, 971 (1913).

[18] C. V. Raman, Indian Journal of Physics **2**, 387 (1928).

[19] W. Jacobi, *Halbleiterverstärker* (1949), dE833366 (C), June 8th, 1949.

[20] E. Yablonovitch, Phys. Rev. Lett. **58**, 2059 (1987).

[21] S. John, Phys. Rev. Lett. **58**, 2486 (1987).

[22] J. D. Joannopoulos, S. G. Johnson, J. N. Winn, and R. D. Meade, *Photonic Crystals - Molding the Flow of Light* (Princeton University Press, 2008).

[23] A. A. Zakhidov, R. H. Baughman, Z. Iqbal, C. Cui, I. Khayrullin, S. O. Dantas, J. Marti, and V. G. Ralchenko, Science **282**, 897 (1998).

[24] S. Y. Lin, J. G. Fleming, D. L. Hetherington, B. K. Smith, R. Biswas, K. M. Ho, M. M. Sigalas, W. Zubrzycki, S. R. Kurtz, and J. Bur, Nature **394**, 251 (1998), ISSN 0028-0836.

[25] D. M. Whittaker, Opt. Lett. **25**, 779 (2000).

[26] S.-Y. Lin, E. Chow, V. Hietala, P. R. Villeneuve, and J. D. Joannopoulos, Science **282**, 274 (1998).

[27] D. Ripin, K.-Y. Lim, G. Petrich, P. R. Villeneuve, S. Fan, E. Thoen, J. D. Joannopoulos, E. Ippen, and L. Kolodziejski, Lightwave Technology, Journal of **17**, 2152 (1999), ISSN 0733-8724.

[28] R. F. Cregan, B. J. Mangan, J. C. Knight, T. A. Birks, P. S. J. Russell, P. J. Roberts, and D. C. Allan, Science **285**, 1537 (1999).

[29] C. M. Smith, N. Venkataraman, M. T. Gallagher, D. Muller, J. A. West, N. F. Borrelli, D. C. Allan, and K. W. Koch, Nature **424**, 657 (2003), ISSN 0028-0836.

[30] Y. S. Chan, C. T. Chan, and Z. Y. Liu, Phys. Rev. Lett. **80**, 956 (1998).

[31] J.-H. Lee, J. P. Singer, and E. L. Thomas, Advanced Materials **24**, 4782 (2012), ISSN 1521-4095.

[32] M. S. Kushwaha, P. Halevi, L. Dobrzynski, and B. Djafari-Rouhani, Phys. Rev. Lett. **71**, 2022 (1993).

[33] M. Sigalas and E. N. Economou, Solid State Communications **86**, 141 (1993), ISSN 0038-1098.

[34] R. Martinez-Salazar, J. Sancho, J. V. Sanchez, V. Gomez, J. Llinares, and F. Meseguer, Nature **378**, 241 (1995).

[35] F. R. Montero de Espinosa, E. Jiménez, and M. Torres, Phys. Rev. Lett. **80**, 1208 (1998).

[36] Z. Liu, X. Zhang, Y. Mao, Y. Y. Zhu, Z. Yang, C. T. Chan, and P. Sheng, Science **289**, 1734 (2000).

[37] J. O. Vasseur, P. A. Deymier, B. Chenni, B. Djafari-Rouhani, L. Dobrzynski, and D. Prevost, Phys. Rev. Lett. **86**, 3012 (2001).

[38] R. S. Penciu, H. Kriegs, G. Petekidis, G. Fytas, and E. N. Economou, The Journal of Chemical Physics **118**, 5224 (2003).

[39] T. Gorishnyy, C. K. Ullal, M. Maldovan, G. Fytas, and E. L. Thomas, Phys. Rev. Lett. **94**, 115501 (2005).

[40] W. Cheng, J. Wang, U. Jonas, G. Fytas, and N. Stefanou, Nat. Mater. **5**, 830 (2006), ISSN 1476-1122.

[41] T. Still, W. Cheng, M. Retsch, R. Sainidou, J. Wang, U. Jonas, N. Stefanou, and G. Fytas, Phys. Rev. Lett. **100**, 194301 (2008).

[42] M. L. Cowan, J. H. Page, and P. Sheng, Phys. Rev. B **84**, 094305 (2011).

[43] T. Still, G. Gantzounis, D. Kiefer, G. Hellmann, R. Sainidou, G. Fytas, and N. Stefanou, Phys. Rev. Lett. **106**, 175505 (2011).

[44] A. Shaulov, W. Smith, and B. M. Singer, in *IEEE 1984 Ultrasonics Symposium* (1984), pp. 545–548.

[45] S. Yang, J. H. Page, Z. Liu, M. L. Cowan, C. T. Chan, and P. Sheng, Phys. Rev. Lett. **88**, 104301 (2002).

[46] K. M. Kinnunen, M. R. J. Palosaari, and I. J. Maasilta, Journal of Applied Physics **112**, 034515 (2012).

[47] B. Graczykowski, S. Mielcarek, A. Trzaskowska, J. Sarkar, P. Hakonen, and B. Mroz, Phys. Rev. B **86**, 085426 (2012).

[48] V. G. Veselago, Sov. Phys. Usp. **10**, 509 (1968).

[49] L. Fok, M. Ambati, and X. Zhang, MRS Bull. **33**, 931 (2008).

[50] J. Page, Nat. Mater. **10**, 565 (2011), ISSN 1476-1122.

[51] Y. Lai, Y. Wu, P. Sheng, and Z.-Q. Zhang, Nat. Mater. **10**, 620 (2011), ISSN 1476-1122.

[52] S. Yang, J. H. Page, Z. Liu, M. L. Cowan, C. T. Chan, and P. Sheng, Phys. Rev. Lett. **93**, 024301 (2004).

[53] A. Sukhovich, L. Jing, and J. H. Page, Phys. Rev. B **77**, 014301 (2008).

[54] S. A. Cummer and D. Schurig, New Journal of Physics **9**, 45 (2007), ISSN 1367-2630.

[55] L. Sanchis, V. M. García-Chocano, R. Llopis-Pontiveros, A. Climente, J. Martínez-Pastor, F. Cervera, and J. Sánchez-Dehesa, Phys. Rev. Lett. **110**, 124301 (2013).

[56] R. H. Olsson III and I. El-Kady, Measurement Science and Technology **20**, 012002 (2009).

[57] M. Eichenfield, J. Chan, R. M. Camacho, K. J. Vahala, and O. Painter, Nature **462**, 78 (2009), ISSN 0028-0836.

[58] M. Maldovan and E. L. Thomas, Applied Physics Letters **88**, 251907 (2006).

[59] S. Sadat-Saleh, S. Benchabane, F. I. Baida, M.-P. Bernal, and V. Laude, Journal of Applied Physics **106**, 074912 (2009).

[60] N. Papanikolaou, I. E. Psarobas, and N. Stefanou, Applied Physics Letters **96**, 231917 (2010).

[61] P. Lacharmoise, A. Fainstein, B. Jusserand, and V. Thierry-Mieg, Applied Physics Letters **84**, 3274 (2004).

[62] N. Papanikolaou, I. Psarobas, N. Stefanou, B. Djafari-Rouhani, B. Bonello, and V. Laude, Microelectronic Engineering **90**, 155 (2012), ISSN 0167-9317.

[63] A. Fainstein, N. D. Lanzillotti-Kimura, B. Jusserand, and B. Perrin, Phys. Rev. Lett. **110**, 037403 (2013).

[64] A. D. O'Connell, M. Hofheinz, M. Ansmann, R. C. Bialczak, M. Lenander, E. Lucero, M. Neeley, D. Sank, H. Wang, M. Weides, et al., Nature **464**, 697 (2010), ISSN 0028-0836.

[65] J. Chan, T. P. M. Alegre, A. H. Safavi-Naeini, J. T. Hill, A. Krause, S. Groblacher, M. Aspelmeyer, and O. Painter, Nature **478**, 89 (2011), ISSN 0028-0836.

[66] G. Bahl, M. Tomes, F. Marquardt, and T. Carmon, Nat. Phys. **8**, 203 (2012), ISSN 1745-2473.

[67] D. C. Jiles, Journal of Physics D: Applied Physics **28**, 1537 (1995).

[68] A. J. Kent, R. N. Kini, N. M. Stanton, M. Henini, B. A. Glavin, V. A. Kochelap, and T. L. Linnik, Phys. Rev. Lett. **96**, 215504 (2006).

[69] R. P. Beardsley, A. V. Akimov, M. Henini, and A. J. Kent, Phys. Rev. Lett. **104**, 085501 (2010).

[70] M. I. Ojovan, Entropy **10**, 334 (2008), ISSN 1099-4300.

[71] M. S. Paterson, Journal of Applied Physics **35**, 176 (1964).

[72] Y. Mi, G. Xue, and X. Wang, Polymer **43**, 6701 (2002), ISSN 0032-3861.

[73] W. Cheng, R. Sainidou, P. Burgardt, N. Stefanou, A. Kiyanova, M. Efremov, G. Fytas, and P. F. Nealey, Macromolecules **40**, 7283 (2007), 0024-9297.

[74] K. L. Kearns, T. Still, G. Fytas, and M. D. Ediger, Advanced Materials **22**, 39 (2010).

[75] Y. Guo, A. Morozov, D. Schneider, J. W. Chung, C. Zhang, M. Waldmann, N. Yao, G. Fytas, C. B. Arnold, and R. D. Priestley, Nat. Mater. **11**, 337 (2012), ISSN 1476-1122.

[76] M. D. Ediger and L. Yu, Nat. Mater. **11**, 267 (2012), ISSN 1476-1122.

[77] S. Singh, M. D. Ediger, and J. J. de Pablo, Nat. Mater. **12**, 139 (2013), ISSN 1476-1122.

[78] D. G. Cahill and R. O. Pohl, Phys. Rev. B **35**, 4067 (1987).

[79] R. M. Costescu, D. G. Cahill, F. H. Fabreguette, Z. A. Sechrist, and S. M. George, Science **303**, 989 (2004).

[80] C. Chiritescu, D. G. Cahill, N. Nguyen, D. Johnson, A. Bodapati, P. Keblinski, and P. Zschack, Science **315**, 351 (2007).

[81] G. Pernot, M. Stoffel, I. Savic, F. Pezzoli, P. Chen, G. Savelli, A. Jacquot, J. Schumann, U. Denker, I. Mönch, et al., Nat. Mater. **9**, 491 (2010), ISSN 1476-1122.

[82] G. Floquet, Annales de l'École Normale Supérieure **12**, 47 (1883).

[83] F. Bloch, **52**, 555 (1928), ISSN 0044-3328.

[84] E. Schrödinger, Annalen der Physik (Leipzig) **79**, 384 (1926).

[85] R. de L. Kronig and W. G. Penney, Proceedings of the Royal Society of London. Series A **130**, 499 (1931).

[86] S. M. Rytov, Sov. Phys. Acoust. **2**, 68 (1956).

[87] W. a. Maurice Ewing, *Elastic waves in layered media* (McGraw Hill, 1957).

[88] M. C. Comerio, Science **312**, 204 (2006).

[89] G. Sai-Halasz, A. Pinczuk, P. Yu, and L. Esaki, Solid State Communications **25**, 381 (1978), ISSN 0038-1098.

[90] V. Narayanamurti, H. L. Störmer, M. A. Chin, A. C. Gossard, and W. Wiegmann, Phys. Rev. Lett. **43**, 2012 (1979).

[91] C. Colvard, R. Merlin, M. V. Klein, and A. C. Gossard, Phys. Rev. Lett. **45**, 298 (1980).

[92] P. X. Zhang, D. J. Lockwood, H. J. Labbé, and J.-M. Baribeau, Phys. Rev. B **46**, 9881 (1992).

[93] N. D. Lanzillotti Kimura, A. Fainstein, and B. Jusserand, Phys. Rev. B **71**, 041305 (2005).

[94] N. D. Lanzillotti-Kimura, A. Fainstein, A. Huynh, B. Perrin, B. Jusserand, A. Miard, and A. Lemaître, Phys. Rev. Lett. **99**, 217405 (2007).

[95] N. Gomopoulos, D. Maschke, C. Y. Koh, E. L. Thomas, W. Tremel, H. J. Butt, and G. Fytas, Nano Letters **10**, 980 (2010), doi: 10.1021/nl903959r.

[96] D. Schneider, F. Liaqat, E. H. El Boudouti, Y. El Hassouani, B. Djafari-Rouhani, W. Tremel, H.-J. Butt, and G. Fytas, Nano Letters **12**, 3101 (2012).

[97] L. M. Goldenberg, V. Lisinetskii, and S. Schrader, Laser Physics Letters **10**, 055808 (2013), ISSN 1612-202X.

[98] L. C. Parsons and G. T. Andrews, Applied Physics Letters **95**, 241909 (2009), ISSN 00036951.

[99] G. N. Aliev, B. Goller, D. Kovalev, and P. A. Snow, Appl. Phys. Lett. **96**, 124101 (2010), ISSN 00036951.

[100] G. Saini, T. Pezeril, D. Torchinsky, J. Yoon, S. Kooi, E. Thomas, and K. Nelson, Journal of Materials Research **22**, 719 (2007).

[101] P. M. Walker, J. S. Sharp, A. V. Akimov, and A. J. Kent, Appl. Phys. Lett. **97**, 073106 (2010).

[102] H. T. Grahn, H. J. Maris, J. Tauc, and B. Abeles, Phys. Rev. B **38**, 6066 (1988).

[103] H. J. Trodahl, P. V. Santos, G. V. M. Williams, and A. Bittar, Phys. Rev. B **40**, 8577 (1989).

[104] V. Lemos, O. Pilla, M. Montagna, and C. de Souza, Superlattices and Microstructures **17**, 51 (1995), ISSN 0749-6036.

[105] N.-W. Pu and J. Bokor, Phys. Rev. Lett. **91**, 076101 (2003).

[106] G. P. Schwartz, G. J. Gualtieri, and W. A. Sunder, Applied Physics Letters **58**, 971 (1991), ISSN 00036951.

[107] M. Trigo, T. A. Eckhause, M. Reason, R. S. Goldman, and R. Merlin, Phys. Rev. Lett. **97**, 124301 (2006).

[108] Y. Ezzahri, S. Grauby, J. M. Rampnoux, H. Michel, G. Pernot, W. Claeys, S. Dilhaire, C. Rossignol, G. Zeng, and A. Shakouri, Phys. Rev. B **75**, 195309 (2007).

[109] L. Belliard, A. Huynh, B. Perrin, A. Michel, G. Abadias, and C. Jaouen, Phys. Rev. B **80**, 155424 (2009).

[110] M. N. Luckyanova, J. Garg, K. Esfarjani, A. Jandl, M. T. Bulsara, A. J. Schmidt, A. J. Minnich, S. Chen, M. S. Dresselhaus, Z. Ren, et al., Science **338**, 936 (2012).

[111] M. Trigo, A. Bruchhausen, A. Fainstein, B. Jusserand, and V. Thierry-Mieg, Phys. Rev. Lett. **89**, 227402 (2002).

[112] S. Roshan Entezar and A. Namdar, Phys. Rev. A **80**, 013814 (2009).

[113] B. Liang, X. S. Guo, J. Tu, D. Zhang, and J. C. Cheng, Nat. Mater. **9**, 989 (2010), ISSN 1476-1122.

[114] S.-M. Lee, D. G. Cahill, and R. Venkatasubramanian, Applied Physics Letters **70**, 2957 (1997).

[115] Y. K. Koh, Y. Cao, D. G. Cahill, and D. Jena, Adv. Funct. Mater. **19**, 610 (2009), ISSN 1616-3028.

[116] M. Hu, X. Wang, G. V. Hartland, P. Mulvaney, J. P. Juste, and J. E. Sader, J. Am. Chem. Soc. **125**, 14925 (2003), ISSN 0002-7863.

[117] H. Petrova, C.-H. Lin, S. de Liejer, M. Hu, J. M. McLellan, A. R. Siekkinen, B. J. Wiley, M. Marquez, Y. Xia, J. E. Sader, et al., The Journal of Chemical Physics **126**, 094709 (2007).

[118] B. Stephanidis, S. Adichtchev, S. Etienne, S. Migot, E. Duval, and A. Mermet, Phys. Rev. B **76**, 121404 (2007).

[119] C. Herrmann, M. B. Bannwarth, K. Landfester, and D. Crespy, Macromol. Chem. Phys. **213**, 829 (2012), ISSN 1521-3935.

[120] J. Y. Sun, Z. K. Wang, H. S. Lim, S. C. Ng, M. H. Kuok, T. T. Tran, and X. Lu, ACS Nano **4**, 7692 (2010).

[121] T. Still, R. Sainidou, M. Retsch, U. Jonas, P. Spahn, G. P. Hellmann, and G. Fytas, Nano Letters **8**, 3194 (2008).

[122] M. D'Acunzi, L. Mammen, M. Singh, X. Deng, M. Roth, G. K. Auernhammer, H.-J. Butt, and D. Vollmer, Faraday Discuss. **146**, 35 (2010).

[123] C. Krueger and U. Jonas, Journal of Colloid and Interface Science **252**, 331 (2002).

[124] C. Ho, A. Keller, J. A. Odell, and R. H. Ottewill, Colloid Polym. Sci. **271**, 469 (1993).

[125] K. M. Keville, E. I. Franses, and J. Caruthers, J. Colloid Interface Sci. **144**, 103 (1991).

[126] M. Retsch, Ph.D. thesis, Johannes Gutenberg-Universität Mainz (2009).

[127] T. Still, M. Mattarelli, D. Kiefer, G. Fytas, and M. Montagna, The Journal of Physical Chemistry Letters **1**, 2440 (2010).

[128] M. Montagna, Phys. Rev. B **77**, 045418 (2008).

[129] Y. Li, H. S. Lim, S. C. Ng, Z. K. Wang, M. H. Kuok, E. Vekris, V. Kitaev, F. C. Peiris, and G. A. Ozin, Applied Physics Letters **88**, 023112 (2006).

[130] J.-H. Jang, C. K. Ullal, T. Gorishnyy, V. V. Tsukruk, and E. L. Thomas, Nano Letters **6**, 740 (2006).

[131] W. Cheng, Ph.D. thesis, Johannes Gutenberg-Universität Mainz (2007).

[132] D. Schneider, F. Liaqat, E. H. El Boudouti, O. El Abouti, W. Tremel, H.-J. Butt, B. Djafari-Rouhani, and G. Fytas, Phys. Rev. Lett. **111**, 164301 (2013).

[133] H. H. Pan, Z. K. Wang, H. S. Lim, S. C. Ng, V. L. Zhang, M. H. Kuok, T. T. Tran, and X. M. Lu, Applied Physics Letters **98**, 133123 (2011).

[134] M. Mattarelli, M. Montagna, T. Still, D. Schneider, and G. Fytas, Soft Matter **8**, 4235 (2012), ISSN 1744-683X.

[135] D. Schneider, P. J. Beltramo, M. Mattarelli, P. Pfleiderer, J. Vermant, D. Crespy, M. Montagna, E. M. Furst, and G. Fytas, Soft Matter **9**, 9129 (2013).

[136] L. D. Landau and E. M. Lifshitz, *Theory of Elasticity* (Pergamon Press, 1986), 3rd ed.

[137] A. L. Cauchy, *Oeuvres Complètes* (Cambridge University Press, 2009), vol. 2 of *2*, chap. Recherches sur l'équilibre et le mouvement intérieur des corps solides ou fluides, élastiques ou non élastiques., pp. 300–304.

[138] A. L. Cauchy, Exercices de Mathématiques **2**, 42 (1827).

[139] A. L. Cauchy, Exercices de Mathématiques **2**, 60 (1827).

[140] J. F. Nye, *Physical properties of crystals* (Clarendon Press, 1987).

[141] N. W. Ashcroft and N. D. Mermin, *Solid State Physics* (Thomson Learning, London, 1976).

[142] G. Green, *An Essay on the Application of Mathematical Analysis to the Theories of Electricity and Magnetism* (T. Wheelhouse, Nottingham, 1828).

[143] L. Dobrzynski, Surface Science Reports **6**, 119 (1986), ISSN 0167-5729.

[144] L. Dobrzynski, Surface Science Reports **11**, 139 (1990), ISSN 0167-5729.

[145] L. Dobrzynski, Surface Science **180**, 489 (1987), ISSN 0039-6028.

[146] E. E. Boudouti, B. Djafari-Rouhani, A. Akjouj, and L. Dobrzynski, Surface Science Reports **64**, 471 (2009), ISSN 0167-5729.

[147] A. Einstein, Ann. Phys. **33**, 1275 (1910), ISSN 1521-3889.

[148] B. J. Berne and R. Pecora, *Dynamic Light Scattering* (Dover, Mineola, 2000).

[149] L. Brillouin, Ann. Phys. (Paris) **17**, 88 (1922).

[150] D. Meschede, ed., *Gerthsen Physik* (Springer-Verlag Berlin Heidelberg, 2006), 23rd ed.

[151] K. R. Subbaswamy and A. A. Maradudin, Phys. Rev. B **18**, 4181 (1978).

[152] H. Lamb, Proc. London Math. Soc. **13**, 189 (1882).

[153] N. M. Temme, *Special Functions: An Introduction to the Classical Functions of Mathematical Physics* (John Wiley & Sons, Inc., 1996), ISBN 9781118032572.

[154] M. Gertsenshtein and V. Pustovoit, **43**, 605 (1962).

[155] A. Abramovici, W. E. Althouse, R. W. P. Drever, Y. Gürsel, S. Kawamura, F. J. Raab, D. Shoemaker, L. Sievers, R. E. Spero, K. S. Thorne, et al., Science **256**, 325 (1992).

[156] E. Hecht, *Optics* (Addison Wesley, 2002), 4th ed.

[157] H. D. Polster, J. Pastor, R. M. Scott, R. Crane, P. H. Langenbeck, R. Pilston, and G. Steinberg, Appl. Opt. **8**, 521 (1969).

[158] R. Mock, B. Hillebrands, and R. Sandercock, Journal of Physics E: Scientific Instruments **20**, 656 (1987).

[159] M. D. Rao, Journal of Sound and Vibration **262**, 457 (2003), ISSN 0022-460X.

[160] A. Gonzalez, M. Ferrer, M. de Diego, G. Piñero, and J. J. Garcia-Bonito, Journal of Sound and Vibration **265**, 663 (2003), ISSN 0022-460X.

[161] T. Gorishnyy, M. Maldovan, C. K. Ullal, and E. L. Thomas, Physics World **Dec**, 24 (2005).

[162] J. Page, Nat. Mater. **10**, 565 (2011), ISSN 1476-1122.

[163] J.-H. Jang, C. Y. Koh, K. Bertoldi, M. C. Boyce, and E. L. Thomas, Nano Letters **9**, 2113 (2009).

[164] A. B. Wood, *A Textbook of Sound* (G. Bell & Sons Ltd., New York, 1930).

[165] B. Djafari-Rouhani, L. Dobrzynski, O. H. Duparc, R. E. Camley, and A. A. Maradudin, Phys. Rev. B **28**, 1711 (1983).

[166] B. Jusserand, D. Paquet, F. Mollot, F. Alexandre, and G. Le Roux, Phys. Rev. B **35**, 2808 (1987).

[167] I. E. Psarobas, N. Papanikolaou, N. Stefanou, B. Djafari-Rouhani, B. Bonello, and V. Laude, Phys. Rev. B **82**, 174303 (2010).

[168] J. H. Moon and S. Yang, Chemical Reviews **110**, 547 (2010).

[169] Y. Pennec, J. O. Vasseur, B. Djafari-Rouhani, L. Dobrzyński, and P. A. Deymier, Surface Science Reports **65**, 229 (2010), ISSN 0167-5729.

[170] J. He, B. Djafari-Rouhani, and J. Sapriel, Phys. Rev. B **37**, 4086 (1988).

[171] M. Giehler, T. Ruf, M. Cardona, and K. Ploog, Phys. Rev. B **55**, 7124 (1997).

[172] M. Trigo, A. Fainstein, B. Jusserand, and V. Thierry-Mieg, Phys. Rev. B **66**, 125311 (2002).

[173] N. Combe, J. R. Huntzinger, and J. Morillo, Eur. Phys. J. B **68**, 47 (2009).

[174] E. H. El Boudouti, B. Djafari-Rouhani, E. M. Khourdifi, and L. Dobrzynski, Phys. Rev. B **48**, 10987 (1993).

[175] L. C. Parsons and G. T. Andrews, Journal of Applied Physics **111**, 123521 (2012).

[176] R. S. Penciu, G. Fytas, E. N. Economou, W. Steffen, and S. N. Yannopoulos, Phys. Rev. Lett. **85**, 4622 (2000).

[177] M. H. Kuok, H. S. Lim, S. C. Ng, N. N. Liu, and Z. K. Wang, Phys. Rev. Lett. **90**, 2555021 (2003).

[178] H. S. Lim, M. H. Kuok, S. C. Ng, and Z. K. Wang, Applied Physics Letters **84**, 4182 (2004).

[179] W. Cheng, J. J. Wang, U. Jonas, W. Steffen, G. Fytas, R. S. Penciu, and E. N. Economou, The Journal of Chemical Physics **123**, 121104 (2005).

[180] Y. Li, H. S. Lim, Z. K. Wang, S. C. Ng, and M. H. Kuok, Journal of Nanoscience and Nanotechnology **8**, 5869 (2008).

[181] T. Still, W. Cheng, M. Retsch, U. Jonas, and G. Fytas, Journal of Physics: Condensed Matter **20**, 404203 (2008), 0953-8984.

[182] T. Still, M. Retsch, U. Jonas, R. Sainidou, P. Rembert, K. Mpoukouvalas, and G. Fytas, Macromolecules **43**, 3422 (2010).

[183] E. Duval, A. Boukenter, and B. Champagnon, Phys. Rev. Lett. **56**, 2052 (1986).

[184] G. Mariotto, M. Montagna, G. Viliani, E. Duval, S. Lefrant, E. Rzepka, and C. Mai, Europhysics Letters. **6**, 239 (1988).

[185] M. Fujii, T. Nagareda, S. Hayashi, and K. Yamamoto, Phys. Rev. B **44**, 6243 (1991).

[186] H. Portales, L. Saviot, E. Duval, M. Fujii, S. Hayashi, N. D. Fatti, and F. Vallee, The Journal of Chemical Physics **115**, 3444 (2001).

[187] R. Ceccato, R. Dal Maschio, S. Gialanella, G. Mariotto, M. Montagna, F. Rossi, M. Ferrari, K. E. Lipinska-Kalita, and Y. Ohki, Journal of Applied Physics **90**, 2522 (2001).

[188] V. K. Tikhomirov, D. Furniss, A. B. Seddon, I. M. Reaney, M. Beggiora, M. Ferrari, M. Montagna, and R. Rolli, Applied Physics Letters **81**, 1937 (2002).

[189] M. Montagna, E. Moser, F. Visintain, M. Ferrari, L. Zampedri, A. Martucci, M. Guglielmi, and M. Ivanda, Journal of Sol-Gel Science and Technology **26**, 241 (2003), ISSN 0928-0707.

[190] M. Ivanda, K. Babocsi, C. Dem, M. Schmitt, M. Montagna, and W. Kiefer, Phys. Rev. B **67**, 2353291 (2003).

[191] M. Ivanda, A. Hohl, M. Montagna, G. Mariotto, M. Ferrari, Z. Crnjak Orel, A. Turković, and K. Furić, Journal of Raman Spectroscopy **37**, 161 (2006), ISSN 1097-4555.

[192] Y. Jestin, N. Afify, C. Armellini, S. Berneschi, S. N. B. Bhaktha, B. Boulard, A. Chiappini, A. Chiasera, G. Dalba, C. Duverger, et al., SPIE **6183**, 61831W (2006), ISSN 0277786X.

[193] M. Ivanda, K. Furic, S. Music, M. Ristic, M. Gotic, D. Ristic, A. M. Tonejc, I. Djerdj, M. Mattarelli, M. Montagna, et al., Journal of Raman Spectroscopy **38**, 647 (2007).

[194] M. Pelton, J. E. Sader, J. Burgin, M. Liu, P. Guyot-Sionnest, and D. Gosztola, Nat. Nano. **4**, 492 (2009), ISSN 1748-3387.

[195] T. Dehoux, T. A. Kelf, M. Tomoda, O. Matsuda, O. B. Wright, K. Ueno, Y. Nishijima, S. Juodkazis, H. Misawa, V. Tournat, et al., Opt. Lett. **34**, 3740 (2009).

[196] L. Saviot and D. B. Murray, Phys. Rev. B **81**, 235432 (2010).

[197] A. E. H. Love, *A treatise on the mathematical theory of elasticity* (Dover Publications, 1944).

[198] P. Benassi, O. Pilla, V. Mazzacurati, M. Montagna, G. Ruocco, and G. Signorelli, Phys. Rev. B **44**, 11734 (1991).

[199] R. S. Penciu, M. Kafesaki, G. Fytas, E. N. Economou, W. Steffen, A. Hollingsworth, and W. B. Russel, Europhysics Letters **58**, 699 (2002).

[200] X. Zhang, F. Wub, Y. Yao, and Z. Liu, Solid State Communications **150**, 275 (2010).

[201] N. F. Bunkin, V. Gorelik, and V. Filatov, Physics of Wave Phenomena **18**, 90 (2010).

[202] M. Kafesaki and E. Economou, Phys. Rev. B **52**, 13317 (1995).

[203] M. Mattarelli, M. Montagna, and P. Verrocchio, Applied Physics Letters **91**, 061911 (2007).

[204] M. Mattarelli, G. Gasperi, M. Montagna, and P. Verrocchio, Phys. Rev. B **82**, 094204 (2010).

[205] O. Pilla, A. Cunsolo, A. Fontana, C. Masciovecchio, G. Monaco, M. Montagna, G. Ruocco, T. Scopigno, and F. Sette, Phys. Rev. Lett. **85**, 2136 (2000).

[206] H. Kriegs, W. Steffen, G. Fytas, G. Monaco, C. Dreyfus, P. Fragouli, M. Pitsikalis, and N. Hadjichristidis, Journal of Chemical Physics **121**, 2376 (2004).

[207] M. Mattarelli and M. Montagna, Chemical Physics Letters **524**, 112 (2012), ISSN 0009-2614.

[208] R. Mindlin and H. Deresiewicz, Journal of Applied Mechanics **20**, 327 (1953).

[209] J. Duffy and R. Mindlin, Journal of Applied Mechanics **24**, 585 (1957).

[210] A. Merkel, V. Tournat, and V. Gusev, Phys. Rev. E **82**, 031305 (2010).

[211] H. Bilz and W. Kress, *Phonon Dispersion Relations in Insulators* (Springer-Verlag, Berlin, 1979).

[212] A. Bansal, Journal of Sound and Vibration, **207**, 365 (1997).

[213] P. Ngoepe, E. Lambson, G. Saunders, and B. Bridge, Journal of Material Science **25**, 4654 (1990).

[214] T. Still, M. D'Acunzi, D. Vollmer, and G. Fytas, Journal of Colloid and Interface Science **340**, 42 (2009).

[215] M. Grzelczak, J. Vermant, E. M. Furst, and L. M. Liz-Marzan, ACS Nano **4**, 3591 (2010).

[216] S. Sacanna and D. J. Pine, Curr. Opin. Colloid Interface Sci. **16**, 96 (2011).

[217] S. C. Glotzer and M. J. Solomon, Nat. Mater. **6**, 557 (2007).

[218] B. Madivala, J. Fransaer, and J. Vermant, Langmuir **25**, 2718 (2009).

[219] Z. Zhang, P. Pfleiderer, A. B. Schofield, C. Clasen, and J. Vermant, J Am Chem Soc **133**, 392 (2011).

[220] T. Ding, K. Song, K. Clays, and C.-H. Tung, Adv Mater **21**, 1936 (2009).

[221] T. Ding, K. Song, K. Clays, and C.-H. Tung, Langmuir **26**, 11544 (2010).

[222] J. P. Singh, P. P. Lele, F. Nettesheim, N. J. Wagner, and E. M. Furst, Phys. Rev. E **79**, 050401 (2009).

[223] M. Mittal and E. M. Furst, Advanced Functional Materials **19**, 3271 (2009), ISSN 1616-3028.

[224] A. A. Shah, H. Kang, K. L. Kohlstedt, K. H. Ahn, S. C. Glotzer, C. W. Monroe, and M. J. Solomon, Small **8**, 1551 (2012).

[225] M. Mittal, R. K. Niles, and E. M. Furst, Nanoscale **2**, 2237 (2010).

[226] T. B. Jones, *Electromechanics of Particles* (Cambridge University Press, 1995).

[227] P. Pfleiderer and T. Schilling, Phys. Rev. E **75**, 020402 (2007).

[228] A. Donev, F. H. Stillinger, P. M. Chaikin, and S. Torquato, Phys. Rev. Lett. **92**, 255506 (2004).

[229] P. E. Hopkins, M. Mittal, L. M. Phinney, A. M. Grillet, and E. M. Furst, Appl. Phys. Lett. **99**, 133106 (2011).

[230] H. Portalès, N. Goubet, L. Saviot, P. Yang, S. Sirotkin, E. Duval, A. Mermet, and M.-P. Pileni, ACS Nano **4**, 3489 (2010), ISSN 1936-0851.

[231] J. Margueritat, J. Gonzalo, C. N. Afonso, A. Mlayah, D. B. Murray, and L. Saviot, Nano Letters **6**, 2037 (2006).

[232] J.-H. Kang and A. Leissa, Acta Mechanica **197**, 97 (2008), ISSN 0001-5970.

[233] N. Gomopoulos, G. Saini, M. Efremov, P. F. Nealey, K. Nelson, and G. Fytas, Macromolecules **43**, 1551 (2010).

[234] L. Saviot and D. B. Murray, Phys. Rev. B **79**, 214101 (2009).

[235] D. Konopinski, S. Hudziak, R. Morgan, P. Bull, and A. Kenyon, Forensic Science International **223**, 245 (2012), ISSN 0379-0738.

[236] M. Sinha, B. Erman, J. E. Mark, T. H. Ridgway, and H. E. Jackson, Macromolecules **36**, 6127 (2003), ISSN 0024-9297.

[237] C. Vega, E. P. A. Paras, and P. A. Monson, The Journal of Chemical Physics **96**, 9060 (1992).

[238] R. C. Kramb, R. Zhang, K. S. Schweizer, and C. F. Zukoski, Phys. Rev. Lett. **105**, 055702 (2010).

[239] P. Pfleiderer, K. Milinkovic, and T. Schilling, EPL (Europhysics Letters) **84**, 16003 (2008).

[240] R. C. Kramb, R. Zhang, K. S. Schweizer, and C. F. Zukoski, The Journal of Chemical Physics **134**, 014503 (2011).

[241] J. D. Forster, J.-G. Park, M. Mittal, H. Noh, C. F. Schreck, C. S. O'Hern, H. Cao, E. M. Furst, and E. R. Dufresne, ACS Nano **5**, 6695 (2011), ISSN 1936-0851.

[242] S. Sacanna, L. Rossi, A. Wouterse, and A. P. Philipse, Journal of Physics: Condensed Matter **19**, 376108 (2007), ISSN 0953-8984.

[243] J. Sun, Z. Wang, H. Lim, V. Zhang, S. Ng, M. Kuok, W. Zhang, S. Firdoz, and X. Lu, Solid State Communications **152**, 501 (2012), ISSN 0038-1098.

[244] F. Lemoult, N. Kaina, M. Fink, and G. Lerosey, Nat. Phys. **9**, 55 (2013), ISSN 1745-2473.

[245] B. Fischer, M. Ziadeh, A. Pfaff, J. Breu, and V. Altstädt, Polymer **53**, 3230 (2012), ISSN 0032-3861.

[246] F. Natalio, T. P. Corrales, M. Panthöfer, D. Schollmeyer, I. Lieberwirth, W. E. G. Müller, M. Kappl, H.-J. Butt, and W. Tremel, Science **339**, 1298 (2013).

[247] R. Ene, P. Papadopoulos, and F. Kremer, Soft Matter **5**, 4568 (2009), ISSN 1744-683X.

[248] Z. Qin and M. J. Buehler, Nat. Mater. **12**, 185 (2013), ISSN 1476-1122.

Acknowledgments

This thesis only came into being with the help of numerous people along the road. During my stay at MPIP, I had the chance to make friends and get to know many interesting collaborators. First of all, I want to express my sincerest gratitude to my advisors Prof. [redacted] and Prof. [redacted] for all their input and helpful discussions in the course of my thesis. Working in the group of Prof. [redacted] was a great experience and I'm thankful that he gave me the opportunity to be part of his team at MPIP. I enjoyed the interdisciplinary atmosphere and all the freedom and support provided, which is in my opinion exceptional even in academia. I thank Prof. [redacted] (Univ. of Mainz) not only for the fruitful collaboration but also for the review of my thesis. Prof. [redacted] is gratefully acknowledged for being the third examiner in my thesis defense.

I'm obliged to honor Prof. [redacted] with my deepest gratitude, who turned out to be a great advisor and friend. Sharing an office for more than three years along with stimulating discussions, mostly but not always about science, shaped my view on research. He knows how to gently push young people helping them to get things back into focus and shares his experience to be more relaxed in unknown situations. Indeed, his superior enthusiasm for scientific exchange was already truly remarked by Paul in Acts 17,21a "All the people of Athens loved to spent their time talking about and listening to the latest ideas."

This thesis is based on several collaborations. I want to thank [redacted] and [redacted] from the [redacted] group, for the tedious preparation of the hybrid superlattices, and of course also Prof. [redacted] himself for all his contributions. I owe my sincerest thanks to [redacted] and [redacted], for their endless patience in answering my questions and being always committed coworkers. Also their group members, especially [redacted], [redacted] and [redacted] are acknowledged for their contribution in the background. [redacted] and [redacted] mainly provided the theory for the calculation of particle vibration spectra. Thank you!

During their short research stay at MPIP, I had the chance to work with [redacted] [redacted] (Group of [redacted], Columbia) and [redacted] ([redacted] group, UDel). Their work partially entered the thesis, for which I also acknowledge [redacted], [redacted], [redacted] and [redacted] for the synthesis of the studied particles. I thank Prof. [redacted] and [redacted] for providing first theoretical insights regarding anisotropic colloidal crystals. I'm grateful for the stimulating work with [redacted] (Princeton), at the begin of my thesis. [redacted], Prof. [redacted] and Prof. [redacted] gave me the chance to study the peculiar properties of semi-flourinated sytems. [redacted] [redacted] is acknowledged for his incredible patience with the spider silk project. [redacted] and Prof. [redacted] (UPenn) readily endorsed our proposition and fabricated the nanoridges. [redacted], [redacted] and Prof. [redacted] (CMU) are gratefully acknowledged for their hospitality and the interesting ongoing collaboration on brushed nanoparticle films. So are [redacted] and [redacted] [redacted] (U. Le Havre) for the corresponding preliminary calculations. [redacted] [redacted] and [redacted] (U. Osnabrück) came up with an interesting collaboration on porous glasses.

This institute wouldn't perform nearly as well without the technicians, workshops and all the other in-house services. A big thanks to you! Especially, I want to acknowledge [redacted] and [redacted] for their help and introduction to electron microscopy, as well as [redacted] for DSC measurements and [redacted] [redacted] for vapor deposition. On this occasion, I have to highlight [redacted]'s uncommonly high reliability and his exceptional skills in tutoring students.

During the first three months of my thesis work, [redacted] introduced me to BLS and helped me getting started at MPIP. Even after he has left the institute, he was willing to answer my questions. I thank [redacted], [redacted] and [redacted] [redacted] for their assistance with formalities and advise in experimental subtleties. Thanks again to my diploma thesis advisor Prof. [redacted] and his right-hand man [redacted], who introduced me to X-ray scattering and made me stick to physical chemistry.

[redacted], [redacted] and [redacted] kindly agreed to proofread parts of the thesis. I thank my office mates [redacted] and [redacted] [redacted] for the company throughout the last years and months. My time at MPIP was shaped by all the friends I made here, especially those with whom I spent lunch breaks and hung out in the coffee corner. Great to know you guys! Also, the friends that I met during the conferences and especially at the summer school in France; it was a pleasure to get to know you and share a great time together. I'm full of gratitude for all my friends and family outside academia, G7, Dünis, and more; you know who you are! Special thanks is given to my parents, who supported me throughout my life and from the very beginning. In the end, I express my deepest thanks to the woman of my life for all the great times and for carrying me through the hard times every PhD thesis brings along. Thank you for your endless love and kindness!